

Novel Electronic States in Sodium Cobaltates Na_xCoO_2

Author: Meng Gao

Persistent link: <http://hdl.handle.net/2345/990>

This work is posted on [eScholarship@BC](#),
Boston College University Libraries.

Boston College Electronic Thesis or Dissertation, 2009

Copyright is held by the author, with all rights reserved, unless otherwise noted.

Boston College

The Graduate School of Arts and Sciences

Department of Physics

NOVEL ELECTRONIC STATES IN Na_xCoO_2

A DISSERTATION

By

MENG GAO

submitted in partial fulfillment of the requirements

for the degree

DOCTOR OF PHILOSOPHY

December 2009

© Copyright by MENG GAO 2009

All Rights Reserved

ABSTRACT

NOVEL ELECTRONIC STATES IN Na_xCoO_2

MENG GAO

Dissertation Advisor: Dr. Ziqiang Wang

Transition metal oxides occupy an important arena in strongly correlated materials. We focus here on the triangular lattice sodium cobaltates which display a very rich phase diagram as a function of Na doping x with many new surprises. We review a spectrum of recent experiments and argue that strong correlation and Na dopant potential play essential roles in understanding the unconventional behaviors of the charge, spin, and orbital degrees of freedom of the Co $3d$ electrons.

The strong Co intra-atomic Coulomb repulsion renormalizes the crystal field splitting and the bandwidths of the t_{2g} complex in Na_xCoO_2 , resulting in a single band crossing the Fermi level at all doping levels x explored by ARPES experiments. On this basis, we study the electronic states using a minimal one-band Hubbard model with large U on the triangular lattice. The strong correlation renormalizes the Stoner criterion and stabilizes the paramagnetic state for $x < x_c \simeq 0.67$.

The important role played by the off-plane Na dopants is taken into account by including the ionic electrostatic potential. In the Na rich part of the phase diagram, the high density of off-plane Na dopants (or dilute Na vacancies) increases the tendency toward carrier localization in the Co plane, which competes with in-plane ferromagnetic (FM) correlations described by a renormalized Stoner theory and leads to an inhomogeneous FM state, exhibiting nonmagnetic Co^{3+} patches, AF correlated regions, and FM clusters with AF domains.

We argue that the newly discovered $x=11/13$ phase associated with Na vacancy order can be described by the interplay between the sodium potential and the strong correlation, which gives rise to the coexistence of FM itinerant carriers and local moments.

Acknowledgements

I am deeply indebted to my dissertation committee chair, Prof. Ziqiang Wang, for his numerous discussions, continuous guidance, and helpful comments throughout my entire study in the Ph.D. program. His wisdom, knowledge, and commitment to the highest standards have inspired and motivated me. I am also very thankful to my dissertation committee members, Prof. Hong Ding and Prof. Vidya Madhavan for all the helpful comments, suggestions and encouragement. I benefited a lot from the joint group meetings with them. I would also like to thank Prof. Willie Padilla for his time and inputs to serve on my committee.

I am pleased to take this opportunity to thank my friends and colleagues, their warm and generous help has been great support to me. I especially thank Sen Zhou and Chunhua Li for all the discussions and intelligent answers to my questions. I also thank Liang Niestemski, Feng Cai, Yuanming Lu, Yiming Xu, Jihua Ma, and Zhihui Pan for their help and support in many ways. I am very glad to work or collaborate with them.

My most sincere thanks also go to my family. I would like to thank my parents who have been great support to me from the very beginning of my study. Last but not least, I am deeply grateful to my husband, Jiekun Huang, for his support, encouragement, and patience during my dissertation study.

I owe my gratitude to all those people who have made this dissertation possible and because of whom my graduate experience has been one that I will cherish forever.

Table of Contents

ABSTRACT	III
Acknowledgements	V
List of Figures	IX
Chapter 1. Introduction	1
References	11
Chapter 2. Electron Correlation and Fermi Surface Topology of Na_xCoO_2	13
2.1. Theoretical calculation of band structure	13
2.2. Experimental results of the band structure	19
2.3. Electron correlation and Fermi surface topology	26
References	41
Chapter 3. Stoner Magnetism	43
3.1. Single band model for sodium cobaltates: a minimal model	44
3.2. Stoner Magnetism	46
3.3. Single band in the strong coupling limit	48
3.4. Magnetism in Na_xCoO_2	59
References	63

Chapter 4. Itinerant and Localized Magnetism in Sodium Rich Phases of Na_xCoO_2	64
4.1. Recent focus on magnetism in sodium rich phases	64
4.2. Sodium structure	67
4.3. Itinerant and localized magnetism	70
References	78
Chapter 5. Novel Electronic States at $x=0.84$	80
5.1. Na ordering and Na potential	80
5.2. Experimental evidence of coexistence of localized moments and itinerant carriers	85
5.3. Charge ordering with small sodium potential	88
5.4. High temperature PM order	91
5.5. Low temperature FM order	95
5.6. Thermal properties of $\text{Na}_{11/13}\text{CoO}_2$	99
5.7. Similar superstructure at $x=12/13$	101
5.8. Conclusion	103
References	104

List of Figures

- 1.1 Structural views of $\text{Na}_{0.7}\text{CoO}_2$ (left) and $\text{Na}_{0.35}\text{CoO}_2 \cdot 1.3\text{H}_2\text{O}$ (right) [3], where Na and H_2O sites are partially occupied. 2
- 1.2 Phase diagram of sodium doped cobaltates Na_xCoO_2 [8] 3
- 1.3 a) CoO_6 octahedron, red spheres represent oxygen; the center blue is Co; the yellow spheres above and below the octahedron are Na ions. The octahedron is largely tilted. b) Top-down views of a single CoO_2 layer found in the new cobalt oxide superconductor and related sodium cobalt oxide bronzes [9]. In this hexagonal lattice, cobalt atoms and oxygen atoms are represented by blue and red colors, respectively. Any antiferromagnetic ordering is frustrated by the triangular arrangement of the cobalt atoms, which does not allow for a single minimum energy configuration of opposing spins. 4
- 1.4 a) the degenerate $3d$ orbitals are split into degenerate e_g bands and t_{2g} complex under the octahedral field, and t_{2g} complex are further split into e'_g bands and a_{1g} band under trigonal field by the octahedral tilting. The 2 octahedrons in the plot are schematic plots of CoO_6 and the tilting of it. b) Atomic occupation scheme for the Co ions in cobaltates. The e_g bands are clearly separated from t_{2g} with an energy difference

about 2.5 eV [10]. On the left, when $x=0$, lower a_{1g} band and one e'_g band are fully filled with the other e'_g band half filled. Co atoms form Co^{4+} ion and the low spin state is $S=1/2$ due to open shell occupation. On the right hand side, it shows the filling scheme when $x=1$. All 3 bands in the t_{2g} complex are fully filled, resulting a close shell Co^{3+} and the low spin state $S=0$.

6

2.1 LDA prediction of the electronic structure of NaCo_2O_4 in paramagnetic state. a) the electronic structure of NaCo_2O_4 , the horizontal dotted line denotes Fermi energy E_F . b) the enlargement around E_f shows the t_{2g} manifold. c) LDA Fermi surfaces of NaCo_2O_4 in the $k = 0$ (on the left) and $k_z = 0.5$ (on the right) planes.

16

2.2 a) The density of states of $\text{Na}_{0.3}\text{CoO}_2 \cdot y\text{H}_2\text{O}$ and of the two bands crossing the Fermi level. The a_{1g} band, which carries 2/3 of all holes, yields only about 1/3 of $\text{DOS}(E_F)$. b) Fermi surface of $\text{Na}_{0.3}\text{CoO}_2 \cdot y\text{H}_2\text{O}$ with three main nesting types. Q_1 in a solid line is the perfect nesting, Q_2 in a narrow line and Q_3 in a wide dashed line are shown as imperfect nesting.

19

2.3 Band structure (in the virtual crystal approximation) along high symmetry lines (left panel) and the aligned density of states (right panel) for the $x=1/3$ cobaltate in the local density approximation. The a_{1g} symmetry band is emphasized with circles proportional to the

amount of a_{1g} character. The a_{1g} density of states is indicated by the darker line. 20

2.4 a) Measured FS crossing compared to calculated FS in $k_z = 0$ (black solid lines) and $k_z = 0.5$ (red dashed lines) planes. The blue hexagon is the 2D BZ. b) Extracted band positions (red dots) along $\Gamma - M$ and a tight binding fit with $t=-44$ meV. c) Extracted band positions along $\Gamma - K$ (red dots) and two tight binding fits with $t=-12$ meV (solid line) and $t=-26$ meV. 23

2.5 FS evolution in Na_xCoO_2 . a)-c) Fermi surface intensity contours at $x = 0.3, 0.48$, and 0.72 in the 1st Brillouin zone. d) Overlap of the FS locations at different doping levels. e) Effective Na concentration x' derived from FS area *vs* Na concentration x . The diagonal line is from the Luttinger theorem. 25

2.6 a) n_k plot generated by integrating within 75 meV of Fermi level. A hole pocket is centred around the Γ point. b) Comparison with LDA calculation on $NaCo_2O_4$. Red dots indicate the location of measured Fermi crossing in $Na_{0.7}CoO_2$. c) E *vs* k plots based on the extracted peak positions in $\Gamma - M$ (left) and $\Gamma - K$ (right) directions. 26

2.7 Tight-binding fits to the LDA band structure at $x = 1/3$. a) The fitted band dispersions with up to 3rd, 5th and 8th NN hopping. The corresponding Fermi surfaces are plotted in b), c), and d) respectively. 33

- 2.8 HF results for $U = 3.0 \text{ eV}$ at $x = 1/3$. a) The band dispersions for $\eta = 1/3, 1/2, 2/3$, and b) the η dependence of the HF and kinetic energies and the renormalized atomic level spacing Δ' . 33
- 2.9 The doping x dependence of the bandwidth renormalization and the level spacing between a_{1g} and e'_g orbitals. 35
- 2.10 The band dispersions and the Fermi surfaces in the strong coupling limit (red solid lines) for doping $x = 0.3, 0.5$ and 0.7 . The results in non-interacting limit (blue dashed lines) are also plotted for comparison. 38
- 2.11 Experiment *v.s.* theory [21]: Comparison of a) experimental band structure for $x = 0.35, x = 0.48$, and $x = 0.75$ with b) LDA + large- U calculation. 39
- 3.1 The division line represents x_c and separates ferromagnetic state (FM) and paramagnetic state (PM), corresponding to varying U 49
- 3.2 Phase diagram of a_{1g} band, $x_c = 0.67$ 52
- 3.3 a)The density of states of a single 1st *n.n.* hopping band, on the electron doped side, paramagnetic (PM) and on the hole doped side, ferromagnetic (FM). b)Band structure at $x = 0.1$, electron doped. 53
- 3.4 a)The density of states of a_{1g} band up to 3rd *n.n.* hopping, on the electron doped side, paramagnetic (PM) and ferromagnetic (FM) are separated at $x_c = 0.67$. b)Band structure is at $x = 0.67$, electron doped. 54
- 3.5 Paramagnetic DOS at $x = 0.5$ (dotted) and $x = 0.7$ (solid), with $U \rightarrow \infty$ 55

- 3.6 Susceptibility of single a_{1g} band with 3^{rd} *n.n.* hopping diverges at $x_c = 0.67$ 57
- 3.7 Dots are numerical calculation of ground state energy as a function of M . Solid lines are 2^{nd} order polynomial fit. Results are shown at $x = 0.63, 0.65, 0.67, 0.69$. $\chi^{-1} \propto a_2$ 58
- 3.8 Phase diagram of the 3-band model. a) phase diagram of a multi-band Hubbard model for Na_xCoO_2 as a function of U in Hartree-Fock approximation. b) The interplay of J and U at $x=0.5$ in HFA. c) In strong U limit, phase diagram at different doping levels. 61
- 4.1 a)-c) Zero-field μ SR spectra for Na_xCoO_2 crystals with $x=0.92, 0.87$ and 0.78 which exhibit a rapidly increasing fraction of the oscillatory signal at 5 K. d) Polaron model[10]: Co^{4+} with $s=1/2$ in the center, induced spin $S=1$ on the six adjacent Co^{3+} sites. J, J_{diag} , and J' are parameters for nearest neighbour coupling on the ring, cross diagonal coupling and center to the ring coupling, respectively. 66
- 4.2 The three types of hexagonal structure in Na_xCoO_2 H1-H3. Layers of edge-shared CoO_6 octahedra are seen in a triangular lattice with Na ions occupying ordered or disordered positions in the interleaving planes. Three different Na ion sites are shown beneath. 68
- 4.3 a) The general structural characteristics and compositional stability regions of the four Na_xCoO_2 phases, H1-H3, O1. Above the panel,

- the sodium ion distributions are shown schematically. b). Fractional occupancies of the two types of sodium sites. 69
- 4.4 The spin (colored arrows) and charge (local doping x_i) distribution in a typical Na(1) and Na(2) realization at $x = 0.8$ (a) and $x = 0.97$. (c) The one-particle spectral intensity (top) and its spin resolved components at $x = 0.8$. 72
- 4.5 (a) Spectral intensity of one-hole doped by a Na(2) vacancy at $V_d = 1.0$ eV. (b) Spin and charge distribution of the $S=1/2$ local moment near a Na(1) and a Na(2) vacancy. (c) The local moment “binding energy” E_b as a function of V_d induced by a Na(1) or Na(2) vacancy at $V_d = 0.6$ eV. (d) Spin/charge distribution around two Na(1) and two Na(2) vacancies shows AF correlations between the local moments. 77
- 5.1 Models for the Na planes of Na_xCoO_2 with $x = 0.15 \sim 0.75$. Both the Na planes on $z = 0$ and $z = 1/2$ are given. Occupied Na positions are given as black dots and Na vacancies as open circles. X indicates the positions of the underlying Co atoms. Dashed lines indicate that only one of the lines on $z = 0$ and $z = 1/2$ is occupied. The basic hexagonal unit cell is indicated by dotted lines. Below the models are the calculated diffraction patterns for a thickness of 10 nm and 200 kV. 81
- 5.2 Self-consistent $x=0.5$ states at different temperatures. From left to right columns, charge- or spin-ordering patterns and unit cells; FS without thermal broadening showing the anisotropic gapping of the

- FS; intensified FS showing the band folding along zone boundaries of corresponding charge or spin order. 82
- 5.3 Proposed crystal structure of $Na_{0.84}CoO_2$. a) and b) are the 2D view of the Na layers A and B with superstructure of $\sqrt{13} \times \sqrt{13}$, shown by solid lines. c) shows the corresponding 3D structure of in-phase stacking, although there is no way to tell in-phase and out of phase stacking in experiments. There is a 180° rotation between two adjacent layers. 84
- 5.4 a) Energy for two vacancies decreases with increasing distance d , in the units of the hexagonal lattice parameter a , as expected for Coulomb repulsion. The divacancy structure has lower stabilization energy than other structures simply with sites apart. (b) Ground-state energies of super structure for mono-vacancies (black), divacancies (red), tri-vacancies (blue) and quadri-vacancies (green). The inset shows the $x=0.8$ tri-vacancy phase. 85
- 5.5 FS area measurement and topology scheme at $x=0.84$. a) Amplitude of the fast Fourier transform normalized by temperature T for several values of T . Two main frequencies are detected: $F_1 = 125 T$, $F_2 = 190 T$. b) The superlattice-induced new Brillouin zone (blue dotted line) is $1/13$ of area of the original FBZ, and the spin-polarized Fermi surface for 2 and 1 hole per unit formula, respectively, in black and purple. For 1 hole per reconstructed unit cell, the originally depicted spin-polarized Fermi surface intersects with the new Brillouin zone. 87

- 5.6 PM states with small $V_c = V_d = V$ at $x=11/13$. a) Band structure with $V=0.2$ eV, semi-metal. b) FS of the semi-metal at $V=0.2$ eV. Red lines indicate the reconstructed 1st Brillouin zone. c) Band structure with $V=0.3$ eV is totally gapped and becomes a band insulator. 91
- 5.7 Band Structure and Fermi surface of PM state with one local moment and one itinerant carrier. K' indicates points at the corner of the reduced 1st Brillouin zone. M' indicates points in the middle of 2 nearest K' points. The system maintains 6-fold symmetry. a),b)States with a parameter $V=0.6$ eV c),d)States with a parameter $V=1.2$ eV 94
- 5.8 Energy comparison between the insulating state and the state with one local and one itinerant holes, as a function of V . 95
- 5.9 Band structure and Fermi surface of FM state with top band filled by one hole with spin σ . a),b)States with a parameter $V=0.6$ eV c),d)States with a parameter $V=1.2$ eV 97
- 5.10 A Kondo insulator with large V_c . a) Band structure with 2 hole localized and AFM correlated. b) Madelung potential on real-space cobalt sites. The first hole is localized on the blues sites. The second localized hole can reside on any equivalent brown points within one unit cell due to degeneracy. 98
- 5.11 Thermal properties of Na_xCoO_2 a) γ calculation from DMFT method [20]. Different lines indicate different crystal field splitting values. At large U values, γ is around 14 mJ/mole K^2 b),c) Experimentally

observed specific heat linear coefficient.[6, 7] d) Calculated electronic contribution of C/T at $x=0.3$ and $x=0.84$ with different parameters V .

The linear coefficient is extrapolated from the high temperature range. 100

5.12

a) Sodium arrangement of $2\sqrt{13} \times \sqrt{13}$ superstructure in each layer.

Solid dots and empty circles represent sodium ion in two adjacent layers.

The blue ones are Na1 and the green ones are Na2. b) Above magnetic

transition T_N , PM metallic state with 1 hole per super unit. c) Below

T_N , FM state is filled by 1 hole per super unit and becomes a band

insulator.

102

CHAPTER 1

Introduction

Understanding materials containing strongly correlated electrons represents both the challenge and the vitality of condensed matter physics. It is invigorated by the continuing discovery of new materials and physical properties that demand new ideas and approaches for a deeper understanding of the quantum many-body and statistical physics. The study of electron correlation in transition metal oxides occupies an important area in condensed matter and materials physics. A few recent examples include the high- T_c cuprates, the CMR manganites, and the unconventional pairing state in the ruthenates. We focus on the physics of electron correlation in sodium doped cobaltates, Na_xCoO_2 . The sodium cobaltates provide a unique low-spin, triangular lattice fermion system with strong electronic correlation and geometrical frustration in the charge, spin, and orbital sectors.

The cobaltates had been studied primarily for their high thermal electric performance [1, 2], until early 2003 when experimentalists at NIMS announced the discovery of a new superconductor, $\text{Na}_x\text{CoO}_2 \cdot y\text{H}_2\text{O}$, shown in Fig. 1.1, with a T_c of about 5 K [3]. It is the first layered superconductor to replace copper in the copper with cobalt. Since then, it has received growing, widespread interests both theoretically and experimentally. A broad spectrum of experiments such as NMR, μSR , ARPES, electric and thermal transport, optical absorption, and neutron diffraction have been performed, yielding a rich phase diagram and many unexpected and exotic behaviors. A detailed phase diagram is plotted

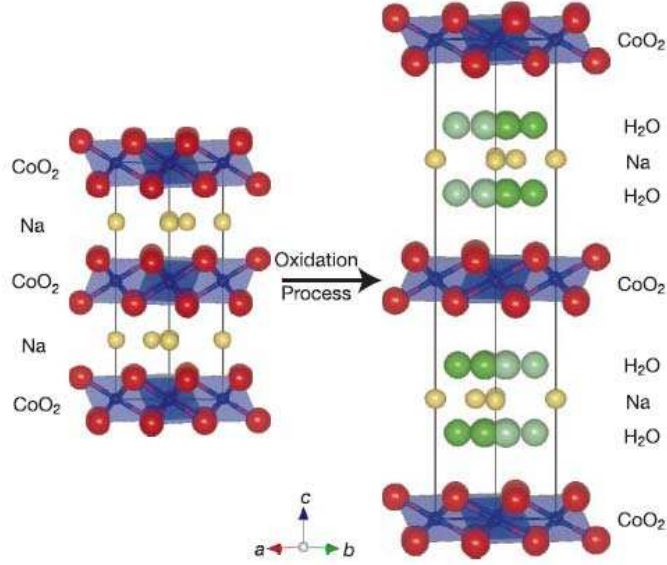


Figure 1.1. Structural views of $\text{Na}_{0.7}\text{CoO}_2$ (left) and $\text{Na}_{0.35}\text{CoO}_2 \cdot 1.3\text{H}_2\text{O}$ (right) [3], where Na and H_2O sites are partially occupied.

by Foo *et al* across a wide doping range to explore the connection between different electronic states, shown in Fig. 1.2. At $x \sim \frac{2}{3}$, where Na_xCoO_2 exhibits an unusually large thermopower [1], it displays a surprising Curie-Weiss magnetic profile [4]. At $x = 0.5$, which is not a natural commensurate filling on a triangular lattice, an unexpected charge ordered insulating phase emerges. For $\frac{1}{3} < x < \frac{1}{4}$, when it is intercalated with water, Na_xCoO_2 , superconductivity has been found with T_c close to 5K [3, 5, 6, 7].

Sodium cobaltates, Na_xCoO_2 , are electron doped transition metal oxides with a layered, hexagonal lattice structure. The layered structure has already been shown in Fig. 1.1 by Takada *et al*, before and after water intercalation. Before the oxidation process,

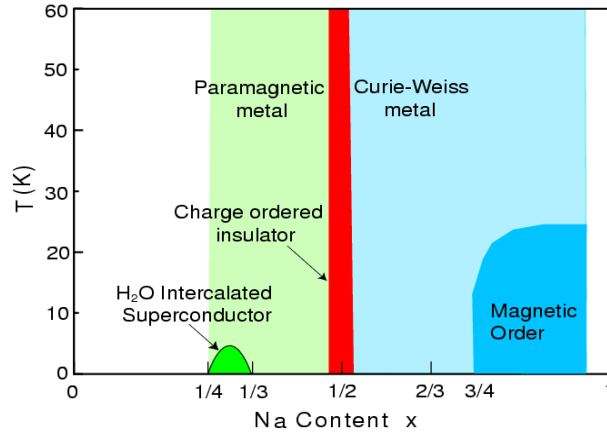


Figure 1.2. Phase diagram of sodium doped cobaltates Na_xCoO_2 [8]

$\text{Na}_{0.7}\text{CoO}_2$ has a hexagonal layered structure consisting of the two-dimensional CoO_2 layers and alternating charge-balancing Na^+ ions. A remarkable increase in c axis is observed after the oxidation process. a slightly decreases from 2.8292 Å in the parent compound to 2.8230 Å, probably because Co^{3+} ions are partially oxidized to smaller Co^{4+} . Meanwhile, c increases remarkably from 10.9628 Å in the parent compound to 19.6207 Å after the oxidation process. An amplification of CoO_2 layer is shown in Fig. 1.3. It consists of octahedra as in Fig. 1.3(a) with cobalt atoms at the center surrounded by six neighboring oxygen atoms. The CoO_6 octahedra share edges with the nearest octahedra within the same CoO_2 layer, and all the oxygens are not on the Co layer. If one views

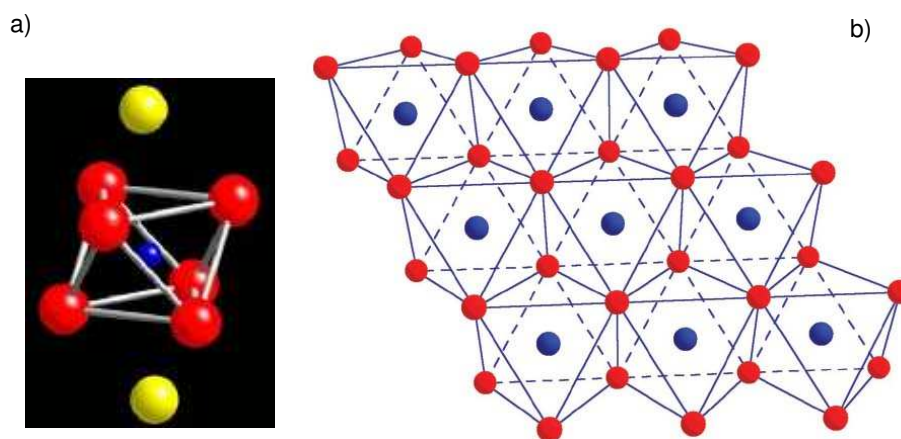


Figure 1.3. a) CoO_6 octahedron, red spheres represent oxygen; the center blue is Co; the yellow spheres above and below the octahedron are Na ions. The octahedron is largely tilted. b) Top-down views of a single CoO_2 layer found in the new cobalt oxide superconductor and related sodium cobalt oxide bronzes [9]. In this hexagonal lattice, cobalt atoms and oxygen atoms are represented by blue and red colors, respectively. Any antiferromagnetic ordering is frustrated by the triangular arrangement of the cobalt atoms, which does not allow for a single minimum energy configuration of opposing spins.

the CoO_2 layer along c axis, the projection on the cobalt layer is shown in Fig. 1.3. From band calculation, there are Co $3f$ bands and O $2p$ bands. The Co d -O p hybridization is weak [10], since the $\text{Co}d$ bands are cleanly separated from $\text{O}2p$ bands.

Furthermore, the atomic orbitals are presented in Fig. 1.4(a). Without any extra field, cobalt atoms with atomic number 27 have 5 degenerate $3d$ orbitals. Each Co is located at the center of an octahedron. The CoO_6 octahedron is largely tilted. First, the oxygen octahedral field splits the $3d$ orbitals into e_g and t_{2g} complex. Then because of the tilting of the octahedron, it generates a trigonal field, which further splits the t_{2g} complex into 2 degenerate e'_g bands and 1 lower a_{1g} level. In our study, the electron fillings are only up to e'_g and the e_g bands are well separated from t_{2g} complex, so we will only focus on the t_{2g} complex.

Electronically, Co has partially filled $3d$ orbitals. Co^{4+} is in the $3d^5$ configuration, with 5 electrons occupying the three lower t_{2g} orbitals similar to the ruthenates (Sr_2RuO_4). The low-spin state of Co^{4+} is $S = 1/2$. Adding sodium corresponds to electron doping. With a sodium content x , the average Co valence is $\text{Co}^{(4-x)+}$, evolving from an open shell Co^{4+} with $S = 1/2$ at $x = 0$ to a closed shell Co^{3+} with a low-spin state $S = 0$ at $x = 1$, as shown in Fig. 1.3. Thus, the cobaltates provide an almost ideal system of spin-1/2 triangular lattice fermions for studying the physics of correlation and geometrical frustration in the charge, spin, and orbital sectors.

This dissertation is organized as follows. In Chapter 2, we propose to investigate how strong correlations not included in LDA promote inter-orbital carrier transfer, leading to an orbital polarized state with the FS topology and band narrowing observed by ARPES.

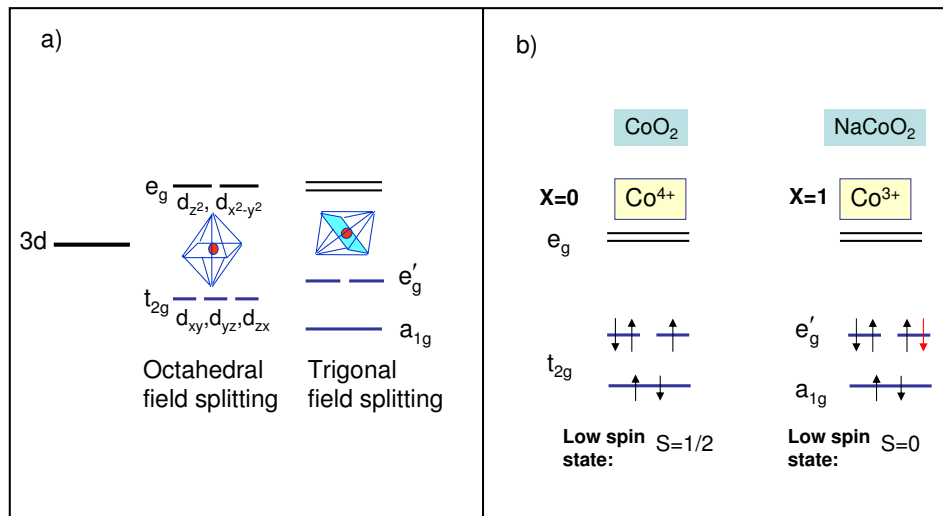


Figure 1.4. a) the degenerate 3d orbitals are split into degenerate e_g bands and t_{2g} complex under the octahedral field, and t_{2g} complex are further split into e'_g bands and a_{1g} band under trigonal field by the octahedral tilting. The 2 octahedrons in the plot are schematic plots of CoO_6 and the tilting of it. b) Atomic occupation scheme for the Co ions in cobaltates. The e_g bands are clearly separated from t_{2g} with an energy difference about 2.5 eV [10]. On the left, when $x=0$, lower a_{1g} band and one e'_g band are fully filled with the other e'_g band half filled. Co atoms form Co^{4+} ion and the low spin state is $S=1/2$ due to open shell occupation. On the right hand side, it shows the filling scheme when $x=1$. All 3 bands in the t_{2g} complex are fully filled, resulting a close shell Co^{3+} and the low spin state $S=0$.

This is an important and necessary step toward understanding the origin of superconductivity in this material. We adopt the “standard model” of transition metals and consider a three-band Hubbard model for the t_{2g} complex. We carried out a LDA+U analysis, which amounts to an orbital Hartree-Fock (HF) approximation, and elucidated the dynamics of orbital carrier transfer. The LDA+U analysis shows that the “sinking” of the six FS pockets is the physics of large U/J_H . However, the theory itself becomes unreliable in this regime. To correctly capture the basic strong-coupling physics, we considered the limit $U \rightarrow \infty$. We extended the Gutzwiller approximation to the projected wavefunctions to the multi-orbital case. The most important feature of the strong-coupling approach is that there is no unphysical self-energy cost that scales with U . The band center shifts according to the average Gutzwiller projected kinetic energy in a specific band. The combined effect of orbital dependent Gutzwiller band-narrowing and the band center shifts causes holes to move out of the e'_g band into the a_{1g} band. We obtained both band narrowing and the disappearance of the FS pockets for a wide range of doping, which are consistent with the ARPES experiments.

The FS topology measured by ARPES and calculated using our strong-coupling theory described in the last section suggests that the orbital degrees of freedom are confined by strong correlation. In Chapter 3, we propose that a single, strongly correlated a_{1g} t-U-V model as a minimal model for the low energy physics. Using this model, we show that the same strong correlation is also required to give a proper description of the magnetism in the system. In previous studies, LDA+U which is equivalent to the HF approach shows that the paramagnetic state is always unstable and the system stays ferromagnetic state throughout the entire doping range [11]. Meanwhile experiments observe single

spin degenerate FS for $x < 0.72$ [12] and that FM order emerges only when x is above 0.75. The FM instability in such a weak-coupling theory is of the Stoner-type, i.e. due to the large density of states combined with the unphysical self-energy corrections that scales with the interaction strength U . Here we address the stability of the paramagnetic state before the emergence of FM. Our basic idea is that the Stoner criteria is strongly renormalized and weakened by correlation effects. In the strong-coupling approach, the interaction strength U that enters the Stoner susceptibility is replaced by the difference in the spin-dependent chemical potential (fugacity) that scales with the average kinetic energy in each spin sector. Our results obtained for the single a_{1g} band t - U - V model in the unrestricted Gutzwiller approximation show that strong correlation makes the paramagnetic state stable against FM order for $x < x_c = 0.67$.

A further exploration for the magnetic properties in the sodium rich region provides a theoretical description of the experimental observations [13, 14, 15] in Chapter 4. At $x = 0.82$, we estimated that the ordered moment detected by neutron scattering [13] is about $0.13 \mu\text{B}$. The physical picture is that the high density of Na atoms enhances the dopant potential which causes a fraction of the doped electrons to localize and form nonmagnetic Co^{3+} . The same argument implies that a fraction of holes will be localized and form $S=1/2 \text{Co}^{4+}$ near the Na vacancy. Indeed this picture is consistent with ^{59}Co and ^{23}Na NMR measurements that find distinct Co and Na sites indicative of $\text{Co}^{4+}/\text{Co}^{3+}$ charge disproportionation in the Na-rich samples [15]. In order to allow inhomogeneous solutions, we propose to develop and advance a spatially unrestricted Gutzwiller approximation (SUGA) in the variational space spanned by spatial and spin dependent renormalization factors. The key to understand this problem is to realize that once the local density is

allowed to be nonuniform, there are an infinite number of unprojected Slater determinant states, each corresponding to a choice of the local fugacity. We found that it is possible to choose the fugacity such that the projection is performed along the path of conserving local densities.

A randomly distributed sodium ion potential has been taken into account. At $x=0.8$ and $x=0.97$, the inhomogeneous charge and spin distributions are presented. Due to the large electrostatic potential fluctuation, it has been presented the coexistence of localized and itinerant electronic states with inhomogeneous FM order, exhibiting nonmagnetic Co^{3+} patches, AF correlated local regions, and FM clusters with AF domain walls. For x close to one, we study the cobaltate from the point of view of a hole-doped band-insulator $\text{Na}_{1-\delta}\text{CoO}_2$. We take into account the superlattice potential of the Na and consider the dilute Na vacancies that dope and tend to trap the doped holes to form local moments.

Lastly in Chapter 5, a special doping $x = 0.84$ in the sodium rich regime is studied based on the single one band model with a_{1g} character on a triangular lattice. A unique sodium ordering of $\sqrt{13} \times \sqrt{13}$ has been found, which imposes the same superstructure on Co accordingly [16]. A state of one local moment and one itinerant carrier has been proposed. The experiment of Shubnikov-de Haas effect also shows much smaller than expected FS pockets [17] at $x = 0.84$, consistent with the proposition of the coexistence of local and itinerant holes. We start with the standpoint of strong correlation plus sodium dopant potential and show the interplay of strong electronic correlation and $\sqrt{13} \times \sqrt{13}$ sodium ordering leads to the semi metal state, where there are 2 holes per supercell, one localized and one itinerant.

Compared to the cuprates, the cobaltate phase diagram covers a much wider doping range from the intermediate $x \sim 0.3$ to high Na concentration $x \sim 0.9$. The diverse electronic properties involving charge, spin, and orbital degrees of freedom as well as the dopant potential as a function of varying sodium concentration x make the cobaltates a very useful and fascinating class of materials to study the physics of electronic correlation.

References

- [1] I. Terasaki, Y. Sasago, and K. Uchinokura, Phys. Rev. B **56**, R12685 (1997)
- [2] Yayu Wang, Nyrisa S. Rogado, R.J. Cava, and N.P. Ong, Nature(London) **423**, 425 (2003)
- [3] K. Takada, et. al., Nature (London) **422**, 53 (2003).
- [4] R. Ray, A. Ghoshray, K. Ghoshray, and S. Nakamura, Phys. Rev. B **59**, 9454 (1999)
- [5] R.E. Schaak, T.Klimczuk, M.L. Foo, and R.J. Cava, Nature(London) **424**, 527 (2003)
- [6] F.C. Chou, J.H. Cho, P.A. Lee, E.T. Abel, K. Matan, and Y.S. Lee, Phys. Rev. Lett. **92**, 157004 (2004)
- [7] R. Jin, B.C. Sales, P. Khalifah, and D. Mandrus, Phys. Rev. Lett. **91**, 217001 (2003)
- [8] M.L. Foo et al., Phys. Rev. Lett. **92**, 247001 (2004).
- [9] John V. Badding, Nature materials, Vol 2, 208 (2003)
- [10] D.J. Singh, Phys. Rev. B **61**, 13397 (2000)
- [11] P. Zhang, W. Luo, M.L. Cohen, and S.G. Louie, PRL **93**, 236402(2004)
- [12] H. B. Yang, et. al., cond-mat/0501403 (2005).
- [13] S.P.Bayrakci et al., Phys. Rev. Lett. **94**, 157205 (2005).
- [14] C. Bernhard, Ch. Niedermayer, A. Drew, G. Khaliullin, S. Bayrakci, J. Stremper, R.K. Kremer, D.P. Chen, C.T. Lin, and B. Keimer, EPL **80**, 27005 (2007).
- [15] I.R. Mukhamedshin, et. al., cond-mat/0703561.

- [16] F.C. Chou, M.-W. Chu, G.J. Shu, T.-T. Huang, Woei Wu Pai, H.S. Sheu, and Patrick A. Lee, PRL **101**, 127404 (2008)
- [17] L. Balicas, Y.J. Jo, G.J. Shu, F.C. Chou, and P.A. Lee, PRL **100**, 126405 (2008)

CHAPTER 2

Electron Correlation and Fermi Surface Topology of Na_xCoO_2

The electronic structure of Na_xCoO_2 revealed by recent photoemission experiments shows important deviations from band theory predictions. The six small Fermi surface pockets predicted by LDA calculations have not been observed as the associated e'_g band fails to cross the Fermi level for a wide range of sodium doping concentration x . In addition, significant bandwidth renormalizations of the t_{2g} complex have been observed. We show that these discrepancies are due to strong electronic correlations by studying the multi-orbital Hubbard model in the Hartree-Fock and strong-coupling Gutzwiller approximations. The quasiparticle dispersion and the Fermi surface topology obtained in the presence of strong local Coulomb repulsion are in good agreement with experiments.

2.1. Theoretical calculation of band structure

Density functional theory (DFT) is a very popular approach used for electronic structure calculation in physics. It is also an *ab initio* method which is based entirely on theory from first principles. DFT introduces a computationally low cost way to solving problems in many body systems, comparing to conventional many-electron wave-function. Meanwhile DFT maintains a satisfactory accuracy when comparing to experiments results. This significant contribution is that it replace the wave-function Ψ of a N-electron system, which has a dimension of $3N$ variables, with a electronic density as a function of \vec{r}

with only 3 variables.

$$(2.1) \quad n(\vec{r}) = N \int d^3r_2 \int d^3r_3 \cdots \int d^3r_N \Psi^*(\vec{r}, \vec{r}_2, \dots, \vec{r}_N) \Psi(\vec{r}, \vec{r}_2, \dots, \vec{r}_N)$$

This moves $E(\Psi)$ to the energy functional

$$(2.2) \quad E(n) = T(n) + U(n) + \int V(\vec{r})n(\vec{r})d^3r$$

This significantly reduces the computational effort needed to calculate and understand the electronic properties of the system. By minimizing the energy functional $E(n)$, the ground state energy E_0 could be obtained. T is the kinetic energy. V is an external potential. U is the electron-electron interaction energy for the N-electron system. The functional $T(n)$ and $U(n)$ are called universal functional, while $V(n)$ is called non-universal functional, as it depends on the system under study. However, one of the main problems of the DFT method is that the exact form of the universal energy density functional is unknown. What we only know is that there exist such a functional in principle. In other words, if we write an effective single-particle potential in a form

$$(2.3) \quad V_s(\vec{r}) = V(\vec{r}) + \int \frac{e^2 n_s(\vec{r}')}{|\vec{r} - \vec{r}'|} d^3r' + V_{XC}[n_x(\vec{r})]$$

$$(2.4) \quad n_s(\vec{r}) \equiv n(\vec{r})$$

if V_s could be written as

$$(2.5) \quad V_s = V + U + (T - T_s)$$

where T_s denotes the non-interacting kinetic energy. V_{XC} is called the exchange-correlation potential and includes all the many-particle interactions.

Since there is no exact expression for the exchange-correlation potential, there are a group of approaches approximate it. This group includes local density approximation (LDA), generalized gradient approximation (GGA), Green's function + screened interaction potential, LDA + U (local density approximation of Hubbard U), LSDA calculation (extends the LDA calculation to include electron spins), *etc.*

Local-density approximation (LDA) was first proposed by Kohn and Sham [1] in 1965 to approximate the exchange correlation energy potential in density functional theory (DFT). LDA methods are exact for slowly varying density system and lead to a self-consistent solution similar to Hartree-Fock equations. Kohn-Sham orbital equations defines the LDA and are written as follows,

$$(2.6) \quad \left[-\frac{1}{2}\nabla^2 + \nu(r) + \int \frac{\rho(r')}{|r-r'|} dr' + v_{xc}^{LDA}(r)\right]\psi_i = \varepsilon_i\psi_i$$

The v_{xc}^{LDA} is the exchange and correlation potential under the local-density approximation.

A LDA calculation of the paramagnetic band structure of $NaCoO_2O_4$ has been performed by Singh [2] in 2000. It was the first LDA calculation on cobaltates. From Fig. 2.1 (b), the t_{2g} manifold has been shown and enlargement of a_{1g} is also displayed.

Fig. 2.1(a) shows the paramagnetic band structure along high symmetry directions Γ, K, M and the corresponding A, L, H points in the $k_z = 0.5$ plane. The $O2p$ extend from approximately -7 eV to -2 eV, relative to the Fermi energy, E_F . Clearly, the $O2p$ is separated from the transition metal d bands lying above, so the hybridization between Co $3d$ and $O2p$ is very weak. The Co $3d$ consists of 5 degenerate orbitals and are crystal

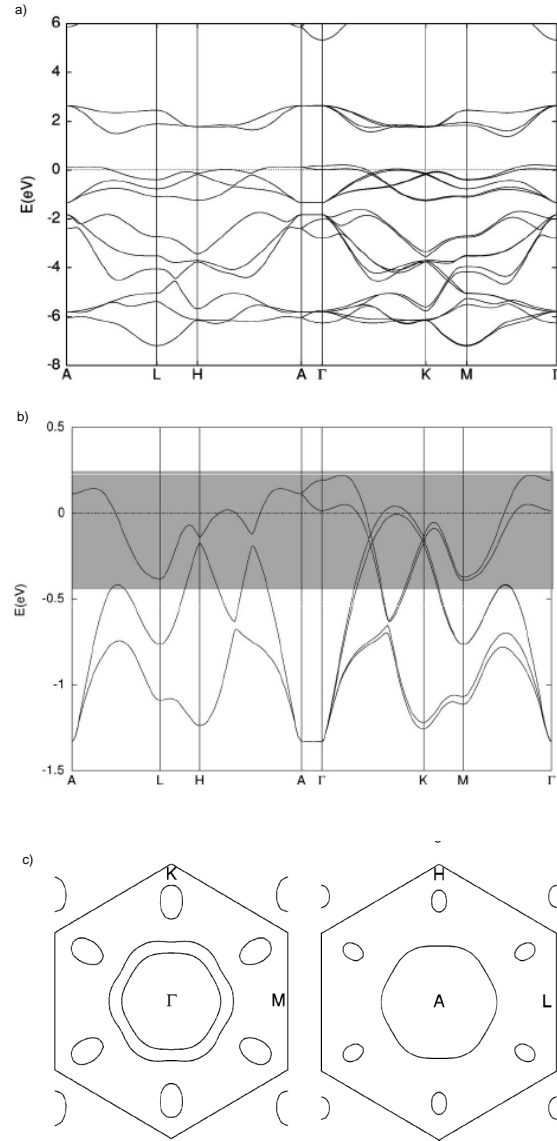


Figure 2.1. LDA prediction of the electronic structure of $NaCo_2O_4$ in paramagnetic state. a) the electronic structure of $NaCo_2O_4$, the horizontal dotted line denotes Fermi energy E_F . b) the enlargement around E_f shows the t_{2g} manifold. c) LDA Fermi surfaces of $NaCo_2O_4$ in the $k = 0$ (on the left) and $k_z = 0.5$ (on the right) planes.

field split in to a lower lying t_{2g} and an upper lying e_g bands in the CoO_6 octahedral environment, which are separated by approximately 2.5 eV. From Fig. 2.1(a), it is shown the e_g band is well separated from t_{2g} due to the narrow band width, and is above E_F . The t_{2g} width is 1.6 eV and the e_g width is 1.2 eV.

In this case, it seems that the t_{2g} manifold will be exclusively responsible for the low energy properties. The trends for other octahedrally coordinated $3d$ transition metal compounds would suggest an effective on-site Hubbard U of $5 \sim 8$ eV. As noted, this manifold of t_{2g} states is quite narrow, and in particular it is in the regime $W \ll U$ with any plausible U . The t_{2g} manifold around E_F is enlarged in Fig. 2.1(b), which is further split in the rhombohedral crystal field into one a_{1g} and two e'_g bands. The amount of splitting is sensitive to the rhombohedral distortion of the O octahedra. The a_{1g} band tops at Γ point and has less electron occupation than e'_g . It has a larger bandwidth but a lower orbital energy than e'_g . One of the e'_g band which lying above the other along $\Gamma - K$ direction is defined as e'_{g1} . The other e'_g band is defined as e'_{g2} . Based on LDA calculation, the band structure is anisotropic. There is more band crossing along the $\Gamma - K$ direction than $\Gamma - M$ direction. Along the $\Gamma - K$ direction, the a_{1g} band hybridizes with the e'_{g2} band, but not with the e'_{g1} band. Along the A-H direction in the $k_z = 0.5$ plane, a_{1g} and e'_{g1} hybridize and open up a gap. In $NaCo_2O_4$ the states at the top of the t_{2g} manifold where E_F sits have dominant a_{1g} character. From Fig. 2.1 in particular, the large cylindrical hole Fermi surfaces around the $\Gamma - A$ direction have dominant a_{1g} character, while the small hole-like sections centred about $2/3$ of the way out on the $\Gamma - K$ and $A - H$ directions have mixed a_{1g} and e'_g character.

Johannes *et al* [3] has shown the *DOS* calculation and Fermi surface at hydrated $Na_{0.3}CoO_2$, in Fig. 2.2. From the *DOS* in Fig. 2.2(a), both a_{1g} and e'_g bands cross the Fermi level, corresponding to the center big pocket and the 6 surrounding small pockets in Fig. 2.2(b), respectively. The e'_g pockets contribute much more to the *DOS* at the Fermi level than the a_{1g} pocket, although the latter one carries 2/3 of all holes. This one-electron susceptibility calculation of hydrated $Na_{1/3}CoO_2$ also finds that the small pockets are strongly nested [3], shown in Fig. 2.2(b). This nesting involves 70% of all electrons at Fermi level and closely commensurates with a $2a \times 2a$ superstructure. This nesting creates a tendency to charge density waves and generates strong spin fluctuations, which can be important for superconductivity.

Meanwhile, K.-W. Lee *et al* [4] also calculated the band structure and corresponding *DOS* based on LDA. Their observation is consistent with Johannes' result [3]. From $NaCoO_2$, the doped holes first go into a_{1g} band. Based on a rigid band structure obtained at $x = 1/3$ in Fig. 2.3, holes enter only a_{1g} states until $x \approx 0.6$, whereupon an e'_g Fermi surface begins to form, whose Fermi surface consists of one center a_{1g} pocket and six e'_g pockets. The a_{1g} character is strong at the bottom and the top of the t_{2g} complex. The *DOS* of a_{1g} is higher than that of the e'_g because of the particular structure and to a much larger effective band width, although its centroid is somewhat lower. Nearly all of the e'_g states lie within a 1.0 eV region and a_{1g} extends over 1.5 eV. The upward dispersion of the a_{1g} band around Γ is affected by interlayer coupling, which can depress the band at $k = 0$.

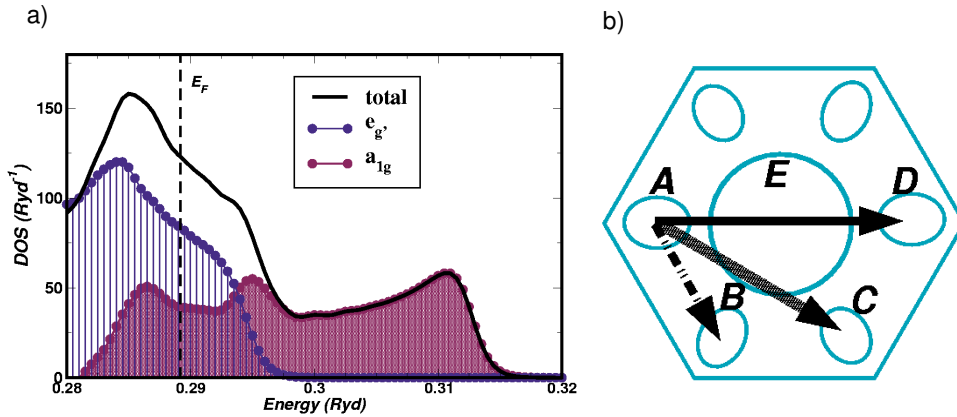


Figure 2.2. a) The density of states of $Na_{0.3}CoO_2 \cdot yH_2O$ and of the two bands crossing the Fermi level. The a_{1g} band, which carries 2/3 of all holes, yields only about 1/3 of $DOS(E_F)$. b) Fermi surface of $Na_{0.3}CoO_2 \cdot yH_2O$ with three main nesting types. Q_1 in a solid line is the perfect nesting, Q_2 in a narrow line and Q_3 in a wide dashed line are shown as imperfect nesting.

2.2. Experimental results of the band structure

Angle-resolved photoemission spectroscopy (ARPES) is a powerful experiment technique to study the electronic structure of a material. Photoelectron spectroscopy is a general term which refers to all techniques based on the photoelectric effect originally observed by Hertz(1887). ARPES is the only truly momentum-resolved probe and it is critical in the study of low dimensional and strongly anisotropic systems. This technique can be used to measure 3 essential attributes of the electrons when studying electrons in

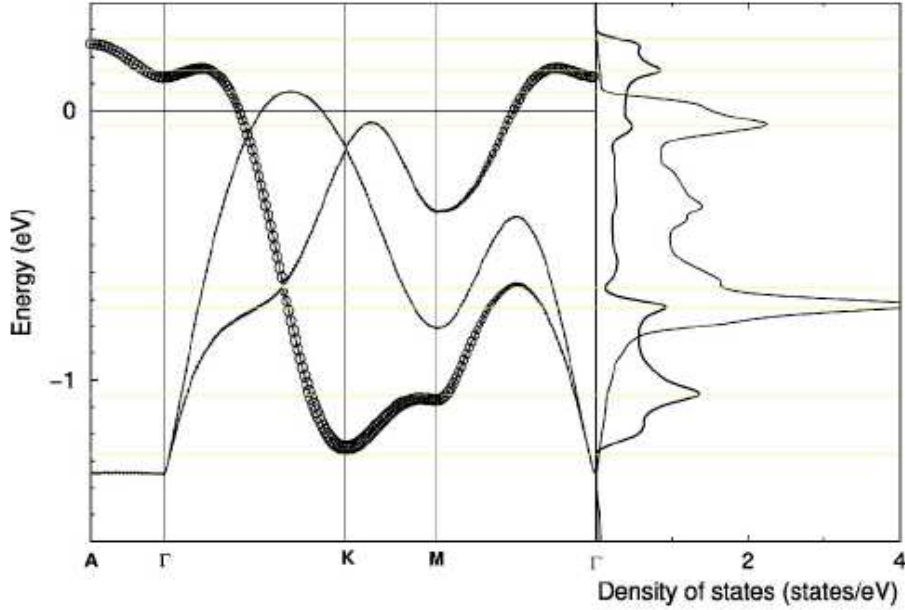


Figure 2.3. Band structure (in the virtual crystal approximation) along high symmetry lines (left panel) and the aligned density of states (right panel) for the $x=1/3$ cobaltate in the local density approximation. The a_{1g} symmetry band is emphasized with circles proportional to the amount of a_{1g} character. The a_{1g} density of states is indicated by the darker line.

a solid: energy, momentum and spin. ARPES has been playing a very important role in the study of high-Tc superconductors. It is also a main probe in the study of the electronic structure of the sodium doped cobaltates. In this section, the ARPES results on the band structure of Na_xCoO_2 will be shown and later it will be compared to the theoretical results discussed in the previous section.

When an incident photon with sufficient energy is incident on a solid, the photoemission process occurs to emit an electron. By the energy conservation law, the kinetic

energy E_k of the emitted electron is given by

$$(2.7) \quad E_k = \hbar\nu - \phi - |E_b|$$

$\hbar\nu$ is the energy of the incident photon, ϕ is the work function of the solid, and E_b is the binding energy of the electron inside the solid.

By measuring momentum and kinetic energy of the electrons photoemitted from a sample illuminated with radiation of energy larger than the material work function, it is possible to gain information on both energy and the momentum of the electronic excitations inside the solid. By collecting these photoelectrons using an electron energy analyzer of a finite acceptance angle, the kinetic energy E_k of photoelectrons can be measured, along a given emission direction. In this case, the momentum of the photoelectrons is also determined. This momentum can be divided into parallel and perpendicular components regarding to the sample surface, $K_{\parallel} = K_x + K_y$ and $K_{\perp} = K_z$, respectively. They are expressed in terms of the polar (θ) and azimuthal (φ) emission angles.

$$(2.8) \quad K_x = \frac{1}{\hbar} \sqrt{2mE_k} \sin\theta \cos\varphi$$

$$(2.9) \quad K_y = \frac{1}{\hbar} \sqrt{2mE_k} \sin\theta \sin\varphi$$

$$K_z = \frac{1}{\hbar} \sqrt{2mE_k} \cos\theta$$

Since the energy and momentum of these final states of outgoing electrons are known, the binding energy of their initial states can be calculated from (2.7). For the momentum of the initial state electrons, the momentum of the photons can be ignored, since it is very small due to the photon energy used in ARPES ($h\nu < 100\text{eV}$). When the system under

study is periodic, $k_{\parallel} = k_{\parallel} + G_{\parallel}$ due to the translational symmetry in the x-y plane. G_{\parallel} is the reciprocal lattice vector. The symmetry is broken along z-axis.

Based on the discussion above, the intensity measured in an ARPES experiment on a 2D single band system can be written as,

$$(2.10) \quad I(\vec{k}, \omega) = I_0(\vec{k}, \nu, \vec{A}) f(\omega) A(\vec{k}, \omega)$$

$\vec{k} = \vec{k}_{\parallel}$ is the in-plane electron momentum. ω is the electron binding energy with respect to the Fermi energy. $I_0(\vec{k}, \nu, \vec{A})$ depends on the electron momentum and the energy and polarization of the incident photon. $f(\omega)$ is the Fermi function $f(\omega) = 1/(e^{\omega/k_B T} + 1)$. $A(\vec{k}, \omega)$ is the one-particle spectral function. $A(\vec{k}, \omega) = -(1/\pi) \text{Im}G(\vec{k}, \omega)$. $G(\vec{k}, \omega)$ is the Green's function describing the propagation of a electron in a many-body system. Thus ARPES can also provide information of many-body interaction in solids.

In principle, the momentum of the electrons can also be obtained as different momentum electrons will escape at different angles from the surface of a material. However, since the electrons are being projected through the surface, the momentum perpendicular to the surface is not conserved. Therefore ARPES is especially attractive in application to quasi-2D materials, where the principle momentum directions of interest are parallel to the surface. In this case direct and complete experimental determination of the band structure becomes possible.

Using ARPES technique, Yang *et al* [5] has pointed out that while the measured Fermi surface is consistent with the large Fermi surface enclosing the Γ point from the band theory, the predicted small Fermi surface pockets about 2/3 way out on in the $\Gamma - K$ point are missing. Also, comparing to the LDA band theory, the observed Fermi velocity

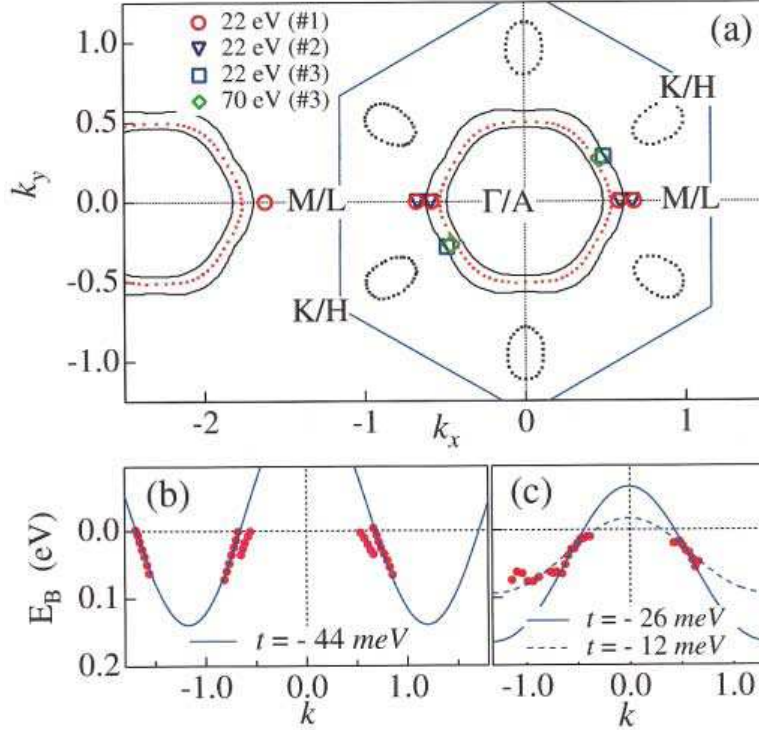


Figure 2.4. a) Measured FS crossing compared to calculated FS in $k_z = 0$ (black solid lines) and $k_z = 0.5$ (red dashed lines) planes. The blue hexagon is the 2D BZ. b) Extracted band positions (red dots) along $\Gamma - M$ and a tight binding fit with $t = -44$ meV. c) Extracted band positions along $\Gamma - K$ (red dots) and two tight binding fits with $t = -12$ meV (solid line) and $t = -26$ meV.

near E_F band is renormalized and anisotropic along two principle axes ($\Gamma - M, \Gamma - K$). The Fermi velocity is reduced by a factor of 3 long $\Gamma - M$, and 5-10 along $\Gamma - K$, shown in Fig. 2.4.

In Yang *et al*'s further study, they investigated a wide range of Na concentration from $x = 0.3$ to $x = 0.72$. In all these metallic samples at different x , only a single hole-like Fermi surface centred around Γ is observed. The single pocket found in the

study also obeys the Luttinger theorem, in which the area of pockets changes with x , shown in Fig. 2.5. They also observed a dispersion that lies below and never crosses the Fermi level, shown by the black triangular markers in Fig. 2.5(f). In addition, the top of this dispersion below E_F shown in Fig. 2.5(g) is essentially temperature independent. This feature rules out the possibility that the e'_{g1} band is gapped and what is observed in ARPES is just the leading-edge associated with the gap opening. Thus, they argued that the small FS pockets near the K point predicted by the LDA calculations are found to sink below E_F with a distance to the Fermi sea almost independent of doping and temperature.

Consistent with Yang's observation, Hasan *et al* also investigated on $Na_{0.7}CoO_2$ and showed that first, only a hole-type Fermi surface is present, Fig. 2.6(a,b). Secondly, the quasiparticle band is highly renormalized with a small Fermi velocity. This is reflected in Fig. 2.6(c). The band is extrapolated to the zone boundary to get a measure for bandwidth. The value of the bandwidth is between 70 and 100 meV. Lastly, the resonant scattering of valence excitations indicates a large Hubbard $U \sim 5$ eV, which supports the strongly correlated nature of the system.

In conclusion, in ARPES experiments, the intensities of a_{1g} and e'_g bands have different dependence on the photon energy. The character of each band can be identified by studying its photon energy dependence in the ARPES intensity. One can obtain the complete band dispersions of t_{2g} complex in Na_xCoO_2 by repeating the measurement at many photon energy levels. One detailed band structure evolution is shown by Yang *et al* [6] and the bandwidth is renormalized approximately by a factor of 2. The outstanding discrepancies between LDA prediction and ARPES observations are that, first, the e'_g

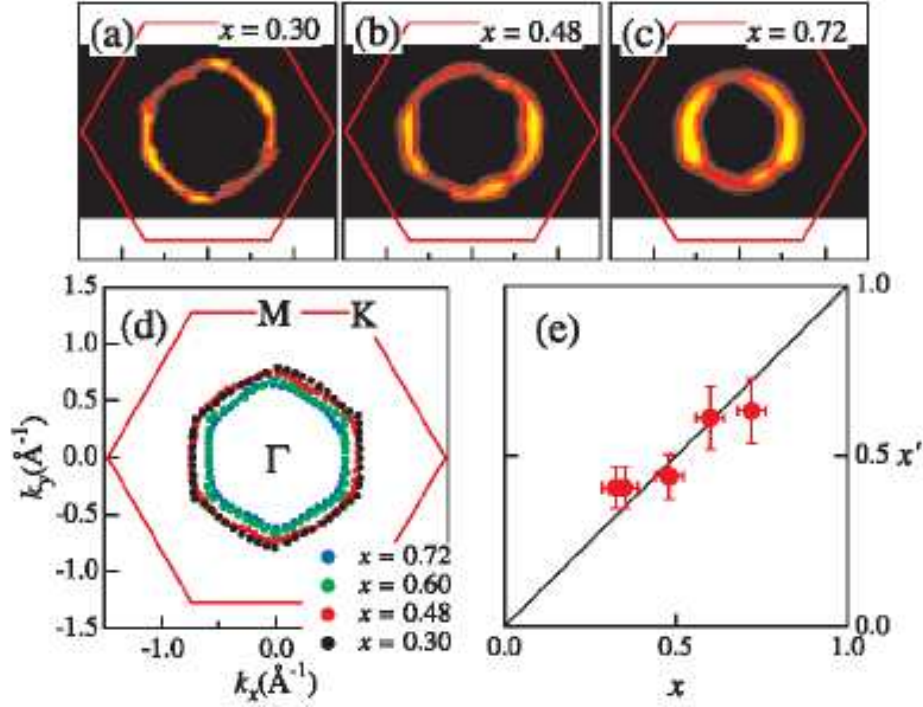


Figure 2.5. FS evolution in Na_xCoO_2 . a)-c) Fermi surface intensity contours at $x = 0.3, 0.48$, and 0.72 in the 1st Brillouin zone. d) Overlap of the FS locations at different doping levels. e) Effective Na concentration x' derived from FS area *vs* Na concentration x . The diagonal line is from the Luttinger theorem.

FS pockets predicted by LDA along $\Gamma - K$ direction are never observed by ARPES. In ARPES, the e'_{g1} band approaches but never reaches E_F . The absence of e'_g pockets is also demonstrated in the hydrated superconducting sample [7]. Secondly, the bandwidth of the t_{2g} complex is much smaller in ARPES measurement than what is predicted by LDA calculation. Also, the narrow manifold of t_{2g} states shows Na_xCoO_2 is in the strongly correlated regime, $W \ll U$, for any plausible U . U is predicted to be 5~8 eV [8] and

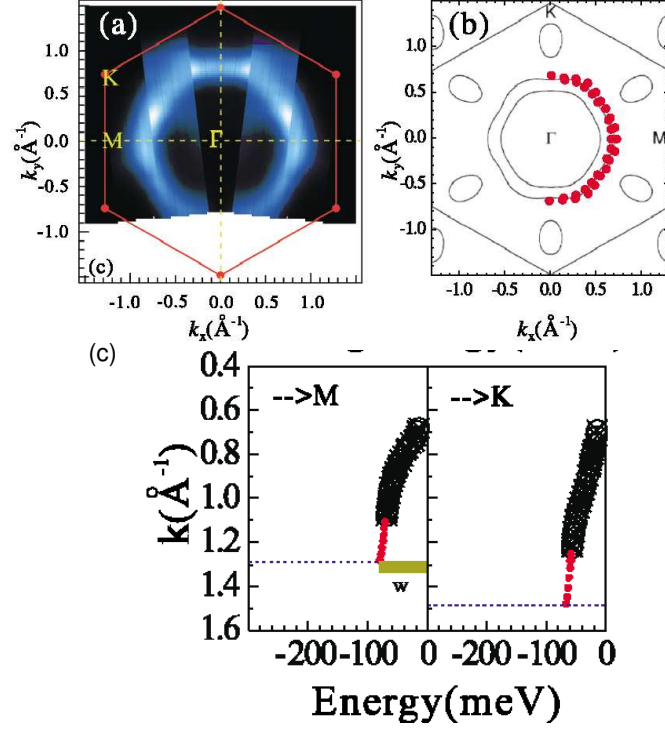


Figure 2.6. a) n_k plot generated by integrating within 75 meV of Fermi level. A hole pocket is centred around the Γ point. b) Comparison with LDA calculation on $NaCo_2O_4$. Red dots indicate the location of measured Fermi crossing in $Na_{0.7}CoO_2$. c) E vs k plots based on the extracted peak positions in $\Gamma - M$ (left) and $\Gamma - K$ (right) directions.

measured to be around 5 eV [9]. All the properties obtained above suggest that the strong electronic correlation play an important role in Na_xCoO_2 .

2.3. Electron correlation and Fermi surface topology

The cobaltates (Na_xCoO_2) are doped 3d transition metal oxides in which the Co atoms form a layered hexagonal lattice structure. In contrast to the high- T_c cuprates, where the Cu^{2+} has a $3d^9$ configuration and occupies the highest *single* e_g ($d_{x^2-y^2}$) orbital near the

Fermi level, the cobaltates are *multi-orbital* systems where the Co^{4+} is in the $3d^5$ configuration, occupying the three lower t_{2g} orbitals, similar to the ruthenates (Sr_2RuO_4). The unexpected discovery [10] of a superconducting phase of yet unknown origin in hydrated Na_xCoO_2 around $x \sim 0.3$ has generated renewed interests in this material. However, such basic issues as the low energy electronic structure and Fermi surface topology in the cobaltates have not been well understood. Band structure (LDA) calculations [11] find that the trigonal symmetry of the Co site in the triangular lattice splits the t_{2g} complex into an a_{1g} and two degenerate e'_g states at the zone center (Γ point). The LDA predicts a large Fermi surface (FS) associated with the a_{1g} band enclosing the Γ point and, interestingly, six small FS pockets of mostly e'_g character near the K points [2, 4].

However, recent angle-resolved photoelectron spectroscopy (ARPES) measurements on the cobaltates revealed, remarkably, only a *single* hole-like FS centered around the Γ point for a wide range of Na concentration x [5, 9, 12]. The area enclosed by the FS exhausts the Luttinger volume, which is consistent with the observation that the dispersion of the e'_g bands associated with the LDA FS pockets lies below and never crosses the Fermi level [5]. The absence of the FS pockets is unexpected and puts serious constraints on several proposed theories of non-phonon mediated superconductivity as well as magnetic properties based on the nesting conditions of the Fermi pockets [3, 13, 14]. Furthermore, the measured quasiparticle bandwidths are significantly narrower than the LDA predictions [5]. These fundamental discrepancies between ARPES and LDA suggest that the effects of strong electronic correlations are important in the cobaltates. The effects of local Coulomb repulsion U have been considered in the LSDA+U approach, which indeed finds the absence of the small FS pockets [15]. However, the latter is tied to

the fully polarized ferromagnetic state in the LSDA+U theory that gives spin-split bands and spin polarized FS with an area twice as large. This is inconsistent with ARPES and likely an artifact of the LSDA+U approximation. A recent calculation based on the multi-orbital Hubbard model and the dynamical mean-field theory finds that the FS pockets become even larger in size than the LDA predictions [16].

How strong correlations drive orbital polarization and the band narrowing observed in ARPES are the focus of the present work. We adopt a generic multi-orbital Hubbard model description where the noninteracting part is determined by fitting the LDA band structure. The interacting part contains both the intra (U) and the inter-orbital (U') local Coulomb repulsion as well as the Hund's rule coupling J_H .

First, a basis independent Hartree-Fock (HF) calculation is performed which is in essence a LDA+U calculation in the paramagnetic phase. We find that for small U' , the HF self-energy renormalizes the atomic level spacing in such a way that the size of the small FS pockets associated with the e'_g band grows. Physically, this reflects the fact that, multi-orbital occupation is favored through double occupancy since $U > U'$ on general grounds. This trend is however reversed when U' grows large and double occupancy becomes energetically costly. In the HF theory, the size of the e'_g FS pockets begins to shrink for $U'/U > 3/5$. To correctly capture the physics of strong correlation for large U and U' , we generalize the Gutzwiller approximation to the case of multi-orbitals. We find that in the strong-coupling regime, orbital polarization is tied to Pauli-blocking, i.e. the orbital occupation dependence of the Gutzwiller band renormalization factors. We obtain both band narrowing and the disappearance of the FS pockets in good agreement with the ARPES experiments.

The non-interacting Hamiltonian is a multi-orbital tight-binding model on a 2-dimensional triangular lattice.

$$(2.11) \quad H_0 = - \sum_{ij,\sigma} \sum_{\alpha\beta} t_{ij,\alpha\beta} d_{i\alpha\sigma}^\dagger d_{j\beta\sigma} - \frac{\Delta}{3} \sum_{i,\sigma} \sum_{\alpha\neq\beta} d_{i\alpha\sigma}^\dagger d_{i\beta\sigma},$$

where the operator $d_{i\alpha\sigma}^\dagger$ creates an electron in the α orbital with spin σ on the Co site i and $t_{ij,\alpha\beta}$ is the hopping integral between the α orbital on site i and the β orbital on site j . The relevant valence bands near the FS consist of the Co $t_{2g} = \{d_{xy}, d_{yz}, d_{zx}\}$ orbitals and have an electron occupancy of $5 + x$. The Δ in Eq. (2.11) describes the crystal field due to trigonal distortion that splits the t_{2g} complex into a lower a_{1g} singlet and a higher e'_g doublet, where $a_{1g} = (d_{xy} + d_{yz} + d_{zx})/\sqrt{3}$, and $e'_g = \{(d_{zx} - d_{yz})/\sqrt{2}, (2d_{xy} - d_{yz} - d_{zx})/\sqrt{6}\}$. d_{xy}, d_{yz}, d_{zx} orbitals are degenerate and the band structure has six fold symmetry. On the triangular lattice, hopping integrals $t_{i,j}$ are anisotropic. Subscript i denotes the i th nearest neighbour hopping, which j denotes the direction of the hopping. For example, in the first nearest neighbour hopping, each site has 3 equivalent hopping directions. Intra-orbital hopping integral $t_{1,1} \neq t_{1,2} = t_{1,3}$, while inter-orbital hopping shows $t'_{1,1} \neq t'_{1,2} = t'_{1,3}$.

For convenience, we will work in the hole-picture via a particle-hole transformation, in which the band filling is $1 - x$. The structure of the tight-binding Hamiltonian in k-space on the triangular lattice is

$$(2.12) \quad H_0 = \sum_{k,\sigma} \sum_{\alpha\beta} \mathbf{K}_{\alpha\beta}^d(k) d_{k\alpha\sigma}^\dagger d_{k\beta\sigma} + \frac{\Delta}{3} \sum_{k,\sigma} \sum_{\alpha\neq\beta} d_{k\alpha\sigma}^\dagger d_{k\beta\sigma}.$$

The hopping matrix \mathbf{K} in the t_{2g} basis is given by

$$(2.13) \quad \mathbf{K}^d(k) = \begin{pmatrix} \varepsilon(t, 1, 2, 3) & \varepsilon(t', 3, 1, 2) & \varepsilon(t', 2, 3, 1) \\ \varepsilon(t', 3, 1, 2) & \varepsilon(t, 2, 3, 1) & \varepsilon(t', 1, 2, 3) \\ \varepsilon(t', 2, 3, 1) & \varepsilon(t', 1, 2, 3) & \varepsilon(t, 3, 1, 2) \end{pmatrix},$$

with $(1, 2, 3) = (k_1, k_2, k_3)$ and due to the intra-orbital and inter-orbital integrals symmetry discussed above,

$$(2.14) \quad \begin{aligned} \varepsilon(t, 1, 2, 3) &= 2t_1 \cos k_1 + 2t_2(\cos k_2 + \cos k_3) \\ &+ 2t_3 \cos(k_2 - k_3) + 2t_4[\cos(k_3 - k_1) + \cos(k_1 - k_2)] \\ &+ 2t_5 \cos(2k_1) + 2t_6[\cos(2k_2) + \cos(2k_3)] + \dots \end{aligned}$$

Here $k_1 = \sqrt{3}k_x/2 - k_y/2$, $k_2 = k_y$, $k_3 = -k_1 - k_2$, and (t, t') denote the (intra,inter)-orbital hopping respectively.

The hopping integrals $t_{ij,\alpha\beta}$ and Δ are fitted to LDA band dispersion. The fitting results up to different nearest neighbours are plotted in Fig. 2.7 showing the fitting of the tight-binding dispersions obtained by diagonalizing Eq. (2.12) to the LDA band structure at $x=1/3$ [4]. We note that the fit with up to third-nearest-neighbor (NN) hopping or more describes the LDA bands quite well. On the other hand, the tight-binding model cannot reproduce completely the LDA dispersions even with up to eighth-NN hopping. The discrepancy is most pronounced along the M-K direction where the two e'_g bands cross in the tight-binding fit (Fig. 1 (a)). Similar disagreement can be traced back to the previous tight-binding fits [3, 14, 16]. We believe the difficulty arises from the hopping

path via the O 2s and 2p orbitals. In another word, this is because the Oxygen is ignored. If the oxygen is present, the tilt of Oxygen Octahedral will break the reflection symmetry along z-axis, and resolve this problem. Nevertheless, the tight-binding model works very well at low energies near the Fermi level. The FS consists of a cylindrical sheet around the Γ -point and six hole pockets near the K-points as shown in Fig. 1(b)-(d). The central FS has a dominant a_{1g} character while the six FS pockets are mainly of the e'_g character. The hopping integrals obtained from the fit with up to third-NN are $t=(-0.045, -0.009, 0.036, 0.006, 0.058, 0.037)$ eV and $t'=(-0.158, -0.030, 0.037, 0.009, -0.012, -0.021)$ eV. The crystal-field splitting Δ is chosen to be 0.01eV, an estimate from the LDA magnetic susceptibility [8]. In the rest of the paper, we use these parameters for H_0 . Note that although holes are evenly distributed among the three degenerate t_{2g} orbitals, in the a_{1g} and e'_g basis (hereafter referred to as the $\{a\}$ basis), the hole occupations are 0.123 (e'_g) and 0.421 (a_{1g}) respectively. However, holes favor the occupation of the a_{1g} orbital not because of its (actually higher than e'_g by Δ) atomic level, but rather its larger bandwidth.

The correlation effects are described by the generic multi-orbital Hubbard model $H = H_0 + H_I$, where H_0 is the tight-binding Hamiltonian in Eq. (2.12) and H_I represents the local Coulomb repulsion U (intra-orbital) and U' (inter-orbital), Hund's rule coupling J_H , and pair hopping integral J_P ,

$$\begin{aligned}
 (2.15) \quad H_I &= U \sum_{i,\alpha} \hat{n}_{i\alpha\uparrow} \hat{n}_{i\alpha\downarrow} + (U' - \frac{1}{2} J_H) \sum_{i,\alpha>\beta} \hat{n}_{i\alpha} \hat{n}_{i\beta} \\
 &- J_H \sum_{i,\alpha\neq\beta} \mathbf{S}_{i\alpha} \cdot \mathbf{S}_{i\beta} + J_P \sum_{i,\alpha\neq\beta} a_{i\alpha\uparrow}^\dagger a_{i\alpha\downarrow}^\dagger a_{i\beta\downarrow} a_{i\beta\uparrow}.
 \end{aligned}$$

Here $\hat{n}_{i\alpha}$ and $\mathbf{S}_{i\alpha}$ are the density and the spin operators in the $\{a\}$ basis of atomic orbitals a_{1g} and e'_g . In this basis, the tight-binding part H_0 is

$$(2.16) \quad H_0 = \sum_{k,\sigma} \sum_{\alpha\beta} \mathbf{K}_{\alpha\beta}^a(k) a_{k\alpha\sigma}^\dagger a_{k\beta\sigma} + \sum_{k,\alpha,\sigma} \Delta_\alpha a_{k\alpha\sigma}^\dagger a_{k\alpha\sigma},$$

where $\Delta_\alpha = -\Delta/3, 2\Delta/3$ for the e'_g and a_{1g} orbitals respectively. The hopping matrix $\mathbf{K}^a(k) = \mathbf{O}^T \mathbf{K}^d(k) \mathbf{O}$, with \mathbf{O} the orthogonal rotation from the t_{2g} to the $\{a\}$ basis.

$$(2.17) \quad \mathbf{O} = \begin{pmatrix} 0 & -1/\sqrt{2} & 1/\sqrt{2} \\ 2/\sqrt{6} & -1/\sqrt{6} & -1/\sqrt{6} \\ 1/\sqrt{3} & 1/\sqrt{3} & 1/\sqrt{3} \end{pmatrix}.$$

The interacting Hamiltonian H_I is identical in these two bases of the t_{2g} complex provided that $J_H = J_P \equiv J$ and $U = U' + J_H + J_P = U' + 2J$ [17]. The hierarchy of the interaction strength is $U > U' > J \geq 0$.

We first study the effects of interactions in the HF theory in the orbital sector. In the paramagnetic phase, the interacting Hamiltonian is thus given by,

$$(2.18) \quad \begin{aligned} H_I^{HF} &= \sum_{k,\sigma,\alpha} \left(\frac{1}{2} U n_\alpha + U'_{\text{eff}} \sum_{\beta \neq \alpha} n_\beta \right) a_{k\alpha\sigma}^\dagger a_{k\alpha\sigma} \\ &+ \left(J - \frac{U'_{\text{eff}}}{2} \right) \sum_{k,\sigma,\alpha \neq \beta} n_{\alpha\beta} a_{k\alpha\sigma}^\dagger a_{k\beta\sigma} - \frac{U}{4} \sum_{k,\alpha} n_\alpha^2 \\ &- \frac{U'_{\text{eff}}}{2} \sum_{k,\alpha \neq \beta} n_\alpha n_\beta - \frac{1}{2} \left(J - \frac{U'_{\text{eff}}}{2} \right) \sum_{k,\alpha \neq \beta} n_{\alpha\beta}^2, \end{aligned}$$

where $n_{\alpha\beta} = (1/N_s) \sum_{k,\sigma} n_{\alpha\beta}^\sigma(k)$, $n_{\alpha\beta}^\sigma(k) = \langle a_{k\alpha\sigma}^\dagger a_{k\beta\sigma} \rangle$, $n_\alpha = n_{\alpha\alpha}$, and $U'_{\text{eff}} = U' - J/2$. In essence, this HF analysis is equivalent to the LDA+U theory [18]. Since we are interested

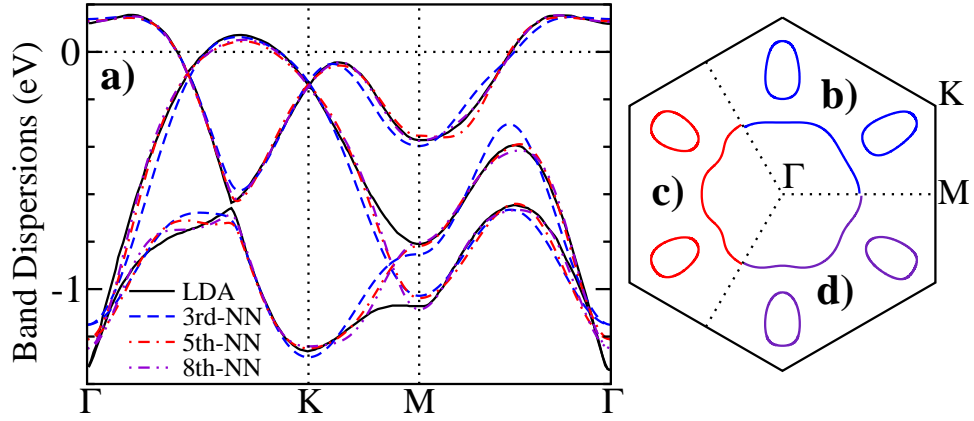


Figure 2.7. Tight-binding fits to the LDA band structure at $x = 1/3$. a) The fitted band dispersions with up to 3rd, 5th and 8th NN hopping. The corresponding Fermi surfaces are plotted in b), c), and d) respectively.

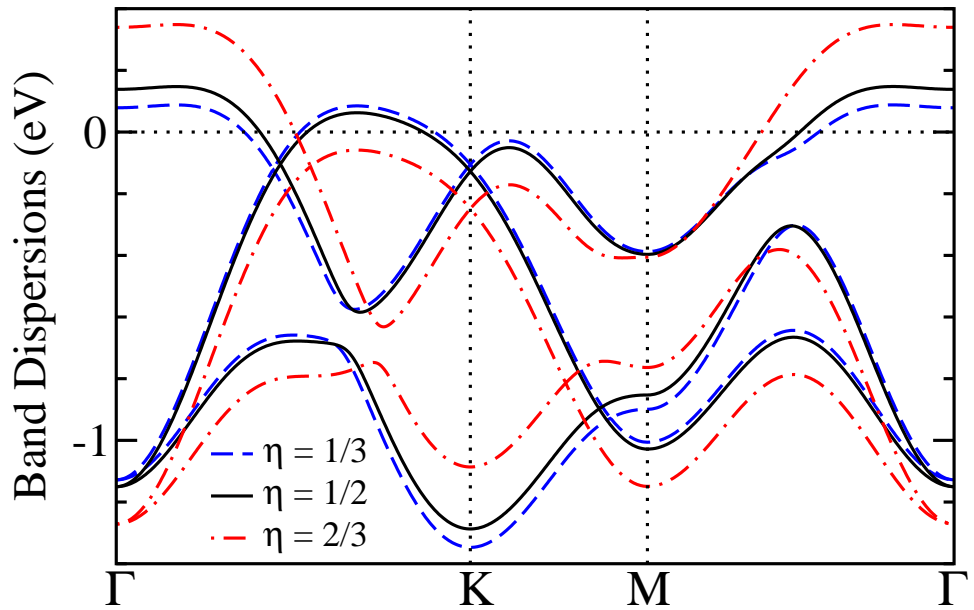


Figure 2.8. HF results for $U = 3.0 \text{ eV}$ at $x = 1/3$. a) The band dispersions for $\eta = 1/3, 1/2, 2/3$, and b) the η dependence of the HF and kinetic energies and the renormalized atomic level spacing Δ' .

in the orbital dependent corrections, eliminating the double counting term for orbital independent interaction effects included in the LDA is not important for our results. Note that the HF theory is basis independent. It is thus convenient to stay in the $\{a\}$ basis where the local density matrix, and thus the HF self-energies are diagonal in orbital space, i.e. $n_{\alpha \neq \beta} = 0$.

In terms of the average $\bar{n} = (n_{a_{1g}} + 2n_{e'_g})/3 = (1 - x)/3$ and the difference $\delta = (n_{a_{1g}} - n_{e'_g})/3$ between the hole occupation of the a_{1g} and e'_g orbitals, the HF self-energy is given by

$$(2.19) \quad \Sigma_{e'_g}^{\text{HF}} = \frac{1}{2}\bar{n}U(1 + 4\eta) - \frac{1}{2}\delta U(1 - 2\eta),$$

$$(2.20) \quad \Sigma_{a_{1g}}^{\text{HF}} = \frac{1}{2}\bar{n}U(1 + 4\eta) + \delta U(1 - 2\eta),$$

where $\eta = U'_{\text{eff}}/U$ is the relative strength of the inter-orbital interaction. The interaction effect in the paramagnetic HF theory is to simply shift the atomic levels by $\Sigma_{e'_g}^{\text{HF}}$ and $\Sigma_{a_{1g}}^{\text{HF}}$ respectively, resulting in a renormalized atomic level spacing $\Delta' = \Delta - 3\delta U(\eta - 1/2)$. Interestingly, the direction of the charge transfer depends on the ratio η . Since the majority of the holes resides in the a_{1g} orbital in the noninteracting limit, $\delta > 0$, Thus, for $\eta < 1/2$, the level splitting renormalizes upward, $\Delta' > \Delta$, and interactions induce a transfer of carriers from the a_{1g} to the e'_g orbital. The self-consistent HF results are shown in Fig. 2.8(a) at $x = 1/3$ for $U = 3\text{eV}$ which is close to the value (3.7eV) estimated from the LDA [19]. For $\eta = 1/3$, the size of the hole pockets indeed becomes larger than that of the noninteracting/LDA ones. Physically, for weak correlations, in order to minimize the interaction energy due to double occupancy, multi-orbital occupation is favored to take advantage of the smaller intra-orbital Coulomb repulsion U' compared to

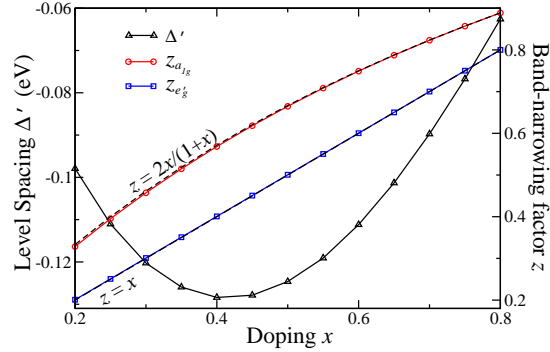


Figure 2.9. The doping x dependence of the bandwidth renormalization and the level spacing between a_{1g} and e'_g orbitals.

the larger U . This tendency must stop, however, with increasing U and U' as it becomes energetically costly to doubly occupy a site. This corresponds to increasing the value of $\eta \leq 1$. Interestingly, at $\eta = \eta_0 = 1/2$ ($U'/U = 3/5$), the self-energy corrections are equal among the orbitals. The level splitting is thus unrenormalized, $\Delta' = \Delta$. There is no interaction induced charge transfer such that the noninteracting (LDA) band dispersions and the Fermi surfaces remain unchanged as shown in Fig. 2(a). When $\eta > 1/2$, i.e. $U'/U > 3/5$, the level splitting renormalizes downward, $\Delta' < \Delta$, triggering a transfer of holes from the e'_g to the a_{1g} orbital. This leads to a reduction in the hole occupation in the e'_g band and hence a reduction in the area of the FS pockets. The six FS pockets continues to shrink as the e'_g band sinks with increasing η and disappears beyond a critical ratio η_c , as shown in Fig. 2a for $\eta = 2/3$. We find that $\eta_c(U = 3.0\text{eV}) \simeq 5/8$.

The HF analysis shows that the disappearance of the six FS pockets near the K-points is the physics of large U and U' . In this case, the HF theory itself becomes unreliable. Moreover, the localization tendency leading to the bandwidth reduction cannot be captured by the HF theory. It is therefore instructive to study the problem in the strong-coupling limit by projecting out the states of double-occupation prohibited by the large on-site Coulomb repulsions. This can be achieved by Gutzwiller projection in the

grand canonical ensemble. The projected wavefunction is expressed as

$$(2.21) \quad |\Psi\rangle = P_G |\Psi_0\rangle$$

where P_G is the projection operator,

$$(2.22) \quad P_G = \prod_{i,\alpha \neq \beta} \prod_{\sigma\sigma'} y_{i\alpha}^{n_\alpha} (1 - n_{i\uparrow\alpha} n_{i\downarrow\beta}) (1 - n_{i\sigma\alpha} n_{i\sigma'\beta})$$

P_G removes the double occupancy by electrons from both the same and different orbitals of the noninteracting state $|\Psi_0\rangle$. $|\Psi_0\rangle$ is an unprojected Slater determinant state. $y_{i\alpha}^{n_\alpha}$ is the local fugacity that maintains the equilibrium of the local densities upon projection. This variational procedure is most conveniently implemented in the Gutzwiller approximation where the effect of projection is taken into account by the statistical weighting factor multiplying the quantum coherent state [20]. Specifically,

$$(2.23) \quad \langle \Psi | a_{i\alpha\sigma}^\dagger a_{j\beta\sigma} | \Psi \rangle = g_t^{\alpha\beta} \langle \Psi_0 | a_{i\alpha\sigma}^\dagger a_{j\beta\sigma} | \Psi_0 \rangle,$$

where the Gutzwiller renormalization factor g_t is given the ratio of the probabilities in the hopping process in the projected $|\Psi\rangle$ and the unprojected $|\Psi_0\rangle$. We find,

$$(2.24) \quad g_t^{\alpha\beta} = \frac{x}{\sqrt{(1 - n_{i\alpha\sigma})(1 - n_{j\beta\sigma})}}.$$

It is important to note that in a multi-orbital system $g_t^{\alpha\beta}$ depends on the occupation of the orbitals connected by the hopping integral as seen in the denominator in Eq. (2.24). The latter originates from the Pauli principle and represents the effects of ‘‘Pauli-blocking’’ of double occupation by electrons in the same quantum states that should be separated

from the ‘‘Coulomb-blocking’’ due to the large on-site U . It turns out that this factor is crucial for carrier transfer and orbital-polarization in the strong-coupling limit. In the uniform paramagnetic phase, the Gutzwiller factor becomes

$$(2.25) \quad g_t^{\alpha\beta} = 2x / \sqrt{(2 - n_\alpha)(2 - n_\beta)}$$

The orbital occupations are variational parameters determined by minimizing the ground state energy of the Hamiltonian,

$$(2.26) \quad \begin{aligned} H_{GW} = & \sum_{k,\sigma,\alpha\beta} g_t^{\alpha\beta} \mathbf{K}_{\alpha\beta}^a(k) a_{k\alpha\sigma}^\dagger a_{k\beta\sigma} + \sum_{i,\alpha,\sigma} \Delta_\alpha a_{i\alpha\sigma}^\dagger a_{i\alpha\sigma} \\ & + \sum_{i,\alpha} \epsilon_{i\alpha} \left(\sum_{\sigma} a_{i\sigma\alpha}^\dagger a_{i\sigma\alpha} - n_{i\alpha} \right), \end{aligned}$$

where $\epsilon_{i\alpha}$ are the Lagrange multipliers enforcing $n_{i\alpha} = \sum_{\sigma} \langle a_{i\sigma\alpha}^\dagger a_{i\sigma\alpha} \rangle$, and are determined by the self-consistency equation

$$(2.27) \quad \epsilon_\alpha = \frac{1}{2} - n_\alpha \frac{1}{N_s} \sum_{k,\beta,\sigma} g_t^{\alpha\beta} \mathbf{K}_{\alpha\beta}^a \langle a_{k\alpha\sigma}^\dagger a_{k\beta\sigma} \rangle.$$

In contrast to the HF theory, both the band-narrowing and the renormalization of the level spacing $\Delta' = \Delta + \epsilon_{a_{1g}} - \epsilon_{e'_g}$ contribute to the redistribution of holes among the orbitals. In Fig. 2.10, we show the self-consistently determined band-narrowing factor $z_\alpha = g_t^{\alpha\alpha}$ and the renormalized level spacing. For orbitals with a larger hole occupation, the bandwidth reduction is smaller and the renormalized band energy is lower, resulting in the transfer of more holes into these bands. The combined effects cause the holes to move out of the e'_g band into the a_{1g} band. The calculated band dispersions and the FS topology at $x = 0.3, 0.5, 0.7$ are shown in Fig. 2.10 in the strong coupling theory. The

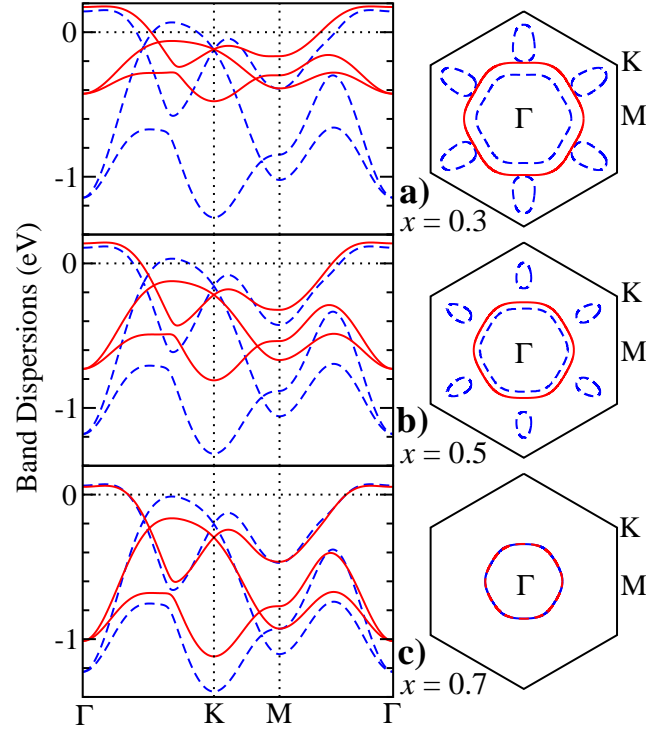


Figure 2.10. The band dispersions and the Fermi surfaces in the strong coupling limit (red solid lines) for doping $x = 0.3, 0.5$ and 0.7 . The results in non-interacting limit (blue dashed lines) are also plotted for comparison.

corresponding non-interacting case is also shown for comparison. The six hole pockets are completely absent at all levels of sodium dopings due to strong correlation, leaving a single hexagonal Fermi surface centered around the Γ point satisfying the Luttinger theorem. This, as well as the band-narrowing due to strong Coulomb repulsion, is in very good agreement with the photoemission experiments [5, 12, 21].

A detailed comparison of band structure between ARPES and LDA + large- U is shown in Fig. 2.11 at doping $x = 0.3$ 0.75 [21]. As expected on fundamental t_{2g} symmetry consideration, lower lying e'_g bands are met at Γ point. This is consistent with our result. Along $\Gamma - M$ direction, 2 lower lying bands are observed and well separated from the a_{1g} band crossing Fermi surface. This band behavior also agrees between experiment and theory. Along $\Gamma - K$ direction, as opposed to the theory, the experiment suggests that a

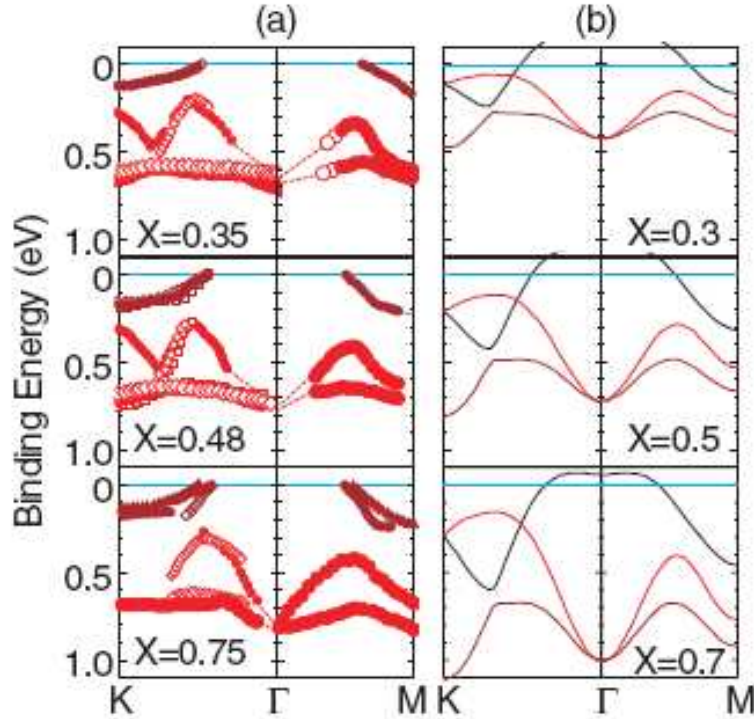


Figure 2.11. Experiment *v.s.* theory [21]: Comparison of a) experimental band structure for $x = 0.35$, $x = 0.48$, and $x = 0.75$ with b) LDA + large- U calculation.

gap formed between the a_{1g} band and the upper e'_g band to avoid crossings. In general, the disappearance of 6 e'_g pockets and band-narrowing due to strong Coulomb repulsion from the experiment observation is in good agreement with the theoretical calculation.

In conclusion, we have shown that strong electronic correlation plays an important role in understanding the electronic structure of Na_xCoO_2 . The strong local Coulomb repulsion pushes the e'_g band below the Fermi level, leading to an orbital polarized state with a single hole-like FS. The absence of the small FS pockets, which would contribute significantly to the density of states in band structure calculations, further suggests that

the large mass enhancement observed in the specific heat measurement [22] is due to strong electronic correlation.

References

- [1] W. Kohn, and L. J. Sham, Phys. Rev. **140**, A1133 (1965).
- [2] D. J. Singh, Phys. Rev. B **61**, 13397 (2000).
- [3] M. D. Johannes, I. I. Mazin, D. J. Singh, and D. A. Papaconstantopoulos, Phys. Rev. Lett. **93**, 097005 (2004).
- [4] K.-W. Lee, J. Kuneš, and W. E. Pickett, Phys. Rev. B **70**, 045104 (2004).
- [5] H. B. Yang, et. al., cond-mat/0501403 (2005).
- [6] H. B. Yang, Angle-resolved photoemission spectroscopy study on Na_xCoO_2 . Ph. D thesis, Boston College (2005)
- [7] T. Shimojima, K. Ishizaka, S. Tsuda, T. Kiss, T. Yokoya, A. Chainani, S. Shin, P. Badica, K. Yamada, and K. Togano, Phys. Rev. Lett. **97**, 267003 (2006)
- [8] D. J. Singh, Phys. Rev. B **68**, 020503(R) (2003).
- [9] M. Z. Hasan, et. al., Phys. Rev. Lett. **92**, 246402 (2004).
- [10] K. Takada, et. al., Nature (London) **422**, 53 (2003).
- [11] D.J. Singh, Phys. Rev. B **61**, 13397 (2000)
- [12] H. B. Yang, et. al., Phys. Rev. Lett. **92**, 246403 (2004).
- [13] K. Kuroki, Y. Tanaka, and R. Arita, Phys. Rev. Lett. **93**, 077001 (2004).
- [14] Y. Yanase, M. Mochizuki, and M. Ogata, J. Phys. Soc. Jpn. **74** (2005); M. Mochizuki, Y. Yanase, and M. Ogata, cond-mat/0407094.
- [15] P. Zhang *et al.*, Phys. Rev. Lett. **93**, 236402 (2004).

- [16] H. Ishida, M. D. Johannes, and A. Liebsch, cond-mat/0412654.
- [17] C. Castellani, C. R. Natoli, and J. Ranninger, Phys. Rev. B **18**, 4945 (1978)
- [18] A. I. Liechtenstein, V. I. Anisimov, and J. Zaanen, Phys. Rev. B **52**, R5467 (1995).
- [19] M. D. Johannes, D. A. Papaconstantopoulos, D. J. Singh, and M. J. Mehl, Europhys. Lett. **68**, 433 (2004).
- [20] F. C. Zhang, C. Gros, T. M. Rice, and H. Shiba, Supercond. Sci. Technol. **1**, 36 (1988).
- [21] D. Qian, L. Wray, D. Hsieh, L. Viciu, R. J. Cava, J. L. Luo, D. Wu, N. L. Wang, and M. Z. Hasan, Phys. Rev. Lett. **97** 186405 (2006).
- [22] F.C. Chou, et. al., Phys. Rev. Lett. **92**, 157004 (2004).

CHAPTER 3

Stoner Magnetism

In the previous chapter, strong correlation plays an important role in the electronic structure of the cobaltates and has resolved the discrepancy between observation from ARPES experiment [1, 2] and theoretical LDA calculation [3]. Comparing to ARPES experimental results, the LDA Fermi surface has six extra small pockets instead of a central one in ARPES, and has a much wider bandwidth than ARPES. Strong correlation has introduced significant bandwidth renormalization of t_{2g} complex and the topology shows the disappearance of 6 small pockets.

In this chapter, the magnetic property of the cobaltates is investigated. It has been shown recently [7, 4, 5, 6] that correlation-induced corrections to the crystal field splitting and bandwidths of the LDA calculations [3] can produce a single renormalized band of mostly a_{1g} character at the Fermi level as observed by ARPES [1, 2, 8, 9]. Here we show that the description of the magnetism in the cobaltates, too, requires a proper account of the large Coulomb repulsion U at the cobaltate sites. Indeed, in the LSDA+ U theory [10], which accounts for the correlation effects in the Hartree-Fock approach, the LDA paramagnetic (PM) state is always unstable and the ground state is a fully polarized ferromagnet at all doping for U as small as 2eV. This disagrees with experiments that ferromagnetic order emerges only at large doping $x > 0.75$ and a spin degenerate Fermi surface is observed by ARPES at $x < 0.72$ [1]. The focus of this chapter is how strong

correlation helps stabilizing paramagnetic states in low dopings and before the investigation of strong correlation, results of weak coupling Hartree-Fock approximation is also presented.

3.1. Single band model for sodium cobaltates: a minimal model

It has been shown recently [5, 6, 7, 4] that correlation-induced corrections to the crystal field splitting and bandwidths of the LDA calculations [3] can produce a single renormalized band of mostly a_{1g} character at the Fermi level as observed by ARPES [1, 2, 8, 9].

According to the 3d transition metal oxides structure of Na_xCoO_2 , Co ions occupy the 3 lower orbitals of $3d^5$, t_{2g} complex. The trigonal distortion further splits t_{2g} into an a_{1g} and 2 degenerate e'_g bands. As shown in the previous chapter, in the case of paramagnetic LDA band structure in the strong U limit, bandwidth is renormalized. e'_g is suppressed and only a_{1g} band crosses the Fermi level [4]. This result is consistent with experiments [1, 2, 8, 9, 11]. A single band of mostly a_{1g} character lies near the Fermi level. The basic physics properties in low energy range can be represented by an effective minimal single-band model, provided that the strong Coulomb repulsion is included at the Co sites. The Hubbard model for the relevant low-energy quasiparticle band of approximate a_{1g} character is written as,

$$\begin{aligned}
 (3.1) \quad H &= H_0 + H_I \\
 &= \sum_{i,\sigma} t_{ij} a_{i\sigma}^\dagger a_{i\sigma} + \sum_{i,\sigma} U \hat{n}_{i\uparrow} \hat{n}_{i\downarrow}
 \end{aligned}$$

H_0 is the tight-binding description of the LDA a_{1g} band, and H_I describes the Hubbard physics on Co sites. $a_{i\sigma}^\dagger$ and $a_{i\sigma}$ are creation and annihilation operators of electrons on a_{1g} orbital, respectively, with spin σ . \hat{n}_i is the density operator. U is intra-orbital Coulomb repulsion. t_{ij} are the intra-orbital hopping integrals.

Therefore, before going into the realistic case of $3d$ bands of Na_xCoO_2 , we first investigate the effect of Hubbard U on a the single a_{1g} band on a triangular lattice. In order to restore the basic a_{1g} band shape, up to the 3^{rd} nearest neighbor hopping has to be taken into account.

H_0 can be written in k-space as

$$(3.2) \quad H_0 = \sum_{k,\sigma} K(k) a_{k\sigma}^+ a_{k\sigma}$$

$K(k)$ is the hopping element of a single a_{1g} band, defined on a triangular lattice, up to 3^{rd} *n.n.* hopping. From the symmetry of a_{1g} band, the hopping is isotropic, *i.e.*, the hopping integral is orientation independent.

$$(3.3) \quad \begin{aligned} K(k) &= 2t_1[\cos(k_1) + \cos(k_2) + \cos(k_3)] \\ &\quad + 2t_2[\cos(k_1 - k_2) + \cos(k_2 - k_3) + \cos(k_3 - k_1)] \\ &\quad + 2t_3[\cos(2k_1) + \cos(2k_2) + \cos(2k_3)] \\ &= -2t_1(\cos k_y + 2\cos\frac{\sqrt{3}k_x}{2}\cos\frac{k_y}{2}) \\ &\quad - 2t_2(\cos\sqrt{3}k_x + 2\cos\frac{\sqrt{3}k_x}{2}\cos\frac{3k_y}{2}) \\ &\quad - 2t_3(\cos 2k_y + 2\cos\sqrt{3}k_x\cos k_y) \end{aligned}$$

The hopping integrals obtained from the fit to LDA are $(t_1, t_2, t_3) = (-0.202, 0.035, 0.29)eV$ [4]. The hole density $n_i = n_{i\uparrow} + n_{i\downarrow} = 1 - x_i$ with x_i as the electron doping is fixed by the chemical potential μ . Due to the small direct Co-Co overlap and the 90° O-Co-O bond angle, the AF superexchange J in the cobaltates is small [12], consistent with the value $J \sim 5\text{meV}$ determined by inelastic neutron scattering [13]. We thus focus on the in-plane magnetism of the kinetic origin and ignore the small interlayer exchange coupling that only enables the 3D magnetic order at finite temperatures.

3.2. Stoner Magnetism

We start with a single band model on triangular lattice with the Hartree-Fock (HF) approximation. Applying HF approximation to the a_{1g} Hubbard model in Eq. (3.2), and decoupling H_I in the density channel, H is written as

$$(3.4) \quad \begin{aligned} H = & \sum_{i,\sigma} t_{ij} a_{i\sigma}^\dagger a_{i\sigma} + \sum_i U (n_{i\uparrow} a_{i\downarrow}^\dagger a_{i\downarrow} + n_{i\downarrow} a_{i\uparrow}^\dagger a_{i\uparrow}) \\ & - \sum_i n_{i\uparrow} n_{i\downarrow} \end{aligned}$$

$n_{i\sigma}$ is the local charge density and we propose a uniform charge density situation $n_{i\sigma} = n_\sigma$. Density difference between spin up and spin down is defined as magnetization satisfying,

$$(3.5) \quad \begin{aligned} M &= n_\uparrow - n_\downarrow \\ n_\sigma &= \frac{1}{N} \sum_i \langle a_{k\sigma}^\dagger a_{k\sigma} \rangle \end{aligned}$$

Fourier transform Hamiltonian in Eq. (3.4) into k-space,

$$(3.6) \quad H = \sum_{k,\sigma} K(k) a_{k\sigma}^\dagger a_{k\sigma} + \frac{1}{2} U \sum_{k,\sigma} n_{\bar{\sigma}} a_{k\sigma}^\dagger a_{k\sigma} - \frac{1}{2} U \sum_k M (a_{k\uparrow}^\dagger a_{k\uparrow} - a_{k\downarrow}^\dagger a_{k\downarrow})$$

Magnetization M is calculated through the self-consistent approach. On-site coulomb repulsion U is a variable parameter in Hamiltonian and is investigated at different values. Corresponding to each U , there is a critical x_c at which the system transits from a paramagnetic state (*i.e.* $m = 0$) into a ferromagnetic state (*i.e.* $m \neq 0$). This dependence relation is plotted in Fig. 3.1. From the figure, it shows that the greater U is, the lower x_c is, which means a small U will stabilize paramagnetic states. When U is greater than 2 eV, the entire electron doping range will be ferromagnetic.

The mechanism of transition here can be well understood from the Stoner theory, shown as follows.

$$(3.7) \quad \begin{aligned} M &= n_\uparrow - n_\downarrow \\ &= \int_0^\infty \frac{1}{2} (f^0(\epsilon_{k\uparrow}) - f^0(\epsilon_{k\downarrow})) N(\epsilon) d\epsilon \end{aligned}$$

$\epsilon_{k\sigma}$ is the energy of each spin under a small external field H . Without the perturbation H , the system is paramagnetic and has an energy $\epsilon(k)$ and a density of states $N(\epsilon)$

$$(3.8) \quad \begin{aligned} \epsilon_{k\uparrow} &= \epsilon(k) - H + U n_\downarrow \\ \epsilon_{k\downarrow} &= \epsilon(k) + H + U n_\downarrow \end{aligned}$$

In the limit of $H \rightarrow 0$, $T \rightarrow 0$,

$$(3.9) \quad M = \frac{HN(\epsilon_f)}{1 - \frac{1}{2}UN(\epsilon_f)}$$

From which, susceptibility is derived as

$$(3.10) \quad \chi = \frac{\partial M}{\partial H} = \frac{N(\epsilon_f)}{1 - \frac{1}{2}UN(\epsilon_f)}$$

The susceptibility of the system will diverge when $\frac{1}{2}UN(\epsilon_f) = 1$. The paramagnetic state becomes unstable, thus to induce a permanent magnetic moment. In the one band HFA case, when $U > U_c$, *e.g.* 2 eV, the entire doping range becomes unstable in paramagnetic states.

Whereas, in the large U region, HFA becomes unreliable, it will be more reasonable to substitute U in the infinite limit for finite U in HFA. In the weak-coupling HF theory, itinerant FM is due to the Stoner instability, i.e. the divergence of the uniform susceptibility $\chi = \chi_0/(1 - UN_F/2)$, where χ_0 is the free-electron value and N_F is the DOS at the Fermi level. The large DOS of the cobaltates would lead to FM order for all x for U greater than a value less than 2 eV [10], clearly inconsistent with experiments. The in-plane FM order does not emerge until $x > 0.75$ and that a single spin-degenerate Fermi surface of the Luttinger area is observed by ARPES for $x < 0.72$ [1]. We show that the weak-coupling Stoner instability is unphysical when correlation is strong.

3.3. Single band in the strong coupling limit

The failure of the HF or LSDA+ U theory lies in the spin-dependent self-energy correction that scales with U . This is unphysical for U larger than the bandwidth. For example,

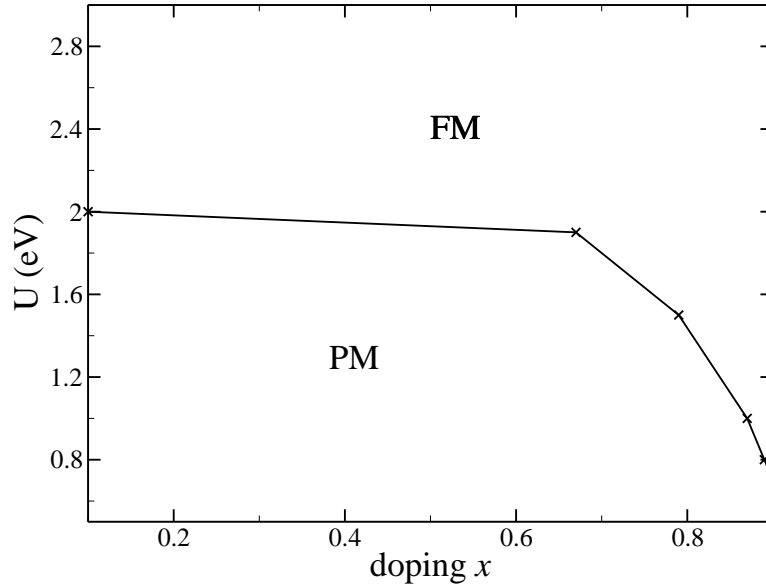


Figure 3.1. The division line represents x_c and separates ferromagnetic state (FM) and paramagnetic state (PM), corresponding to varying U

for large U , the system can simply avoid paying the energy penalty for double occupation in Eq. (3.2) by reverting to a fully spin-polarized state that involves only the kinetic energy. This is the physics behind the Nagaoka theorem: on square lattices, the ground state of the infinite- U Hubbard model doped with a single hole is a fully polarized FM. At finite hole density, the Nagaoka state is lower in energy than the Gutzwiller projected PM state at low doping [14]. Interestingly, on the triangular lattice the kinetic energy is frustrated in the sense that hopping around an elemental triangle picks up a negative sign, the Nagaoka state is not the ground state for a single hole [15]. To study FM at finite electron doping, we consider the large- U limit captured by the projection of double occupation. To make analytical progress, we treat the latter by Gutzwiller approximation (GA) in the grand canonical ensemble where the projected wave function can be written

as

$$(3.11) \quad |\Psi\rangle = \prod_i y_{i\uparrow}^{\hat{n}_{i\uparrow}} y_{i\downarrow}^{\hat{n}_{i\downarrow}} (1 - \hat{n}_{i\uparrow} \hat{n}_{i\downarrow}) |\Psi_0\rangle.$$

Here Ψ_0 is an unprojected Slater determinant state and $y_{i\sigma}$ is a spin-dependent local fugacity that maintains the equilibrium and the local densities upon projection. The GA is then equivalent to minimizing the energy of the renormalized Hamiltonian,

$$(3.12) \quad H_{GA} = \sum_{i,j,\sigma} g_{ij}^\sigma c_{i\sigma}^\dagger c_{j\sigma} + \sum_{i,\sigma} \varepsilon_{i\sigma} (c_{i\sigma}^\dagger c_{i\sigma} - n_{i\sigma}),$$

where the Gutzwiller renormalization factor,

$$(3.13) \quad g_{ij}^\sigma = \langle \Psi | c_{i\sigma}^\dagger c_{j\sigma} | \Psi \rangle \langle \Psi_0 | c_{i\sigma}^\dagger c_{j\sigma} | \Psi_0 \rangle \simeq \sqrt{\frac{x_i x_j}{(1 - n_{i\sigma})(1 - n_{j\sigma})}},$$

and $\varepsilon_{i\sigma}$ is determined by $\partial \langle H_{GA} \rangle / \partial n_{i\sigma} = 0$,

$$(3.14) \quad \varepsilon_{i\sigma} = \frac{1}{2(1 - n_{i\sigma})} \sum_j g_{ij}^\sigma t_{ij} \langle c_{i\sigma}^\dagger c_{j\sigma} + h.c. \rangle - \varepsilon_{i0}.$$

Physically, $\varepsilon_{i\sigma}$ is the local kinetic energy per doped spin- σ electron measured relative to the average over both spins,

$$(3.15) \quad \varepsilon_{i0} = - \sum_\sigma (1 - n_{i\sigma}) \varepsilon_{i\sigma}$$

In the uniform phase,

$$(3.16) \quad \begin{aligned} n_{i\sigma} &= n_\sigma \\ g_{ij}^\sigma &= g^\sigma \\ \varepsilon_{i\sigma} &= \varepsilon_\sigma \end{aligned}$$

$$(3.17) \quad \varepsilon_\sigma = \frac{1}{(1 - n_\sigma)} \sum_k E_{k\sigma} f(E_{k\sigma} + \varepsilon_\sigma - \mu) - \varepsilon_0,$$

In our single, uniform magnetic band case, Gutzwiller factor is express in terms of density and spins.

$$(3.18) \quad g_\sigma = \frac{x}{1 - n_\sigma}$$

In strong coupling limit, $U \rightarrow \infty$, Gutzwiller projection is applied here to project out double occupation on a single site. The general form of Gutzwiller factor for multiple bands is written as

$$(3.19) \quad g^{\alpha\beta} = \frac{x}{\sqrt{(1 - n_{i\alpha\sigma})(1 - n_{j\beta\sigma})}}$$

In the strong coupling cases, the occupation number n_σ of each spin of a_{1g} is restricted by Lagrangian multiplier ε_σ to obey $n_\sigma = \frac{1}{N} \sum_k \langle a_{k\sigma}^\dagger a_{k\sigma} \rangle$. Therefore, the Hamiltonian of a single band Hubbard Model with infinite U is written as

$$(3.20) \quad H = \sum_{k,\sigma} g_\sigma K(k) a_{k\sigma}^\dagger a_{k\sigma} + \sum_{k,\sigma} \varepsilon_\sigma (a_{k\sigma}^\dagger a_{k\sigma} - n_\sigma)$$

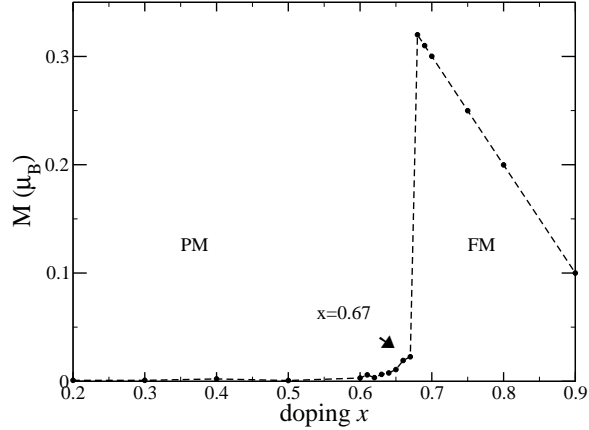


Figure 3.2. Phase diagram of a_{1g} band, $x_c = 0.67$

To minimize the ground state energy, we express ε_σ in self-consistent calculation, as

$$(3.21) \quad \varepsilon_\sigma = \frac{1}{N} \sum_k \frac{x}{(1 - n_\sigma)^2} K(k) \langle a_{k\sigma}^\dagger a_{k\sigma} \rangle$$

The kinetic part $K(k)$ with 3^{rd} *n.n.* hopping has been shown in Eq. (3.4).

Magnetization M is calculated and phase diagram is plotted in Fig. 3.2. It shows that a magnetic phase transition happens around $x_c = 0.67$. At small x , paramagnetic state is stabilized and at $x > 0.67$, the system is fully polarized and satisfies the linear relation $M = 1 - x$.

The mechanism of this phase transition is further explored in the following literature as 2 parts.

The first explanation of the phase transition is inspired by that of HFA. Since $UN(\epsilon_f)$ plays an important role in HFA and here U is set $\rightarrow \infty$. The importance of $N(\epsilon)$ in the magnetic phase transition will be demonstrated by the comparison between the 1^{st} *n.n.* and 3^{rd} *n.n.* hopping integrated in the single a_{1g} band.

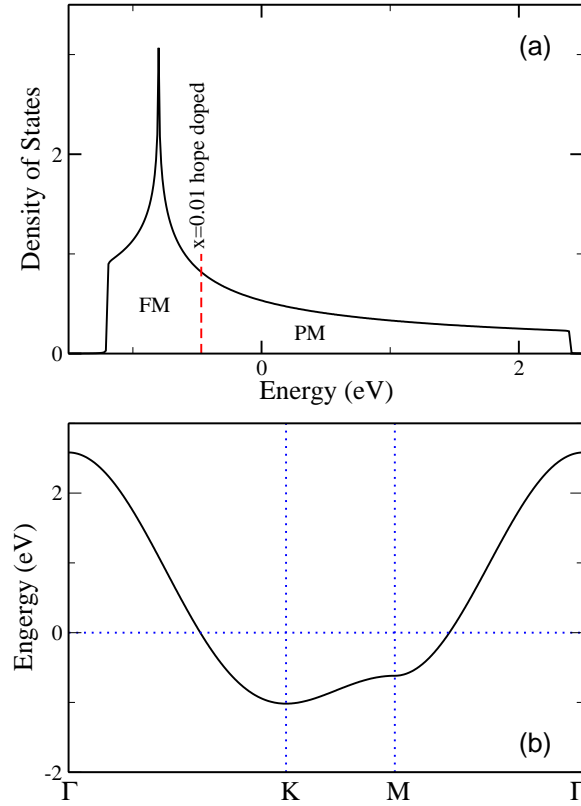


Figure 3.3. a) The density of states of a single 1st n.n. hopping band, on the electron doped side, paramagnetic (PM) and on the hole doped side, ferromagnetic (FM). b) Band structure at $x = 0.1$, electron doped.

For a single band with the 1st n.n. hopping on a triangular lattice, the hopping is

$$(3.22) \quad K(k) = -2t(\cos k_1 + \cos k_2 + \cos k_3)$$

With $t < 0$, the band structure and the corresponding density of states in the Eq. (3.22) are plotted in Fig. 3.3.

The entire e⁻ doped range is paramagnetic, while almost the entire hole doped range is ferromagnetic. Comparing the DOS and band dispersion plots between 1st n.n. hopping in Fig. 3.3 and 3rd n.n. in Fig. 3.4. In 3rd n.n., there is an extra peak above the fermi

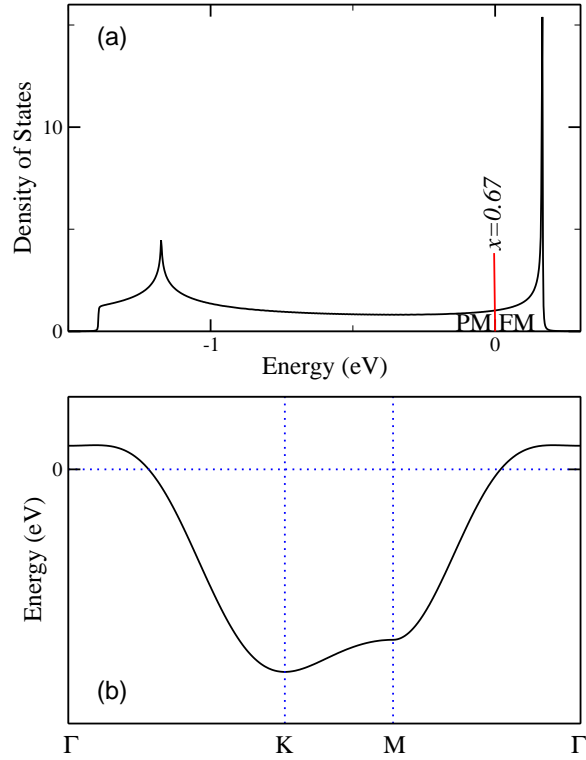


Figure 3.4. a)The density of states of a_{1g} band up to 3^{rd} *n.n.* hopping, on the electron doped side, paramagnetic (PM) and ferromagnetic (FM) are separated at $x_c = 0.67$. b)Band structure is at $x = 0.67$, electron doped.

level. This can be explained by the corresponding flat top of band dispersion at Γ point. Comparing to band dispersion in Fig. 3.3, the velocity here at Γ is greatly enhanced, thus push DOS up. If we recall the Stoner instability in Eq. (3.10), the high DOS provides the possibility of divergence of susceptibility. The density of states of the 1^{st} *n.n.* hopping has only the long right tail in the electron doped range, which is not enough to induce a diverging susceptibility as the extra peak in the 3^{rd} *n.n.* does.

Although DOS plays an important role in the strong coupling limit as shown above, comparing the paramagnetic DOS between 2 sides of x_c , $x = 0.5$ and $x = 0.7$ in Fig. 3.5, there is no apparent difference between them at fermi level. This tells us that although the

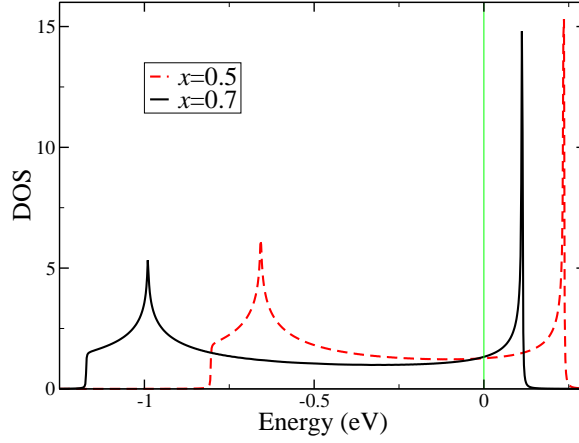


Figure 3.5. Paramagnetic DOS at $x = 0.5$ (dotted) and $x = 0.7$ (solid), with $U \rightarrow \infty$

peak of DOS above the fermi level enhance the probability of transition to ferromagnetic state in general, it is not the only determinant in the strong coupling phase transition. The reason is due to the Gutzwiller factor as in Eq. (3.19). The denominator is constrained to $0 \leq n_\sigma \leq 1 - x$, which makes the Gutzwiller factor always no more than 1 and has the effect of band narrowing. At lower dopings, the bandwidth shrinks much more than at higher dopings. This narrowing effect greatly squeezes DOS up at low dopings.

In order to understand the exact determinants of the magnetic phase transition in the strong U limit, we derived the analytical expression of susceptibility, following a similar route as Stoner theory. To derive a renormalized Stoner theory for the instability of the PM phase against uniform FM order, we calculate the uniform magnetic susceptibility

$$\chi = \partial M / \partial h$$

where

$$M = (n_\uparrow - n_\downarrow)\mu_B$$

is the magnetization due to an infinitesimal external magnetic field h . Including the leading h -dependence of ε_σ in Eq. (2.27) we can obtain the renormalized Stoner equation.

In the strong coupling limit, with Gutzwiller factor ε_σ ,

$$(3.23) \quad \begin{aligned} \epsilon_{k\uparrow} &= \frac{x}{1-n_\uparrow} K(k) + \varepsilon_\uparrow - H \\ \epsilon_{k\downarrow} &= \frac{x}{1-n_\downarrow} K(k) + \varepsilon_\downarrow + H \end{aligned}$$

In the limit of $H \rightarrow 0$, $T \rightarrow 0$,

$$(3.24) \quad \begin{aligned} M &= n_\uparrow - n_\downarrow \\ &= \int_0^\infty \frac{1}{2} (f^0(\epsilon_{k\uparrow}) - f^0(\epsilon_{k\downarrow})) N(\epsilon) d\epsilon \\ &= \int_0^\infty \frac{1}{2} \left[\left(-\frac{\partial f}{\partial \epsilon} \right) (2H - (\varepsilon_\uparrow - \varepsilon_\downarrow)) \right. \end{aligned}$$

$$(3.25) \quad \left. - \frac{K(k)x}{(1-\frac{1}{2}n)^2} (n_\uparrow - n_\downarrow) \right] d\epsilon$$

Plug in the expression of fugacity ε_σ in Eq. (3.21) and an analogy of Stoner susceptibility is derived as

$$(3.26) \quad \chi = \frac{\chi_0}{1-2KN_F}, \quad K = -\frac{2}{1+x} (E_{k_F} + \varepsilon + \varepsilon_0),$$

where N_F is the renormalized DOS and K measures the energy per electron at the Fermi level. The latter plays the role of the effective interaction strength, replacing the Hubbard- U in the Stoner susceptibility. $n = 1 - x$ is the number of holes per site; ε and $N(\epsilon_f)$ are paramagnetic fugacity and the density of states, respectively. These paramagnetic parameters are obtained self-consistently by enforcing $n_\uparrow = n_\downarrow$ in Eq. (3.20).

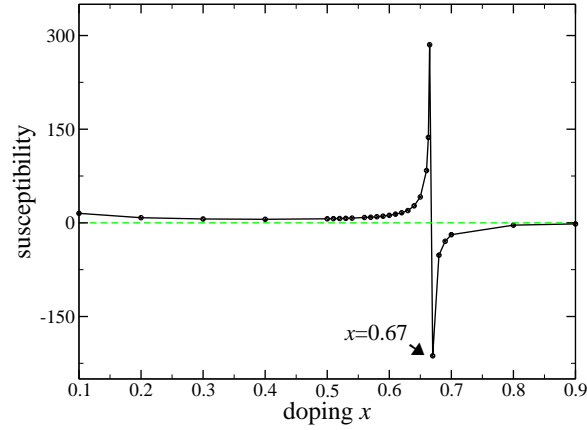


Figure 3.6. Susceptibility of single a_{1g} band with 3^{rd} *n.n.* hopping diverges at $x_c = 0.67$

Fig. 3.6 shows the doping dependence of χ which diverges at $x_c \simeq 0.67$, corresponding to the renormalized Stoner criterion $2KN_F = 1$, beyond which FM order develops at $T = 0$. The self-consistently determined magnetization shown in Fig. 3.2 indicates a sharp transition into the fully polarized FM, half-metallic state. Comparing to Stoner model, the strong coupling susceptibility has the same structure, but with a more complicated U_{eff} instead of Coulomb repulsion. Similarly, the critical doping is obtained when the value is diverging. Fig. 3.6 shows susceptibility as a function of x and the divergence happens around $x = 0.67$. This result consists with our numerical calculation previously shown in Fig. 3.4.

So far, the phase transition is first explained by an analytical expression of susceptibility as a function of DOS, fugacity, kinetic energy, and so on. Secondly, the consistency between numerical and analytical calculation can be verified by another approach, energy dispersion.

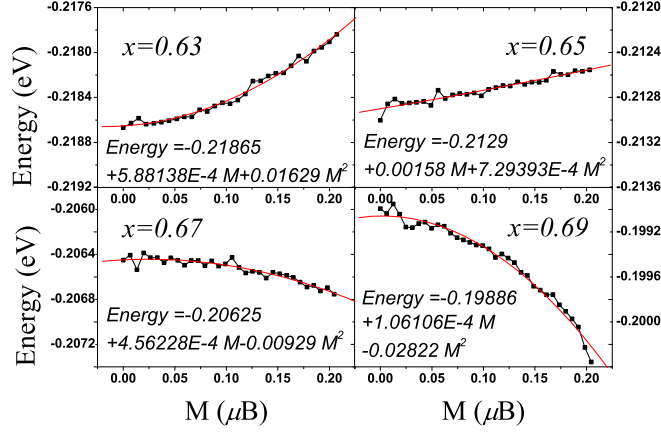


Figure 3.7. Dots are numerical calculation of ground state energy as a function of M . Solid lines are 2^{nd} order polynomial fit. Results are shown at $x = 0.63, 0.65, 0.67, 0.69$. $\chi^{-1} \propto a_2$

Since χ is defined as $\frac{\partial M}{\partial H}$ and free energy $F \propto MH$, the following expression is derived.

$$(3.27) \quad \chi^{-1} \propto \frac{\partial^2 F}{\partial M^2}$$

In numerical calculation, at each x , if we force the magnetization M to be a series of values less than fully polarized $M = 1 - x$, then the ground state energy can be plotted as a function of M , as shown in Fig. 3.7. Suppose $F = a_0 + a_1 M + a_2 M^2$ and apply a polynomial fit to the energy-magnetization curve up to the 2^{nd} order. According to the Eq. (3.27), $\chi^{-1} \propto a_2$. When a_2 is close to zero, χ approaches infinite, which should correspond to a magnetic phase transition. From Fig. 3.7, $x = 0.63$ and $x = 0.65$ both have a positive a_2 . When x steps across 0.67, a_2 goes $0^+ \rightarrow 0^-$, which qualitatively shows a transition around $x = 0.67$.

Hitherto, the presence of the DOS peak near the band top is important for the emergence of the in-plane FM order. For example, with only the nearest neighbor hopping, the

FM order is completely suppressed by strong correlation [16]. Using a strong-coupling Gutzwiller projection approach, we show that the Stoner criterion is strongly renormalized and the spin dependent self-energy scales with the average kinetic energy instead of U . The PM phase is in fact stable against itinerant FM below the critical electron doping $x_c \simeq 0.67$ above which in-plane FM order emerges. We have showed that in the strong coupling limit, the magnetic phase transition is happened at $x = 0.67$ and explained the mechanism of it from 2 different aspects, analytical and energy fitting. All of them have presented a consistent result. This success in explaining the magnetic phase transition in a_{1g} case intrigues us to apply the same approach to the realistic cobaltate bands.

3.4. Magnetism in Na_xCoO_2

The previous results can be extended to the realistic three-band Hubbard model of the t_{2g} complex. The Hamiltonian is written as,

$$(3.28) \quad H = H_0 + H_I$$

$$(3.29) \quad H_0 = \sum_{i,\sigma,\alpha,\beta} K_{\alpha\beta}^a(k) a_{i\alpha\sigma}^+ a_{i\beta\sigma} + \sum_{i,\sigma,\alpha} \Delta_\alpha a_{i\alpha\sigma}^+ a_{i\alpha\sigma}$$

$$(3.30) \quad H_I = U \sum_{i,\alpha} n_{i\alpha\uparrow} n_{i\alpha\downarrow} + (U' - \frac{1}{2}J) \sum_{i,\alpha\beta} n_{i\alpha} n_{i\beta} \\ - J \sum_{i,\alpha>\beta} S_{i\alpha} \cdot S_{i\beta} + J \sum_{i,\alpha\neq\beta} \alpha_{i\alpha\uparrow}^+ \alpha_{i\alpha\downarrow}^+ a_{i\beta\downarrow} a_{i\beta\uparrow}$$

U is the intra-orbital Coulomb repulsion. U' is the inter-orbital Coulomb repulsion. As discussed in the previous chapter, J is Hund's rule coupling and $J = \frac{1}{2}(U - U')$.

Similar to the single band model, we first exam the behavior of 3-band model in the Hartree-Fock Approximation. Taking the spins into account,

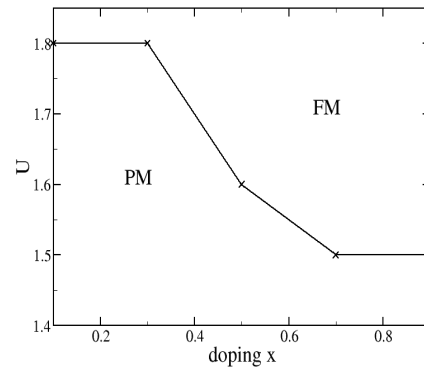
$$\begin{aligned}
(3.31) \quad H_I &= \sum_{k,\sigma,\alpha} (2Un_\alpha + 2 \sum_{\beta \neq \alpha} U' n_\beta) a_{k\alpha\sigma}^+ a_{k\alpha\sigma} \\
&+ \sum_{k,\sigma,\alpha \neq \beta} (Jn_{\bar{\sigma},\alpha\beta} + Jn_{\bar{\sigma},\alpha\beta}^* + (J - U')n_{\sigma,\alpha\beta}^*) a_{k\alpha\sigma}^+ a_{k\alpha\sigma} \\
&- \sum_{k,\alpha} Um_\alpha (a_{k\alpha\uparrow}^+ a_{k\alpha\uparrow} - a_{k\alpha\downarrow}^+ a_{k\alpha\downarrow})
\end{aligned}$$

$$(3.32) \quad m_\alpha = \langle a_{k\alpha\uparrow}^+ a_{k\alpha\uparrow} - a_{k\alpha\downarrow}^+ a_{k\alpha\downarrow} \rangle$$

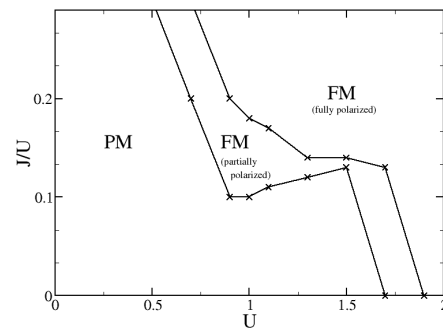
m_α is equivalent to the moment measure in single band calculation. To simplify the effect of parameters, U' takes the same value of U , which makes $J = 0$. Through self-consistency calculation, a phase diagram at different doping level x has been shown in Fig. 3.8(a). In the single band result, as long as U is greater than 2 eV, the system turns in to FM throughout all the dopings. Similar to that result, there is a separation between FM and PM at different values for different dopings. Although the larger the doping, the less U is required to turn into FM, above 1.8 eV the 3-band model stays FM at all dopings. Then we turn to exam the effects of both U and J at $x=0.5$, shown in Fig. 3.8(b). Although there exist a partially polarized state, when U is greater than a certain value it will transit into FM. Consistent with the behavior of 1 band model, but not consistent with experimental observation [1].

As the conclusion made in the previous section, in Hartree-Fock approximation, magnetization is due to Stoner instability. The spin-dependent self-energy correction that scales with U . The system can avoid paying the energy penalty for double occupation by spin-polarization which only involves the kinetic energy. This is unphysical for U larger

a)



b)



c)

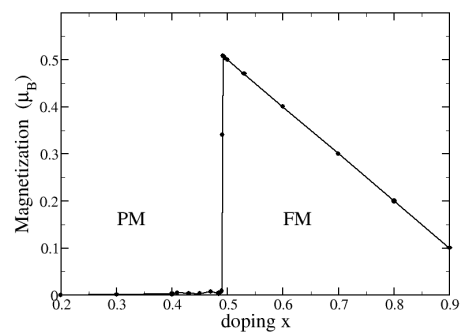


Figure 3.8. Phase diagram of the 3-band model. a) phase diagram of a multi-band Hubbard model for Na_xCoO_2 as a function of U in Hartree-Fock approximation. b) The interplay of J and U at $x=0.5$ in HFA. c) In strong U limit, phase diagram at different doping levels.

than the bandwidth. Then we investigate the magnetic behavior in strong-correlation limit, setting U and U' to infinity, and $J \rightarrow 0$.

$$(3.33) \quad H = \sum_{k,\sigma,\alpha,\beta} g_{t\sigma}^{\alpha\beta}(k) a_{k\alpha\sigma}^+ a_{k\beta\sigma} + \sum_{k,\sigma,\alpha} \Delta_\alpha a_{k\alpha\sigma}^+ a_{k\alpha\sigma} + \sum_{\alpha,\sigma} \epsilon_{\alpha\sigma} (a_{k\alpha\sigma}^+ a_{k\alpha\sigma} - n_{\alpha\sigma})$$

where $\epsilon_{\alpha\sigma}$ is the multi-band fugacity. $g_{t\sigma}^{\alpha\beta}$ is the multi-band Gutzwiller factor used to project out double occupation. α and β indicates the three t_{2g} band. In a density uniform case, it is written as

$$g_{t\sigma}^{\alpha\beta} = \frac{x}{\sqrt{(1 - n_{\alpha\sigma})(1 - n_{\beta\sigma})}}$$

The phase diagram for the multi-band is presented in Fig. 3.8(c). It shows at low doping x , the large U stabilizes the ground state at paramagnetic phase. At high doping x , the system transits into a ferromagnetic state.

The results in this section from the three-band Hubbard model of the t_{2g} complex are consistent with our previous one band model and experiments qualitatively. The finding of the fully polarized FM state at large x is consistent with the large FM moment of about $0.13\mu_B$ per Co site at $x = 0.82$ observed by neutron scattering [13] comparing to $0.18\mu_B$ for a fully polarized FM state.

References

- [1] H.B. Yang et al., Phys. Rev. Lett. **95**, 146401 (2005).
- [2] H.B. Yang et al., Phys. Rev. Lett. **92**, 246403 (2004).
- [3] D.J. Singh, Phys. Rev. **B61**, 13397 (2000).
- [4] S. Zhou, M. Gao, H. Ding, P. A. Lee, and Z. Wang, Phys. Rev. Lett. **94**, 206401 (2005)
- [5] H. Ishida, M.D. Johannes, and A. Liebsch, Phys. Rev. Lett. **94**, 196401 (2005).
- [6] C.A. Marianetti, K. Haule, O. Parcollet, Phys. Rev. Lett. **99**, 246404 (2007).
- [7] A. Bourgeois, A.A. Aligia, T. Kroll, M.D. Nunez-Regueiro, PRB **75**, 174518 (2007).
- [8] M. Z. Hasan, et. al., Phys. Rev. Lett. **92**, 246402 (2004).
- [9] D. Qian, L. Wray, D. Hsieh, L. Viciu, R. J. Cava, J. L. Luo, D. Wu, N. L. Wang, and M. Z. Hasan, Phys. Rev. Lett. **97** 186405 (2006)
- [10] P. Zhang, et. al., Phys. Rev. Lett. **93**, 236402 (2004).
- [11] T. Shimojima, K.Ishizaka, S. Tsuda, T. Kiss, T. Yokoya, A. Chainani, S. Shin, P. Badica, K. Yamada, and K. Togano, Phys. Rev. Lett. **97**, 267003 (2006)
- [12] O.I. Motrunich and P.A. Lee, Phys. Rev. **B69**, 214516 (2004).
- [13] S.P.Bayrakci et al., Phys. Rev. Lett. **94**, 157205 (2005).
- [14] G. Kotliar and A.E. Ruckenstein, Phys. Rev. Lett. **57**, 1362 (1986).
- [15] J.O. Haerter and B.S. Shastry, Phys. Rev. Lett. **95**, 087202 (2005).
- [16] J. Merino, et. al., Phys. Rev. **B73**, 235107 (2006).

CHAPTER 4

Itinerant and Localized Magnetism in Sodium Rich Phases of Na_xCoO_2

We study the interplay between correlation, itinerant ferromagnetism and local moment formation on the electron doped triangular lattice of sodium cobaltates Na_xCoO_2 . We find the enhanced Na dopant potential fluctuations play a crucial role in the sodium rich phases and lead to an inhomogeneous FM state, exhibiting nonmagnetic Co^{3+} patches, antiferromagnetic (AF) correlated regions, and FM clusters with AF domains. Hole doping the band insulator at $x=1$ leads to the formation of local moments near the Na vacancies and AF correlated magnetic clusters. We discuss these results in connections to recent neutron, μSR , and NMR experiments.

4.1. Recent focus on magnetism in sodium rich phases

Since the discovery of unconventional superconductivity near $x = 0.3$ upon water-intercalation in this material [1], a broad spectrum of experiments have been performed, yielding a rich and complex phase diagram with many unexpected and novel properties. Magnetism plays an essential role in the sodium rich region with $x > 0.5$.

The metallic transport coexists with a Curie-Weiss magnetic susceptibility leading to a novel “Curie-Weiss metal” [2]. Neutron scattering and NMR experiments find strong in-plane ferromagnetic (FM) fluctuations at high temperatures and magnetically ordered

states emerge for $x > 0.75$ [3]. At $x = 0.82$, neutron scattering determined that in-plane FM order and inter-layer antiferromagnetic (AF) order develops below a 3D Neel temperature $T_N = 20\text{K}$ [4]. They have also extracted the magnetization value on each Co to be $0.13 \pm 0.02\mu_B$.

There is increasing experimental evidence for unexpected strong correlation effects as the cobaltates approach the band insulating limit at $x = 1$. μSR experiment [5] (2007) has investigated the magnetic properties of $\text{Na}_{a_x}\text{CoO}_2$ with x between 0.78 and 0.97. Their data suggests a nanoscopic coexistence of the magnetic and the non-magnetic regions. They discover the emergence of AF correlated magnetic clusters and localized magnetic moments for $x > 0.96$. They propose the magnetic clusters are Na vacancy induced and remains isolated for x above 0.96. Below 0.96, the clusters percolate until a homogeneous magnetic state is achieved near $x = 0.75$. This magnetic state is long-range ordered and exhibits strong frustration. In Fig. 4.1, it shows at all investigated dopings, $x = 0.78, 0.87, 0.92$, the 5 K ZF- μSR time spectra contains an oscillatory component and it means magnetism exists in part of the volume.

Interestingly, the high thermoelectric power of the sodium cobaltate is found in the sodium rich region which is likely to have a related magnetic origin [6]. The nature of the magnetism in the sodium rich region has been the focus of several theoretical work [7, 8, 9, 10]. For example, Daghofer *et al* propose a spin-orbital-polaron model [10], shown in Fig. 4.1(d), and explain how polarons account for the peculiar magnetic properties at small hole concentration when $x > 0.7$. Polaron consists one Co^{4+} with $s=1/2$ in the center and six adjacent Co^{3+} with $S=1$. When polarons evolves into clusters, different parameters could drive two adjacent polarons into different magnetic orders. However it

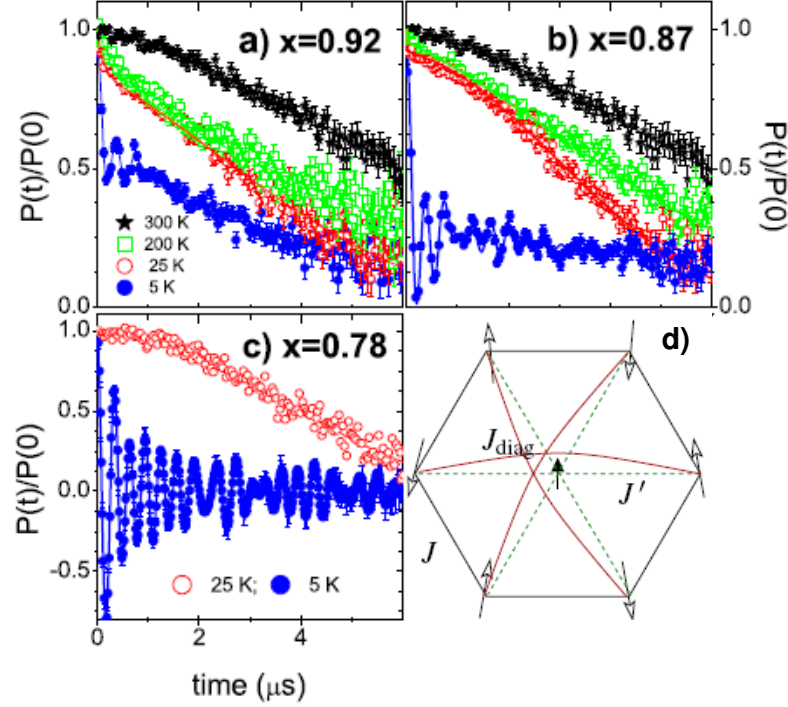


Figure 4.1. a)-c) Zero-field μSR spectra for Na_xCoO_2 crystals with $x=0.92$, 0.87 and 0.78 which exhibit a rapidly increasing fraction of the oscillatory signal at 5 K. d) Polaron model[10]: Co^{4+} with $s=1/2$ in the center, induced spin $S=1$ on the six adjacent Co^{3+} sites. J , J_{diag} , and J' are parameters for nearest neighbour coupling on the ring, cross diagonal coupling and center to the ring coupling, respectively.

needs $\text{Co}^{3+}/\text{Co}^{4+}$ charge order, thus inconsistent with our result and the current data from μSR is insufficient to establish such a scenario [5].

It has been shown in the previous chapter that through a strong-coupling Gutzwiller projection approach, the Stoner criterion is strongly renormalized and the spin dependent self-energy scales with the average kinetic energy instead of U . The PM phase is in fact

stable against itinerant FM below a critical electron doping $x_c \simeq 0.67$, above which in-plane FM order emerges. In this paper, we study the magnetic properties, both itinerant and localized, of strongly correlated electrons on the triangular lattice, and present a theoretical description of the novel magnetism observed by experiments in the sodium rich phases.

4.2. Sodium structure

The crystal structure of Na_xCoO_2 consists of alternating layers of sodiums and triangular CoO_2 layers which octahedrally coordinated by oxygen. The charge on the CoO_2 layers is controlled by the concentration of Sodium ions in the Na layer. Each sodium ion added to the Na layer attract one electron in the Cobalt layer.

There are two possible sodium locations and are defined as Na(1) and Na(2), shown in Fig. 4.2. If we project the location of Na ions onto the Cobalt plane, Na(1) reside right on the cobalt sites and Na(2) reside at the center of the cobalt triangular shaped lattice.

Huang *et al* has shown the crystal structures of Na_xCoO_2 for $0.34 < x \leq 1.0$ [11]. It's found that Na(1) are unambiguously defined for all dopings and Na(2) display a large temperature factor. A refinement with Na(2), labeled as the Na(2)' allows for displacements of the Na(2) atoms from the centers of the ideal triangular prismatic coordination polyhedra. 3 types of crystal structures are found across doping levels, shown schematically in Fig. 4.2. H1 phase refers to a state in which both Na(1) and Na(2)' sites are partially filled. H2 phase refers to that both Na(1) and Na(2) sites are partially filled. In H3 phase only Na(2) sites are filled. Over different doping ranges, the compound is described by one or two of the phases, shown in Fig. 4.3(a). From 0.34 to 0.74 with the

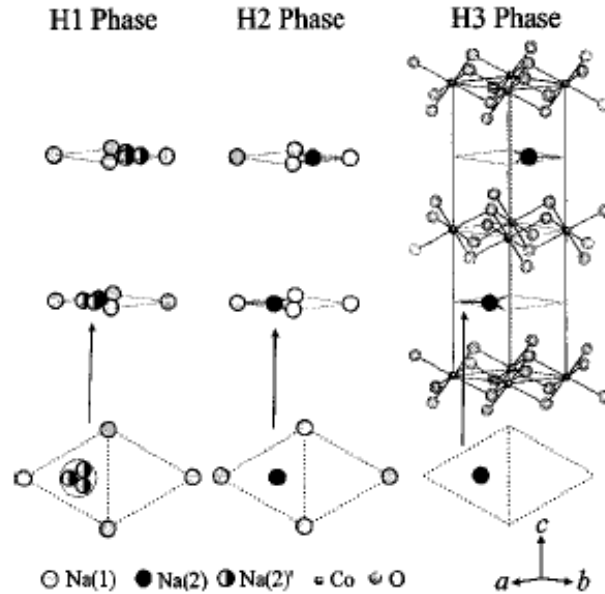


Figure 4.2. The three types of hexagonal structure in Na_xCoO_2 H1-H3. Layers of edge-shared CoO_6 octahedra are seen in a triangular lattice with Na ions occupying ordered or disordered positions in the interleaving planes. Three different Na ion sites are shown beneath.

exception of $x=0.5$, H1 phase describes the structure of its sodium content. Then a small two phase region H1+H2 ranges from 0.72 to 0.76. H2 phase is found for $0.76 < x < \sim 0.82$. From 0.82 to 0.97 is a mixture of H2+H3 phase. Above that, only Na2 sites are occupied, designated as H3 phase. Fig. 4.3(b) shows structure characteristics at different dopings. Even in the same sodium phase, the content ratio of Na(1) and Na(2) are different and the fraction occupancies of the two types of sodium sites are a strong function of total Na content.

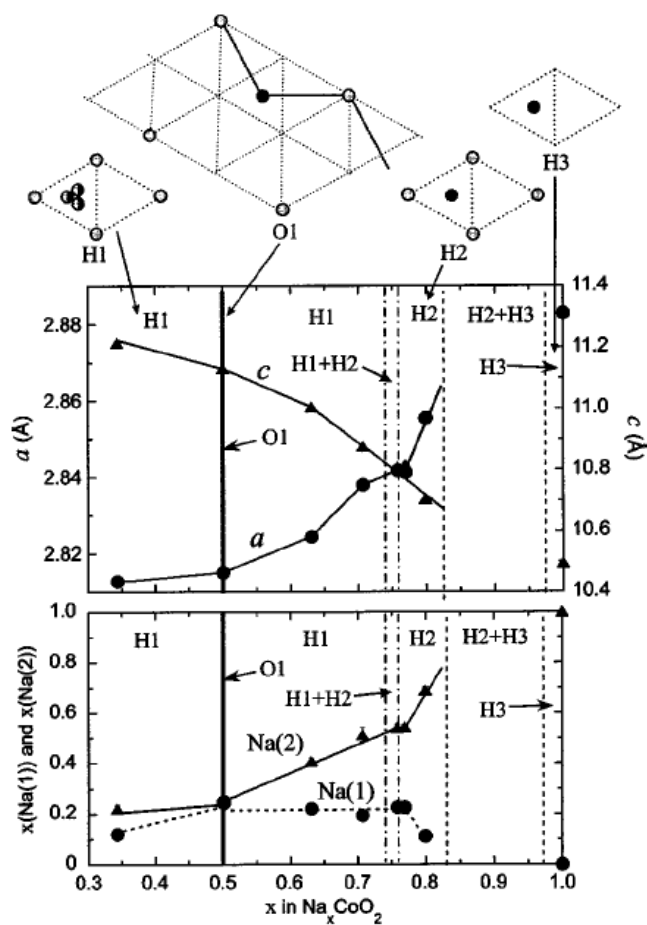


Figure 4.3. a) The general structural characteristics and compositional stability regions of the four Na_xCoO_2 phases, H1-H3, O1. Above the panel, the sodium ion distributions are shown schematically. b). Fractional occupancies of the two types of sodium sites.

NMR study by Mukhamedshin *et al* has shown the magnetic properties of Na_xCoO_2 in sodium rich region for $x > 0.65$ [12]. It shows the presence of Co^{3+} above doping $x = 0.65$. All the experimental results mentioned above lead to the question that if it is local moment formation or spin state transition?

In our study, we focus on the region with $x > 0.8$ and it relates to H2+H3 phase, where Na(2) and Na(3) are partially occupied according to the fractional occupation. In the sodium extreme rich region, we will only consider Na(2) sites. Na potential is taken into Hamiltonian through the following equation with long range Coulomb screening.

$$(4.1) \quad V(i) = V_d \sum_{I=1}^{N_{Na}} \frac{\hat{n}_i}{\sqrt{|\vec{r}_I - \vec{r}_i|^2 + d_z^2}}$$

V_d is the potential strength. d_z is the distance between Co and Na layers.

4.3. Itinerant and localized magnetism

In the sodium-rich region, we show that the enhanced electrostatic potential fluctuations due to the disordered Na dopants lead to the coexistence of localized and itinerant electronic states with inhomogeneous FM order, exhibiting nonmagnetic Co^{3+} patches, AF correlated local regions, and FM clusters with AF domain walls. For very high Na doping, the dilute Na vacancies enhance the strong correlation effects by increasing the localization tendency of the carriers [13]. We consider the case of a few holes (Na vacancies) doped into the band insulator at $x = 1$, and find that the hidden correlation effects are brought out upon the slightest amount of doping. Specifically, a single hole/Na vacancy induces an $S = 1/2$ local moment. We address the interactions between the local moments and the evolution into magnetic clusters and eventually to the macroscopic FM

ordered state with decreasing Na doping and provide a theoretical description of neutron [4], μ SR [5] and NMR experiments [12].

We start with the Hubbard model for the relevant low-energy quasiparticle band of approximate a_{1g} character,

$$(4.2) \quad H = \sum_{i,j,\sigma} t_{ij} c_{i\sigma}^\dagger c_{j\sigma} + \sum_i U \hat{n}_{i\uparrow} \hat{n}_{i\downarrow}$$

where $c_{i\sigma}^\dagger$ creates a *hole* and U ($\sim 5\text{eV}$ for the cobaltates [14]) is the on-site Coulomb repulsion. To model the a_{1g} band, we consider up to 3rd nearest-neighbor hopping $(t_1, t_2, t_3) = (-0.202, 0.035, 0.029)\text{eV}$ [15]. The hole density $n_i = n_{i\uparrow} + n_{i\downarrow} = 1 - x_i$ with x_i the electron doping, is fixed by the chemical potential μ . Due to the small direct Co-Co overlap and the large U and the 90° O-Co-O bond angle, the AF superexchange J in the cobaltates is small [16], consistent with the value $J \sim 5\text{meV}$ determined by inelastic neutron scattering [4]. We thus focus on the in-plane magnetism of the kinetic origin and ignore the small interlayer exchange coupling that only enables the 3D magnetic order at finite temperatures.

We solve the spatially unrestricted Hamiltonian in the strong correlated limit and study the effects of the Na dopants. It is known that Na orders at $x = 0.5$ into $\sqrt{3} \times 2$ superstructure [17], which has been shown [15] to play an important role in alleviating geometrical frustration for the emergence of the 2×2 AF ordered state observed by neutron scattering [18]. For $x \neq 0.5$, Na ions are disordered, and occupy randomly the preferred Na(1) and Na(2) sites directly above/below the Co or the middle of the Co triangle respectively, with a ratio of $1 : 7$ at $x = 0.8$ [17]. The electrostatic potential is

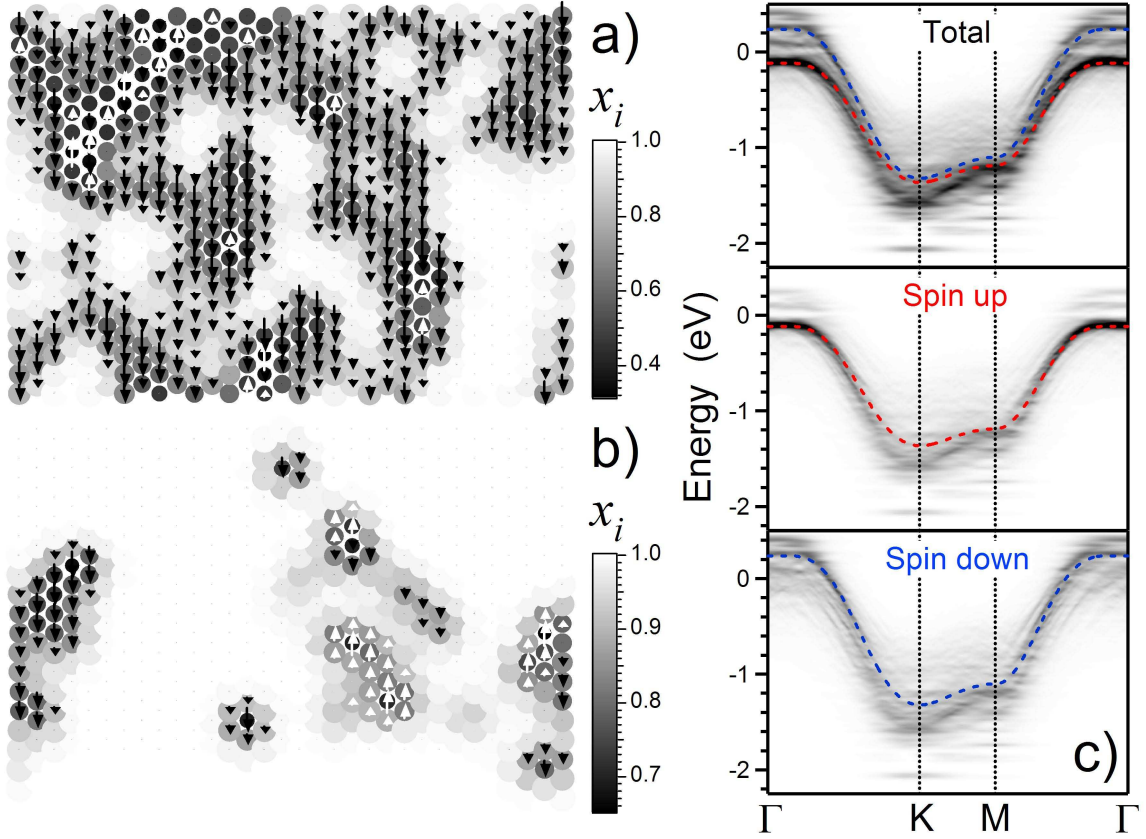


Figure 4.4. The spin (colored arrows) and charge (local doping x_i) distribution in a typical Na(1) and Na(2) realization at $x = 0.8$ (a) and $x = 0.97$. (c) The one-particle spectral intensity (top) and its spin resolved components at $x = 0.8$.

described by adding to the Hamiltonian (4.2),

$$(4.3) \quad H_V = V \sum_{i>j} \frac{\hat{n}_i \hat{n}_j}{|\vec{r}_i - \vec{r}_j|} + V_d \sum_i \sum_{\ell=1}^{N_{\text{Na}}} \frac{\hat{n}_i}{\sqrt{|\vec{r}_\ell - \vec{r}_i|^2 + d_z^2}},$$

where V_d is the dopant potential strength, $d_z \simeq a$ the setback distance of Na to the Co plane, and V the long-range Coulomb interaction that must be included to account for carrier screening. Figs. 4.4(a) and 4.4(b) show the typical charge and spin distribution of the inhomogeneous FM state at $x = 0.8$ and $x = 0.97$ on triangular lattices of 32×20 sites, with $V = 0.2\text{eV}$ and $V_d = 0.6\text{eV}$. Note that at such strength of (V, V_d) , the ordered Na at $x = 0.5$ only induces a weak charge modulation [15]. In contrast, the random distribution of Na at $x = 0.8$ leads to large fluctuations in the local electrostatic potential, causing the localization of the electrons and the formation of the nonmagnetic Co^{3+} clusters where $x_i \simeq 1$. This result is in line with NMR: the presence of Co^{3+} for $x > 0.65$ but not at $x = 0.5$ [12, 19]. The one-particle spectral intensity in Fig. 4.4(c) clearly demonstrates the coexistence of localized and itinerant band-like states. Interestingly, AF correlated regions emerge at $x = 0.8$ in locally underdoped regions in Fig. 4.4(a). In these regions, x is much smaller and the kinetic AF correlation imbedded in the Gutzwiller factor in Eq. (3) prevails due to the alleviated AF frustration by charge inhomogeneity, as proposed for the “0.5 phase” [15]. As a result, the average magnetic moment in Fig. 4.4(a) is reduced from the fully polarized value to about $0.13\mu_B$ per Co site, in qualitative agreement with the finding of neutron scattering [4]. For stronger potential fluctuations, FM clusters with AF domain walls emerge, as seen more prominently at $x = 0.97$ in Fig. 4.4(b). These glassy behaviors arise because the localized states formed out of the majority spin band are pushed above E_F and occupied by holes, as shown in the spin-resolved spectral intensity in Fig. 4.4(c).

To further study the localized magnetism, we consider the limit $x = 1$ and ask what happens when a few holes are doped into the band insulating NaCoO_2 by the Na vacancy. The hidden correlation effects are brought out by the slightest amount of doping. Fig. 4.5(a) displays the case of a single hole added by a Na(2) vacancy. Instead of adding the hole into the minority of the spin-polarized bands, localized states are created and pinned near the Fermi level (Fig. 4.5(a)) to accommodate the doped hole, leading to the formation of the spin-1/2 local moment distributed near the Na vacancy as shown in Fig. 4.5(b) for Na(1) and Na(2) respectively. The localized states induced by the Na electrostatic potential [13] are spin-split by

$$(4.4) \quad \Delta_i = \varepsilon_{i\uparrow} - \varepsilon_{i\downarrow} = (1/2x_i) \sum_j g_{ij}^\uparrow \langle t_{ij} c_{i\uparrow}^\dagger c_{j\uparrow} + h.c. \rangle.$$

The latter has a localized profile whose amplitude $E_b = \Delta_{\max} - \Delta_{\min}$ is used as a measure of the binding energy of the local moment. In Fig. 4.5(c), E_b is plotted as a function of the *bare* Na potential V_d . The local moment develops ($E_b > 0$) for V_d as small as 0.2 eV. Because the Na(1) vacancy is directly above a Co site, E_b is enhanced, making it easier for the local moment to form near Na(1) vacancies. For even smaller V_d , it becomes difficult for our finite size numerical calculations to discern the localized states and the values of E_b , leaving open the possibility of self-trapped, spontaneous local moment formation without the Na potential.

When the Na vacancies are isolated, the spin-1/2 local moments behave as free moments, contributing to significant spin entropy in the Na-rich part of the phase diagram. As the vacancy density increases, i.e. as the average x reduces, the local moments begin to overlap and their interactions become important. We find that nearby local moments

have AF correlations. As shown in Fig. 4.5(d), since the AF frustration is alleviated by the associated charge inhomogeneity, two Na(2) or Na(1) vacancies induce two AF correlated local moments with zero net magnetization. As the local density of Na vacancy increases, FM clusters develop which eventually evolve into the macroscopic FM state. Our findings provide a complimentary description of the evolution from local magnetic clusters to macroscopic FM state observed by recent μ SR experiments [5] and interpreted in terms of a change in the Co^{3+} spin state that involves the higher Co-3d e_g orbitals [10, 20].

We conclude with a discussion of an outstanding puzzle in the ARPES experiments. A large hole-like FS is observed at $x = 0.8$ with a volume much larger than what is expected by the Luttinger counting in a PM state [21, 22]. A natural explanation is that this corresponds to the minority spin band of the itinerant half-metallic state with in-plane FM order. Such an interpretation, although in line with that of the neutron scattering experiments [4], implies a filled majority band below the Fermi level which has yet to be detected by ARPES. Our study suggests another possible scenario where the in-plane FM order associated with the 3D A-type AF order does not develop on the 2D surface at finite temperatures. The larger than expected FS comes instead from the loss of the doped electrons due to Na-induced localization and are “taken out” of the t_{2g} bands. For example, a substantial fraction of the doped electrons on the surface can be localized to form the nonmagnetic Co^{3+} similar to Fig. 4.4(a). This picture is appealing given the recent finding by NMR of valence disproportionation associated with significant Co^{3+} formation for $0.65 < x < 0.75$ [12]. Interestingly, the same picture within the present theory suggests that in the extremely sodium rich phases $x > 0.96$, it is the localization

of a fraction of holes near the Na vacancies that gives rise to the local magnetic clusters observed by μ SR experiments [5]. Further studies are clearly needed to better understand the coexistence of itinerant and localized magnetism in the sodium rich cobaltates.

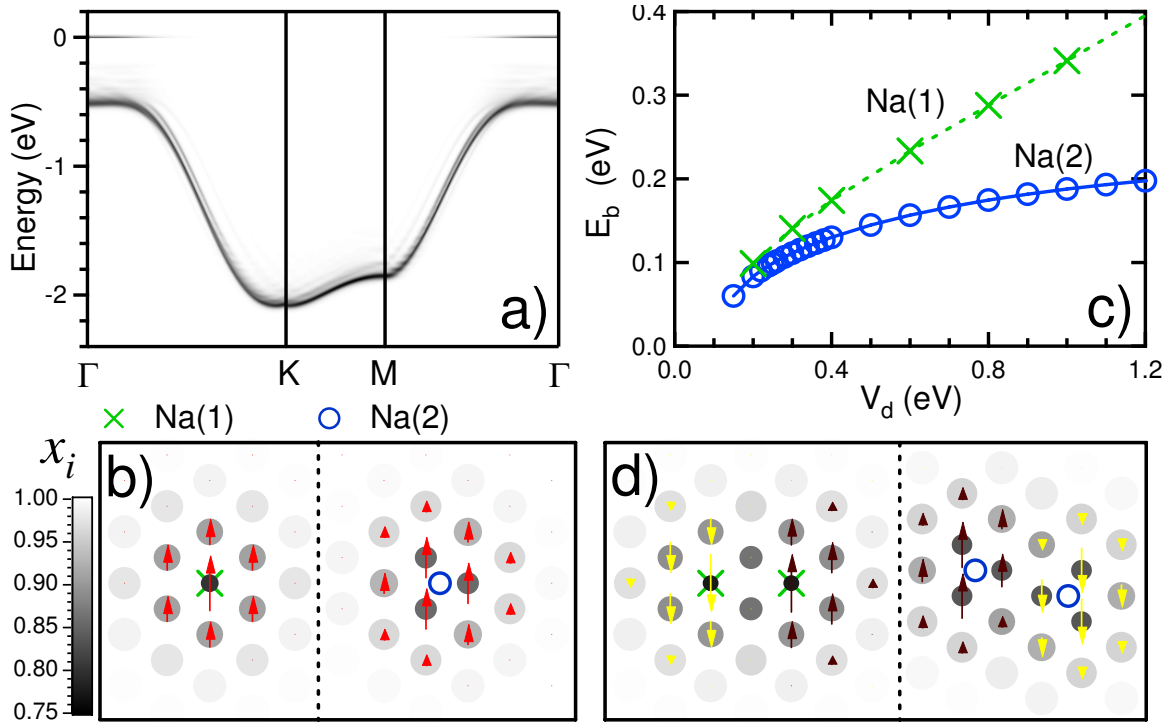


Figure 4.5. (a) Spectral intensity of one-hole doped by a Na(2) vacancy at $V_d = 1.0$ eV. (b) Spin and charge distribution of the $S=1/2$ local moment near a Na(1) and a Na(2) vacancy. (c) The local moment "binding energy" E_b as a function of V_d induced by a Na(1) or Na(2) vacancy at $V_d = 0.6$ eV. (d) Spin/charge distribution around two Na(1) and two Na(2) vacancies shows AF correlations between the local moments.

References

- [1] K. Takada, et. al., Nature (London) **422**, 53 (2003).
- [2] M.L. Foo et al., Phys. Rev. Lett. **92**, 247001 (2004).
- [3] A.T. Boothroyd, et. al., Phys. Rev. Lett. **92**, 197201 (2004).
- [4] S.P. Bayrakci et al., Phys. Rev. Lett. **94**, 157205 (2005).
- [5] C. Bernhard, Ch. Niedermayer, A. Drew, G. Khaliullin, S. Bayrakci, J. Stremper, R.K. Kremer, D.P. Chen, C.T. Lin, and B. Keimer, EPL **80**, 27005 (2007).
- [6] M. Lee, et. al., Nature Materials, **5**, 537 (2006).
- [7] J. Merino, et. al., Phys. Rev. B **73**, 235107 (2006).
- [8] J.O. Haerter, et. al., Phys. Rev. Lett. **97**, 226402 (2006).
- [9] M. M. Korshunov et al., Phys. Rev. B **75**, 094511 (2007).
- [10] M. Daghofer, et. al., Phys. Rev. Lett. **96**, 216404 (2006).
- [11] Q. Huang, M.L. Foo, R.A. Pascal, Jr. J.W. Lynn, B.H. Toby, Tao He, H. W. Zandbergen, and R. J. Cava, PRB **70**, 1184110 (2004).
- [12] I.R. Mukhamedshin, et. al., cond-mat/0703561.
- [13] C.A. Marianetti and G. Kotliar, Phys. Rev. Lett. **98**, 176405 (2007).
- [14] M.Z. Hasan et al., Phys. Rev. Lett. **92**, 246402 (2004).
- [15] S. Zhou and Z. Wang, Phys. Rev. Lett. **98**, 226402 (2007).
- [16] O.I. Motrunich and P.A. Lee, Phys. Rev. B **69**, 214516 (2004).

- [17] H.W. Zandbergen et. al., Phys. Rev. B**70**, 024101 (2004); Q. Huang et. al. Phys. Rev. B**70**, 184110 (2004).
- [18] G. Gasparovic et al., Phys. Rev. Lett. **96**, 046403 (2006).
- [19] J. Bobroff et al., Phys. Rev. Lett. **96**, 107201 (2006).
- [20] C. Bernhard, et. al. Phys. Rev. Lett. **93**, 167003 (2004).
- [21] D. Qian, et. al. Phys. Rev. Lett. **96**, 216405 (2006).
- [22] H. Ding, et. al. to be published.

CHAPTER 5

Novel Electronic States at $x=0.84$

From the experimentally established phase diagram [1], strong correlation effects have been observed in the sodium rich regime even though when $x=1$, NaCoO_2 is a band insulator. Sodium potential also plays an important role in the formation of various electronic states[2, 3]. At $x=0.84$, a special sodium ordering is reported[4]. Within the framework of an extended Hubbard model on the triangular lattice, we study the formation of unconventional and inhomogeneous electronic states. These findings are compared with recent experimental observations around $x=0.84$ [4, 5, 6, 7].

5.1. Na ordering and Na potential

Na ordering has been investigated in a wide range of doping levels [8]. From $x = 0.15$ to $x = 0.75$, a series of ordered Na superlattice has been found through electron diffraction, as in Fig. 5.1. The Na contents order in different structures rather than simply maximizing Na-Na separation. These superstructures provide a possibility of linking Na layer ordering to the properties of cobaltates.

Previous evidence has shown that the interplay between Na ordering and strong correlation plays an important role in the formation of the insulating state at $x=0.5$ [3]. From Fig. 5.1(b), at $x=0.5$ it shows a $\sqrt{3} \times 2$ chain ordering in sodium layers, which is also the strongest superstructure in all investigated areas [8]. This ordering feature is also observed by Huang *et al* in 2004 [9]. It is known that at $x = 0.5$ this cobaltates

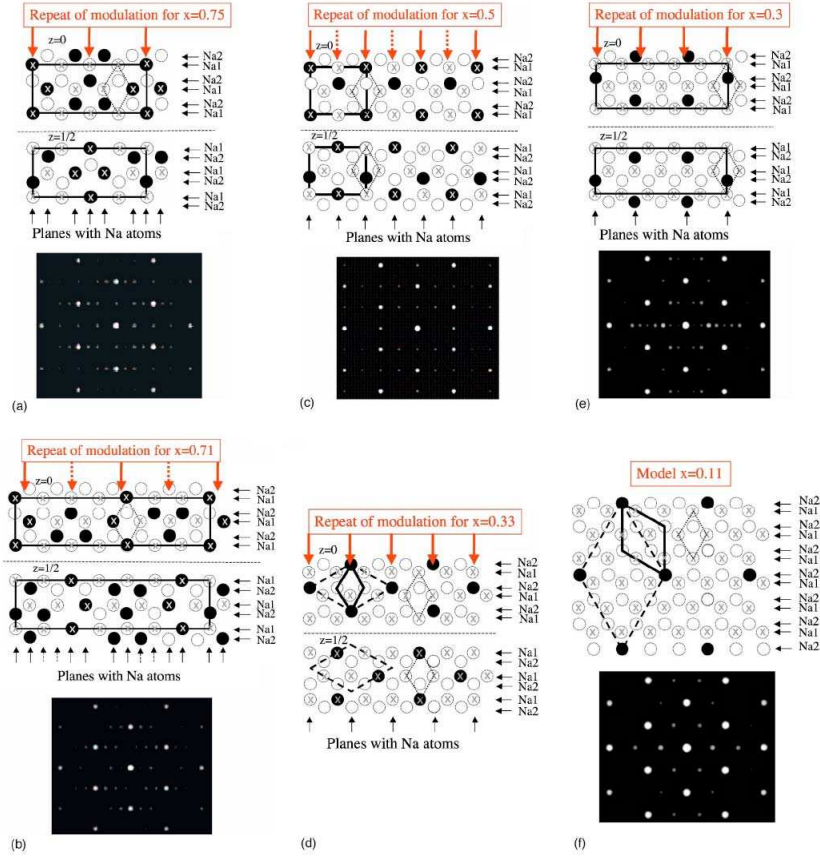


Figure 5.1. Models for the Na planes of Na_xCoO_2 with $x = 0.15 \sim 0.75$. Both the Na planes on $z = 0$ and $z = 1/2$ are given. Occupied Na positions are given as black dots and Na vacancies as open circles. X indicates the positions of the underlying Co atoms. Dashed lines indicate that only one of the lines on $z = 0$ and $z = 1/2$ is occupied. The basic hexagonal unit cell is indicated by dotted lines. Below the models are the calculated diffraction patterns for a thickness of 10 nm and 200 kV.

shows an insulating behavior whereas the others show a metallic behavior. The $\sqrt{3} \times 2$ is arranged in a staggering way between 2 adjacent sodium layers. The sodium potential exerting on the Cobalt layer is $\sqrt{3} \times 1$ and the charges order in the same superstructure.

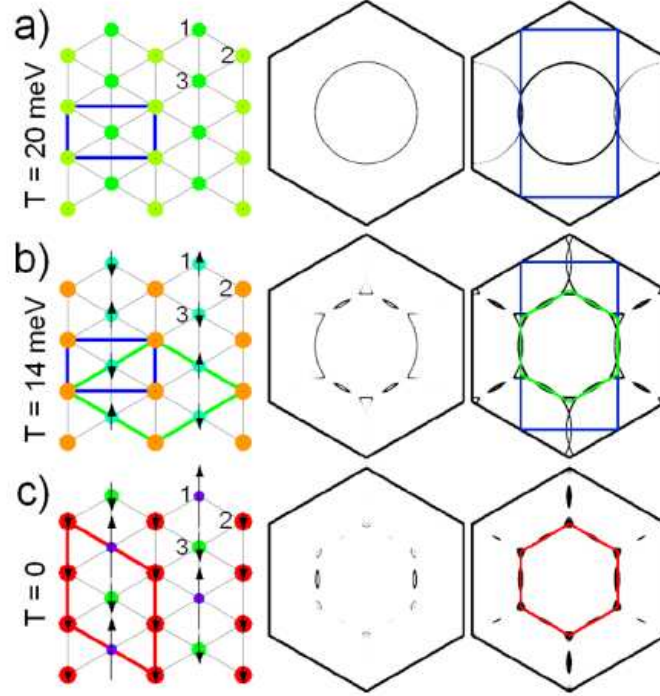


Figure 5.2. Self-consistent $x=0.5$ states at different temperatures. From left to right columns, charge- or spin-ordering patterns and unit cells; FS without thermal broadening showing the anisotropic gapping of the FS; intensified FS showing the band folding along zone boundaries of corresponding charge or spin order.

The symmetry breaking makes AFM ordering energetically favorable by alleviating frustration via weak charge inhomogeneity, and also enables successive $\sqrt{3}a \times 1a$ AFM and $2a \times 2a$ charge- or spin-ordering transitions at low temperatures, shown in Fig. 5.2. The Fermi surface is truncated by the $2a \times 2a$ zone boundary into small electron and hole pockets.

Marianetti *et al* also propose that Na potential is a key element in forming the correlation in the sodium rich regime where strong correlation is observed by experiments, by

LDA + DMFT. To mimic the sodium potential, a fraction of $(1-x)$ sites have a potential ϵ_1 while the others have a potential ϵ_2 . At $x=0.75$ a Curie-Weiss tail is formed, but this behaviour is not developed at the Na poor region, *e.g.* $x=0.3$.

$Na_{0.84\pm 0.01}CoO_2$ is one of the special doping levels, the limit of single phase stability for high temperature melt growth. Above this limit, phase separation emerges. In 2008, Chou *et al* [4] studied the material by synchrotron x-ray diffraction on single crystals. A $\sqrt{13} \times \sqrt{13}$ Na order is discovered based on the formation of divacancies [4, 10], shown in Fig. 5.3. This result leads to a coexistence of local moments and itinerant carriers. All these results are important steps to understanding the rich properties of cobaltates [1].

The formation of $\sqrt{13} \times \sqrt{13}$ superlattice proposed by the paper of Chou *et al* consists of divacancy structures. This idea of divacancies is based on the study of Roger *et al*[10], which proposes a dopant clustering concept. They use single-crystal neutron diffraction supported by numerical simulations to determine the long-range three-dimensional superstructures of ions. Their study of sodium ordering and its associated distortion field is purely governed by electrostatics. The organizational principle is to stabilize the long-range ordered charge droplets at some simple fractional fillings. In Fig. 5.4(a), a divacancy structure is shown at the bottom left corner. It is formed by taking out 3 Na2 dopants and replacing them by a Na1 dopant. The resultant divacancy cluster has net charge $2e^-$ spread over three sites and has the lowest stabilization energy than vacancies three to four sites apart. The formation of trivacancies and quadrivacancies follows a similar process. Fig. 5.4 (b) is a comparison of ground-state energies of superstructures for different dopant clusters. Although the result is different from Chou *et al*'s conclusion which

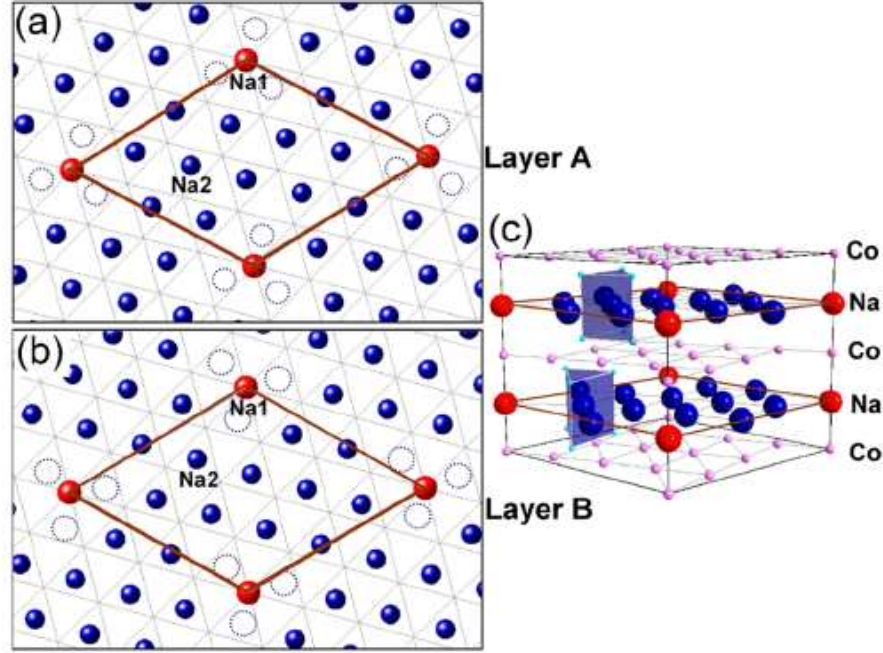


Figure 5.3. Proposed crystal structure of $Na_{0.84}CoO_2$. a) and b) are the 2D view of the Na layers A and B with superstructure of $\sqrt{13} \times \sqrt{13}$, shown by solid lines. c) shows the corresponding 3D structure of in-phase stacking, although there is no way to tell in-phase and out of phase stacking in experiments. There is a 180° rotation between two adjacent layers.

has the trend of increasing cluster size with decreasing x [4], the concept of Na dopant clustering plays an import role in charge ordering, transport, and magnetic properties.

The effect of Na dopant potential is added to the Hamiltonian in the form of

$$(5.1) \quad H_{V_{dopant}} = \sum_i V_d \sum_{I=1}^{N_{Na}} \frac{\hat{n}_i}{\sqrt{|\vec{r}_I - \vec{r}_i|^2 + d_z^2}}$$

where V_d is the potential strength and $d_z \simeq a$ is the setback distance of Na to the Co plane.

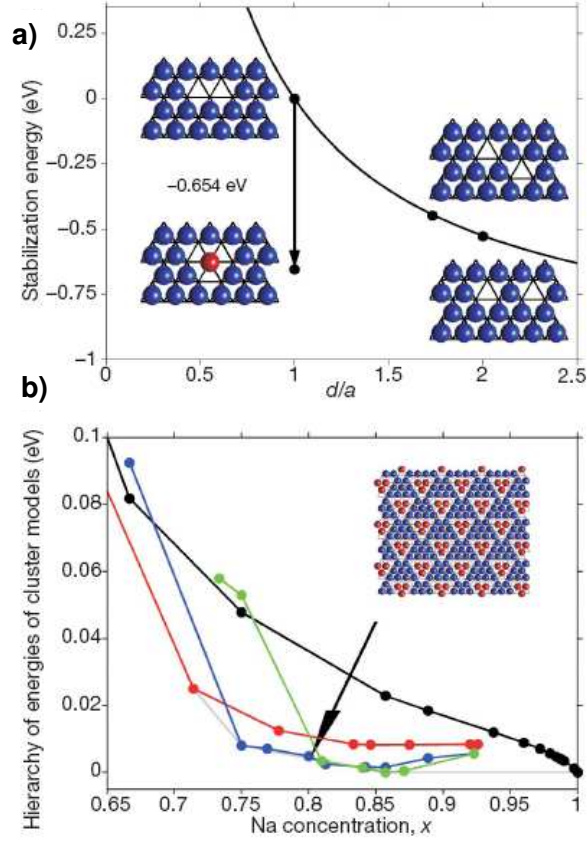


Figure 5.4. a) Energy for two vacancies decreases with increasing distance d , in the units of the hexagonal lattice parameter a , as expected for Coulomb repulsion. The divacancy structure has lower stabilization energy than other structures simply with sites apart. (b) Ground-state energies of super structure for mono-vacancies (black), divacancies (red), tri-vacancies (blue) and quadri-vacancies (green). The inset shows the $x=0.8$ tri-vacancy phase.

5.2. Experimental evidence of coexistence of localized moments and itinerant carriers

Chou *et al*'s paper proposes a picture of coexistence of localized moment and itinerant carriers. They argue that in the $\sqrt{13} \times \sqrt{13}$ structure $x = 0.84$ is equivalent to $\frac{2}{13}$ holes

in the band. The strong potential of the divacancy can localize one hole, while the other one remains itinerant. If the Kondo coupling dominates, the one hole localized one hole itinerant scenario might become a Kondo insulator. Otherwise it would be a metal with antiferromagnetically ordered moments. However, the ground state is observed to be a ferromagnetic metallic state, as opposed to an antiferromagnetic metal or a Kondo insulator.

Chou *et al* argues that the ferromagnetism is induced by the following features. The extrapolated γ from temperature above the magnetic transition T_N is 24 mJ/Co-mole, corresponding to an effective mass 35 times of that of a free electron and a nearest band hopping integral of 14 meV. This is a 6-7 times mass enhancement regarding to LDA tight binding fit. If the number of carriers is assumed to be $\frac{1}{13}$ per Co, the Fermi temperature is 87 K, an exceptionally low energy. All these numbers can lead to an expectation of ferromagnetism. The narrow band with low energy favors spin polarization to gain exchange energy at the expense of kinetic energy, due to Stoner mechanism. This overcomes the kondo coupling and will form a fully polarized "half-metal". They also propose the fully polarized FS overlaps with the reduced Brillouin zone boundary. This intersection will give rise to small hole pockets and electron pockets.

Other evidence of small FS pockets at $x = 0.84$ has been observed by Balicas' group [5]. Their observation through the Shubnikov-de Haas effect indicates that the area of FS is less than 0.6% of the 1st Brillouin zone, according to Onsager relation $F = A(\hbar/2\pi e)$ [11] and measurement shown in Fig. 5.5(a). It shows 2 main detected frequencies, which corresponding to Fermi surface area around 0.6%. While in a paramagnetic state, the FS

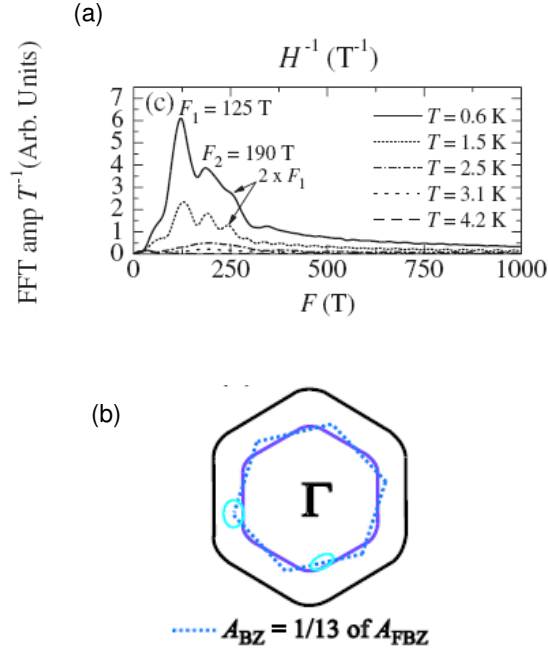


Figure 5.5. FS area measurement and topology scheme at $x=0.84$. a) Amplitude of the fast Fourier transform normalized by temperature T for several values of T . Two main frequencies are detected: $F_1 = 125$ T, $F_2 = 190$ T. b) The superlattice-induced new Brillouin zone (blue dotted line) is $1/13$ of area of the original FBZ, and the spin-polarized Fermi surface for 2 and 1 hole per unit formula, respectively, in black and purple. For 1 hole per reconstructed unit cell, the originally depicted spin-polarized Fermi surface intersects with the new Brillouin zone.

area at $x=0.84$ is predicted to be around 7.7%. The proposed Fermi topology is plotted in Fig. 5.5(b), although the location of the small pockets can not be observed directly.

5.3. Charge ordering with small sodium potential

We first consider cases at $x=11/13 \simeq 0.84$ without Na potential based on the one-band t-U-V model on a triangular lattice.

$$(5.2) \quad H^{t-U-V} = \sum_{i,j,\sigma} t_{ij} c_{i\sigma}^\dagger c_{j\sigma} + \sum_i U \hat{n}_{i\uparrow} \hat{n}_{i\downarrow} + V \sum_{i>j} \frac{\hat{n}_i \hat{n}_j}{|\vec{r}_i - \vec{r}_j|}$$

where $c_{i\sigma}^\dagger$ creates an a_{1g} hole with spin σ . \hat{n}_i is the hole density operator. U is the on-site Coulomb repulsion. V is long range Coulomb repulsion and considered to help the formation of charge ordered phases [3, 12]. Without V , the system is always considered as a uniform paramagnetic or ferromagnetic state.

Based on the t-U-V model, our result shows $\text{Na}_{11/13}\text{CoO}_2$ is a uniform PM state. At $x=11/13$, if charges on the triangular lattice order according to a $\sqrt{13} \times \sqrt{13}$ structure, the reconstructed 1st Brillouin zone will have an area of 1/13 of the original zone. This will intersect with the paramagnetic Fermi surface since the FS is a center pocket of 1/13 area of the original 1st BZ according Luttinger theorem [13]. Previous study has found that a spontaneous charge and spin ordering formation when the FS intersects with the reconstructed 1st Brillouin zone at $x=1/3$ [3]. However, the charge and spin sectors are coupled in the sense that the removal of inhomogeneity in either reinstates the uniform PM phase.

The topology scenario of the $x=11/13$ case can be generalized at doping levels of $x = p/q$ when both p and q are integers. According to Luttinger theorem, the area of the FS over the 1st BZ is $1/\frac{2q}{q-p}$. In these cases, if the charge orders in a $\sqrt{\frac{2q}{q-p}} \times \sqrt{\frac{2q}{q-p}}$ superstructure, the 1st BZ reconstructs into an area same as the PM FS. The nesting of

the FS and the reconstructed zone opens a gap across the Fermi level. A previous example is given at $x=1/3$ and we will show the formation of novel electronic states at $x=11/13$, when $\sqrt{13} \times \sqrt{13}$ superstructure appears.

The $\sqrt{13} \times \sqrt{13}$ structure is detected by Chou *et al* [4] at $x=11/13$ in each sodium layer and how the stacking order develops is unknown. We apply a in-phase stacking sodium potential to cobalt layers by adding sodium potential in Eq.(5.1). In-phase stacking is defined as Na1 in two alternating sodium layers are along the same c-axis with Na2 sites rotated by 60° , as in Fig. 5.3. This configuration gives a $\sqrt{13} \times \sqrt{13}$ external potential to the cobalt sites. Each unit cell is a tilted rhombus with the center of the divancies at the its corners. The center of the divany consists of one Na1 replacing 3 Na2, so negative potential troughs form at the corners of unit cells. They attract holes at these sites and charges order in a $\sqrt{13} \times \sqrt{13}$ way. Hamiltonian in the strong correlation limit is written as

$$(5.3) \quad H = \sum_{ij\sigma} g_{ij}^\sigma t_{ij} c_{i\sigma}^+ c_{j\sigma} + \sum_{i,\sigma} \varepsilon_{i\sigma} (c_{i\sigma}^+ c_{j\sigma} - n_{i\sigma}) \\ + V \sum_{i>j} \frac{\hat{n}_i \hat{n}_j}{|\vec{r}_i - \vec{r}_j|} + \sum_i V_d \sum_{I=1}^{N_{Na}} \frac{\hat{n}_i}{\sqrt{|\vec{r}_I - \vec{r}_i|^2 + d_z^2}}$$

where, g_{ij}^σ is the Gutzwiller renormalization factor,

$$(5.4) \quad g_{ij}^\sigma = \sqrt{\frac{x_i x_j}{(1 - n_{i\sigma})(1 - n_{j\sigma})}}$$

$\varepsilon_{i\sigma}$ is a spin dependent local fugacity that maintains the equilibrium condition and local densities upon Gutzwiller projection [14, 15].

$$(5.5) \quad \varepsilon_{i\sigma} = -\frac{1}{2x_i} \left(\frac{n_{i\bar{\sigma}}}{1 - n_{i\sigma}} \sum_j g_{ij}^{\sigma} t_{ij} \langle c_{i\sigma}^+ c_{j\sigma} \rangle + \sum_j g_{ij}^{\bar{\sigma}} t_{ij} \langle c_{i\bar{\sigma}}^+ c_{j\bar{\sigma}} \rangle \right)$$

Imposing such a super structure with a weak V_d , *i.e.* $V_d \leq 0.2$ eV, the originally uniform band dispersion folds into the reconstructed BZ and forms 13 quasi-particle bands, as shown in Fig. 5.6 (a). The nesting opens a small gap but the first and the second bands still cross the Fermi level. From Fig. 5.6(b), it shows that a semi metal state exists with hole-like pockets at the BZ corners and electron-like narrow pockets along BZ sides. In Fig. 5.6(c), it shows that a little stronger V_d , *i.e.* $V_d > 0.2$ eV, opens a gap wide enough for the system to transit into a band insulator.

In a usual situation, when each unit cell of this superstructure contains of 2 holes, the lowest energy level will accommodate them and the system becomes a band insulator. This state is easily formed with very weak charge ordering in our discussion. However, experiments show a metallic behaviour at this doping and the size of the FS suggests a scenario with one local moment and one itinerant carrier [4, 5]. In the following study, we would like to propose that above magnetic transition T_N such a state exists as a Curie-Weiss metal with the lowest energy level filled by one local moment due to the strong on-site U . Below T_N , as ferromagnetism comes in, the local moments can still appear but solely due to Pauli principle.

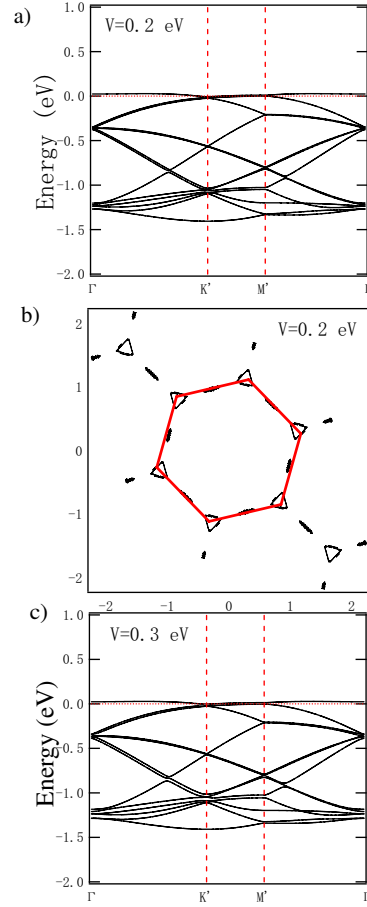


Figure 5.6. PM states with small $V_c = V_d = V$ at $x=11/13$. a) Band structure with $V=0.2$ eV, semi-metal. b) FS of the semi-metal at $V=0.2$ eV. Red lines indicate the reconstructed 1st Brillouin zone. c) Band structure with $V=0.3$ eV is totally gapped and becomes a band insulator.

5.4. High temperature PM order

A-type antiferromagnetic ordering has been found at $x=0.82$ around $T = 20K$ and magnetic transition is observed at $T = 22k$ [6, 16]. At dopings above the insulating state

$x=0.5$, Curie-Weiss like χ and linear temperature dependent resistivity has been found up to $x=0.75$, which is called a Curie-Weiss metallic state [1]. Strong correlation is obviously playing an important role in the sodium rich regime. We investigate the possible states at high temperature before the magnetic phase transition, and proposed that the state with one local moment and one itinerant carrier is formed as a result of the interplay between Na ordering and strong correlation.

As discussed in the previous section, the 1st reconstructed BZ overlaps with the PM FS due to the existence of superstructure at $11/13$. The band dispersion consists of 13 mini bands folded into the 1st BZ. With a minimal amount of sodium and long range coulomb potential, the system can go into a band insulating state with the top band being fully filled by 2 holes per supercell unit. This means if hopping exists among all the sites, the top band is a band-like structure filled by 2 energy degenerate holes due to Pauli principle.

Instead, we propose a state with only one local moment filling the top band. In this case, there is no hopping from the local moment and top band is totally localized with no band dispersion. From the structure of sodium potential, corner sites take the lowest potential and are easily localized. No hopping between the these sites and the rest sites. From the perspective view of the Hamiltonian, hopping involving the local sites is taken out of the calculation. Since the hole density n_i becomes 1 at these sites, it is no longer a variable. When $\frac{\partial H}{\partial n_i}$ is calculated to find the minimum energy as in Eq.(5.5), ε_i of local sites can not be determined this way and is set to be zero.

Following this method, Fermi topology and band structure are shown in Fig. 5.7 with different parameters $V_c = V_d \equiv V$. The top band is a totally flat line representing the

localized energy level. The occupation at this energy level is 1 local moment with arbitrary spin, since the spins are degenerate. The second hole in this unit cell resides at the second top band and remains itinerant. The second mini-band is half filled and crosses the Fermi level. Fermi-surface consist of small pockets at zone corners and one large pocket in the center. According to Luttiger's theorem, the total area of pockets should be half the area of the reduced zone. Across different potential ranges, the local energy level is adjusted with different on-site sodium and coulomb potential, as in Fig. 5.7. However, since the second band is always half-filled, the FS shapes remain unchanged. The structure of the FS is determined by the shape of the second mini band, so it is different from a single center pocket FS in the uniform half-filled case [17].

Since the wavefunctions of the state with 2 itinerant holes and the state with one itinerant and one local holes are different, there is no connection between them in the calculation. In order to argue the rationality behind the result above, the energy levels of these 2 states are presented and compared from $V=0.2$ eV to 1.2 eV in Fig. 5.8. At a low V range, the picture of 2 itinerant holes dominates. The crossover happens at $V=0.8$ eV. In summary, the system is a semi-metal below $V=0.2$ eV, a band insulator between $V=0.2$ eV and 0.8 eV, and a metallic state with one hole localized above $V=0.8$ eV.

This novel metallic state in high potential range is justified by the strong correlation U . In our infinite U limit, double occupation is totally projected out by the Gutzwiller factor. If there is more than one hole localized at the lowest energy level, it translates into a state with more than 1 hole on the local sites, which is prohibited due to large U .

Generally, in a Kondo problem, when the itinerant states and the local states start to couple, local states becomes unstable under a critical Kondo temperature T_K . Above

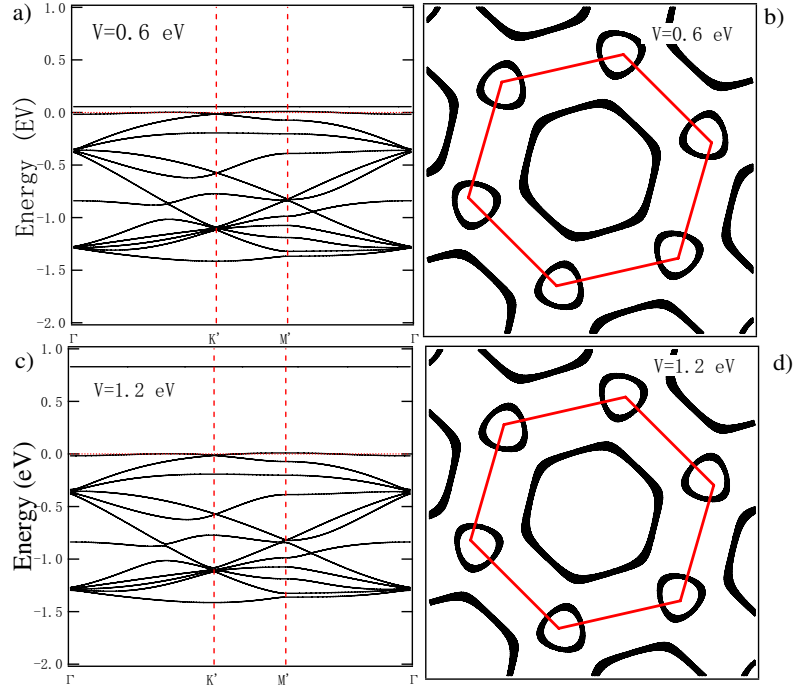


Figure 5.7. Band Structure and Fermi surface of PM state with one local moment and one itinerant carrier. K' indicates points at the corner of the reduced 1st Brillouin zone. M' indicates points in the middle of 2 nearest K' points. The system maintains 6-fold symmetry. a),b) States with a parameter $V=0.6$ eV c),d) States with a parameter $V=1.2$ eV

this temperature, the coupling is not relevant and local states stay. It seems puzzling, but apparently, in this sodium rich region, the scattering is not important and T_K is low, so that doping around $x=2/3$ the local states are stable [18].

In conclusion, the metallic behaviour above T_N can be originated from 2 possibilities. One is the semi-metallic state with extremely small $V \leq 0.2$ eV. The other way to be metallic is to form a state when half of the holes are local moments following the superstructure

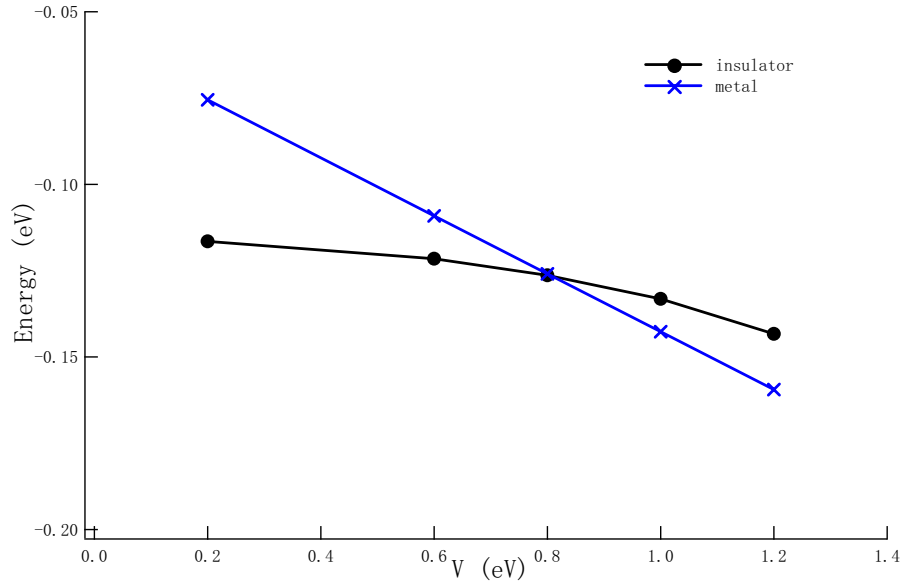


Figure 5.8. Energy comparison between the insulating state and the state with one local and one itinerant holes, as a function of V .

and are decoupled from the rest itinerant carriers. Such a state exists when V is relatively large, *i.e.* $V > 0.8$ eV.

5.5. Low temperature FM order

In the sodium rich region $x > 0.75$, Na_xCoO_2 develops a magnetically ordered ground state [1]. For single crystals with $x=0.82$, A-type antiferromagnetism with antiferromagnetically coupled ferromagnetic layers has been reported below $T=20\text{K}$ [16]. In the low temperature range, our 2-D Hubbard model + strong U is ferromagnetically ordered

when $x > 0.67$ [19]. The same U also lifts the spin-degeneracy under $\sqrt{13} \times \sqrt{13}$ superstructure. In Fig. 5.9(a), the spin split bands are folded inside the reduced zone, forming 26 quasi-particle bands in total.

With $\sqrt{13} \times \sqrt{13}$ superstructure, charges order according to the potential structure with the corner sites of the formula units attracting most holes. The FM Fermi surface is twice the size of the reduced 1st zone and cuts through the 2nd reconstructed zone boundary, as shown in Fig. 5.9(b). FS forms 6 pockets around K' points and one central hole by nesting, for the small sodium potential range $V = 0.6$ eV. From the band structure in Fig. 5.9(a), the system is fully polarized and one spin totally sinks below the Fermi level. The top band is completely filled, and the second and the third band cross Fermi level and form a semi-metal. The central pocket is an electron pocket by the crossing of the second band. The third band crossing makes hole pockets around K' point.

Increasing V makes the sodium potential with the long range Coulomb screening at corner sites more negative, attracting more holes. With a stronger $V = 1.2$ eV, the hole density at these sites approaches 1 and this localization effect makes the top band narrower and closer to a straight localized energy level than smaller V . The total band structure shown in Fig. 5.9(c) is similar to the one with $V = 0.6$ eV and stays at a ferromagnetic semi-metallic state. FS pockets however shrink comparing to the $V = 0.6$ eV state due to band narrowing. In either case, each BZ contains 2 corner pockets and one center pocket on average. The area of the central electron pocket is approximately twice of that of each corner hole pocket.

In FM states, with certain amount of V , one moment can be localized with hole density approaching 1 and the other hole carrier remains itinerant. However, the formation of this

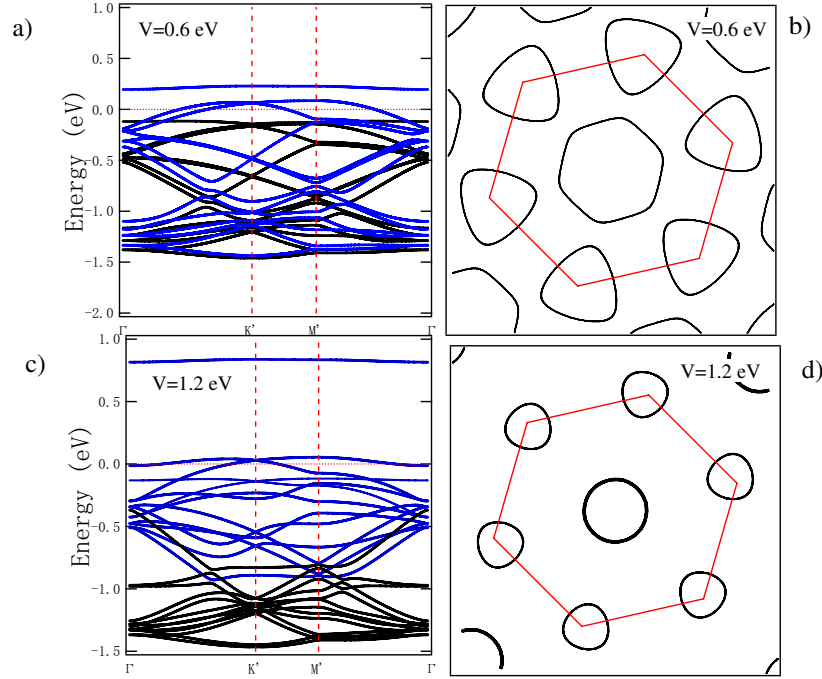


Figure 5.9. Band structure and Fermi surface of FM state with top band filled by one hole with spin σ . a),b)States with a parameter $V=0.6$ eV c),d)States with a parameter $V=1.2$ eV

scenario with one local and one itinerant hole is totally due to Pauli blocking, not strong U as in the PM case at high temperatures. Although the single a_{1g} band is polarized due to strong correlation U [17], the prevention of the 2^{nd} hole from localizing on the same site is determined by Pauli principle. The spin split band can only be filled by one hole and it is only due to obeying Pauli and not related to the strong U limit.

Thus our conclusion is different from Chou *et al*, in which they conclude the ferromagnetic metallic state is from the suppression of Kondo coupling by Stoner mechanism

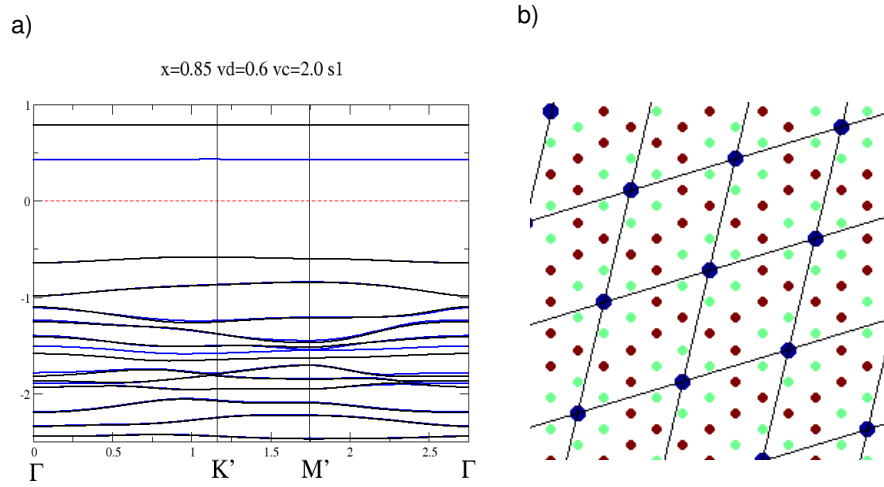


Figure 5.10. A Kondo insulator with large V_c . a) Band structure with 2 hole localized and AFM correlated. b) Madelung potential on real-space cobalt sites. The first hole is localized on the blues sites. The second localized hole can reside on any equivalent brown points within one unit cell due to degeneracy.

[4]. We believe the origin of this state is Pauli principle prohibiting the 2^{nd} hole from localization.

We would also like to discuss the effects of long-range Coulomb correlation in superstructures. Long-range V_c is equivalent to the intra-orbital U' between quasi-particles as in the multi-band calculation [17]. Increasing V_c enhances the correlation between local moments and itinerant sites. With an intermediate $V_d=0.6$ eV and a larger $V_c=2.0$ eV,

the second hole localizes inside the unit cell but not on the corner sites due to Pauli-blocking. The Madelung potential is plotted in Fig. 5.10(b). Since they are energetically degenerate, the final state is a glassy state with the second hole locating inside any one of the degenerate sites. The 2 local moments are antiferromagnetically correlated, from Fig. 5.10(a) and the system forms a Kondo insulator.

5.6. Thermal properties of $\text{Na}_{11/13}\text{CoO}_2$

We put some numbers to demonstrate the thermal properties at $x=11/13$. Above $T_N \sim 22$ K, the specific heat is well described by $C \sim \gamma T + \beta T^3$ with the first term indicating electronic contribution and the latter representing phonon contribution, shown in Fig. 5.11(b) [7]. Extrapolating the linear contribution above T_N gives $\gamma \sim 24 \text{ mJ/mol} \cdot \text{K}^2$. This value is equivalent to an effective mass $m^* = 35m_e$ comparing to a spin unpolarized parabolic band [4]. Schulze *et al* also measured this value by performing μ -SR on both polycrystalline and single crystalline samples. There are 2 phase transition existing and γ of intermediate temperature is extracted from the linear part above the first transition temperature $T_N \sim 22$ K. γ is read around $25 \text{ mJ/mole} \cdot \text{K}^2$ in Fig. 5.11(c)[6].

Without sodium potential, the tight-binding model with hopping integrals fit to LDA bands at $x=0.3$ gives a $\gamma \approx 4.2 \text{ mJ/mole} \cdot \text{K}^2$, shown in Fig. 5.11(d). The electronic contribution is totally linear. This number misses a factor of 2-3 comparing to DMFT calculation, shown in Fig. 5.11(a)[20]. Their specific heat coefficient is proportional to the ratio $\rho(e_f)/Z$, where ρ is a local spectral function and Z is the quasiparticle weight proportional to x . However, our band renormalization from Gutzwiller factor is $\frac{2x}{1+x}$,

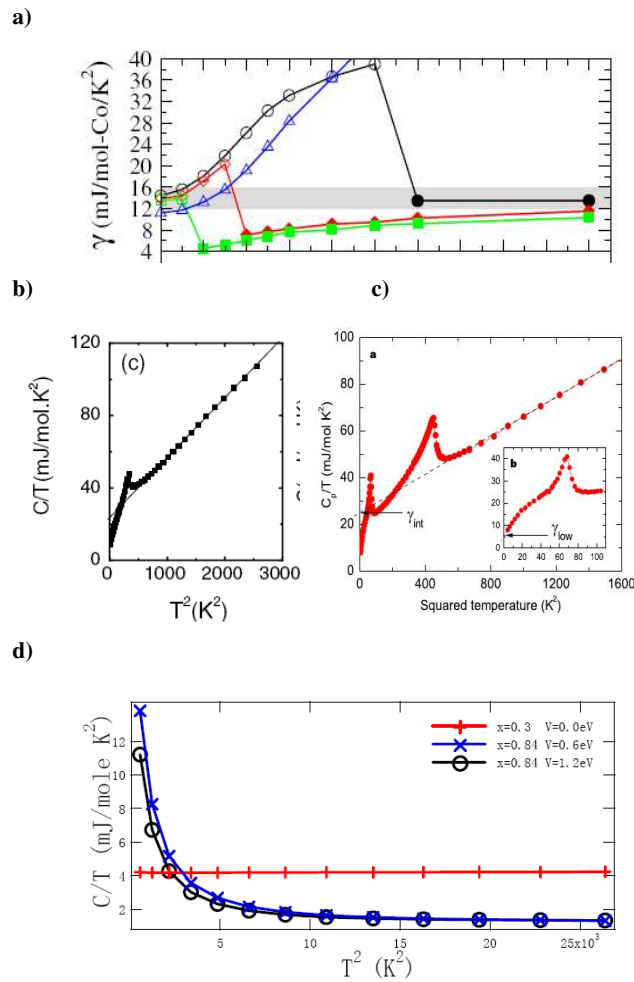


Figure 5.11. Thermal properties of Na_xCoO_2 a) γ calculation from DMFT method [20]. Different lines indicate different crystal field splitting values. At large U values, γ is around 14 mJ/mole K² b),c) Experimentally observed specific heat linear coefficient.[6, 7] d) Calculated electronic contribution of C/T at $x=0.3$ and $x=0.84$ with different parameters V . The linear coefficient is extrapolated from the high temperature range.

proportional to $2x$. This difference gives rise to the factor of 2 in the specific heat calculation.

With superstructure $\sqrt{13} \times \sqrt{13}$ at $x=11/13$, in the high temperature PM state, the thermal property result is shown in Fig. 5.11(d) and only electronic contribution is taken in to account. The C/T diverges in the low temperature range. Extrapolating γ from high temperature at $V = 1.2eV$ gives $14 \text{ mJ/mole} \cdot K^2$, which is equivalent to an effective mass 21 times of that of the free electron. Comparing to experiments results [4, 6, 7], this number is smaller by a factor of 1.5-1.7. From our previous conclusion at $x=0.3$, this difference could be rooted in our original model of Hubbard model + strong U.

5.7. Similar superstructure at $x=12/13$

For $x=12/13$, if the sodium divacancies still exist, it can form a $2\sqrt{13} \times \sqrt{13}$ superstructure on each layer. This structure satisfies the doping fraction. For 2 alternating layers above and below a Co layer, if they are out of phase stacked, as shown in Fig. 5.12(a), the sodium potential exerted on the Co layer still follows a $\sqrt{13} \times \sqrt{13}$ superstructure. Each formula unit consists of 13 sites and the filling fraction of holes is $1/13$.

In the high temperature range, paramagnetically ordered state have one hole per unit cell. The band structure is shown in Fig. 5.12(b). The top band is very narrow and half filled, resulting a nonmagnetic metal. In the low temperature range, as in Fig. 5.12(c), the system is spin split and each quasi-particle band accommodates a hole. The filling fraction of 1 hole per supercell makes the top band fully filled and becomes a band insulator.

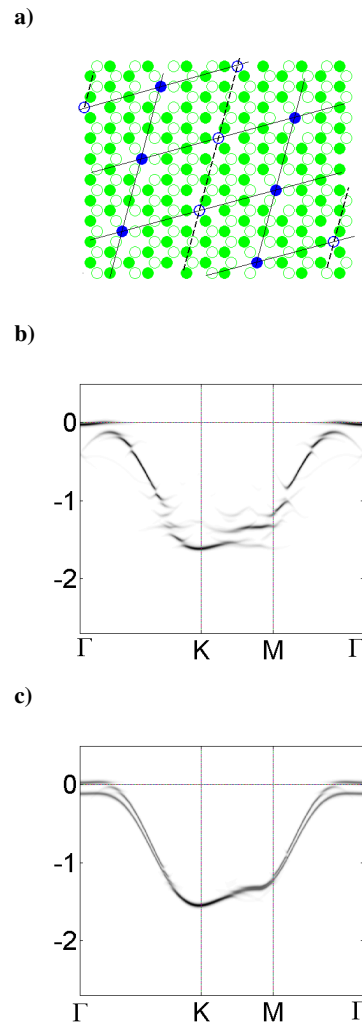


Figure 5.12. a) Sodium arrangement of $2\sqrt{13} \times \sqrt{13}$ superstructure in each layer. Solid dots and empty circles represent sodium ion in two adjacent layers. The blue ones are Na1 and the green ones are Na2. b) Above magnetic transition T_N , PM metallic state with 1 hole per super unit. c) Below T_N , FM state is filled by 1 hole per super unit and becomes a band insulator.

5.8. Conclusion

Despite the proximity to the band insulating state at $x=1$, the strong electronic correlation U plays an important role in the formation of unconventional electronic states in the sodium rich regime. Starting from Hubbard model plus the strong correlation limit, a sodium superstructure is taken into account. Below T_N , the system is ferromagnetically ordered. Na structure induces charge order. Brillouin zones reconstruct and nest with FS, forming a semi-metallic state. At temperature above magnetic transition T_N , the interplay of strong electronic correlation and $\sqrt{13} \times \sqrt{13}$ sodium order at $x=11/13$ leads to a state of 2 holes per supercell, one localized and one itinerant. The system remains as Curie metal, but the statement can only be made at this doping with experimental observations of the superstructure. Even the well known phase diagram of Na_xCoO_2 [1] are measured at discrete doping levels, in which superstructures are always present. These doping levels are believed to be stable.

References

- [1] M.L. Foo, Y. Wang, S. Watauchi, H.W. Zandbergen, T. He, R.J. Cava, and N.P. Ong, Phys. Rev. Lett. **92**, 247001 (2004)
- [2] C.A. Marianetti, and G. Kotliar, Phys. Rev. Lett. **98**, 176405 (2007)
- [3] S. Zhou, and Ziqiang Wang, Phys. Rev. Lett. **98**, 226402 (2007)
- [4] F.C. Chou, M.-W. Chu, G.J. Shu, T.-T. Huang, Woei Wu Pai, H.S. Sheu, and Patrick A. Lee, PRL **101**, 127404 (2008)
- [5] L. Balicas, Y.J. Jo, G.J. Shu, F.C. Chou, and P.A. Lee, Phys. Rev. Lett. **100**, 126405 (2008)
- [6] T.F. Schulze, M. Bruhwiler, P.S. Hafliger, S.M. Kazakov, Ch. Niedermayer, K. Mat-tenberger, J. Karpinski, and B. Batlogg, arXiv: 08081697
- [7] J.L. Luo, N.L. Wang, G.T. Liu, D. Wu, X.N. Jing, F. Hu, and T. Xiang, Phys. Rev. Lett. **93**, 187203 (2004)
- [8] H.W. Zandbergen, M. Foo, Q. Xu, V. Kumar, and R.J. Cava, Phys. Rev. **B70**, 024101 (2004)
- [9] Q. Huang, *et al*, Phys. Rev. **B70**, 184110 (2004)
- [10] M. Roger, D.J.P. Morris, D.A. Tennant, M.J. Gutmann, J.P. Goff, J.-U. Hoffmann, R. Feyerherm, E. Dudzik, D. Prabhakaran, A.T. Boothroyd, N. Shannon, B. Lake, and P.P. Deen, Nature Vol **445**, 631 (2007)
- [11] L. Balicas, M. Abdel-Jawad, N.E. Hussey, F.C. Chou, and P.A. Lee, Phys. Rev. Lett. **94**, 236402 (2005)
- [12] O.I. Motrunich, and P.A. Lee, Phys. Rev. **B70**, 024514 (2004)

- [13] H.-B. Yang, Z.-H. Pan, A.K.P. Sekharan, T. Sato, S. Souma, T. Takahashi, R. Jin, B.C. Sales, D. Mandrus, A.V. Fedorov, Z. Wang, and H. Ding, Phys. Rev. Lett. **95**, 146401 (2005)
- [14] C. Li, S. Zhou, and Z. Wang, Phys. Rev. B**73**, 060501 (2006)
- [15] Q.-H. Wang, Z.D. Wang, Y. Chen, and F.C. Zhang, Phys. Rev. B**73**, 092507 (2006)
- [16] S.P. Bayrakci, I. Mirebeau, P. Bourges, Y. Sidis, M. Enderle, J. Mesot, D.P. Chen, C.T. Lin, and B. Keimer, Phys. Rev. Lett. **94**, 157205 (2005)
- [17] S. Zhou, M. Gao, H. Ding, P.A. Lee, Z. Wang, Phys. Rev. Lett. **94**, 206401 (2005)
- [18] Y. Wang, N.S. Rogado, R.J. Cava, and N.P. Ong, Nature Vol 423, 425 (2003)
- [19] M.Gao, S. Zhou, and Z. Wang, Phys. Rev. B**76**, 180402 (2007)
- [20] C.A. Marianetti, K. Haule, and O. Parcollet, Phys. Rev. Lett. **99**, 246404 (2007)